8/132

**NATIONAL LIBRARY**
**OTTAWA**

CANADA

**BIBLIOTHÈQUE NATIONALE**
**OTTAWA**

NAME OF AUTHOR.......JIRI VRBA.......

TITLE OF THESIS.....Tunneling into weakly-coupled films of Aluminum and Tin in proximity.......

UNIVERSITY....of Alberta.......

DEGREE FOR WHICH THESIS WAS PRESENTED.....PhD.......

YEAR THIS DEGREE GRANTED.......1971.......

Permission is hereby granted to THE NATIONAL LIBRARY OF CANADA to microfilm this thesis and to lend or sell copies of the film.

The author reserves other publication rights, and neither the thesis nor extensive extracts from it may be printed or otherwise reproduced without the author's written permission.

(Signed).......Jiří Vrba.......

PERMANENT ADDRESS:

.......Department of Physics
.......Univ. of Alta
.......Edmonton

DATED...April 16,.......1971

NL-91 (10-68)

THE UNIVERSITY OF ALBERTA

# TUNNELING INTO WEAKLY - COUPLED FILMS OF ALUMINUM AND TIN IN PROXIMITY

BY

© JIRI VRBA

A THESIS
SUBMITTED TO THE FACULTY OF GRADUATE STUDIES IN
PARTIAL FULFILMENT OF THE REQUIREMENTS FOR THE
DEGREE OF DOCTOR OF PHILOSOPHY

DEPARTMENT OF PHYSICS
EDMONTON, ALBERTA
SPRING, 1971

UNIVERSITY OF ALBERTA
FACULTY OF GRADUATE STUDIES

The undersigned certify that they have read, and recommend to the Faculty of Graduate Studies for acceptance, a thesis entitled "TUNNELING INTO WEAKLY - COUPLED FILMS OF ALUMINUM AND TIN IN PROXIMITY", submitted by Jiri Vrba in partial fulfilment of the requirements for the degree of Doctor of Philosophy.

Supervisor

C. R. James

Gaston Fischer
External Examiner

Date 5 April 1971

# ABSTRACT

Self-consistent computer calculations with the McMillan tunneling model of the proximity sandwich have been carried out and a detailed analysis of the tunneling density of states has been made. Also tunneling experiments have been performed into the aluminum side of some aluminum-tin proximity sandwiches and into the tin side of others evaporated at room temperature onto an oxidized aluminum electrode B. The coupling between the aluminum and tin proximity films was made weak by purposely allowing slight oxidation to occur at the interface. The properties of the sandwich depend on the amount of this oxidation. When B is superconducting, the double-peaked structure of the McMillan density of states is resolved in the tunneling conductance as a function of voltage and the range of its observability has been established. When B is normal, the normalized tunneling conductance between B and the aluminum side of the sandwich in the vicinity of the critical temperature of the sandwich is markedly different from that of junctions formed between B and a BCS superconductor. The normalized conductance between B when it is normal and the tin side of the sandwich in the vicinity of the critical temperature of the sandwich is about the same as that of a junction formed between B and a BCS superconductor. The comparison of these experimental results shows satisfactory quantitative agreement with the predictions of the McMillan model.

# ACKNOWLEDGEMENTS

It is a particular pleasure to thank Dr.S.B.Woods, my research supervisor,for his cheerful encouragement, instructive help and guidance during the course of this research and during the preparation of this manuscript.

I wish to thank Dr.J.G.Adler and Dr.J.S.Rogers for many valuable discussions pertaining to this project.

My thanks are also due to Mr.R.Teshima for his kind help with various mathematical problems and with writing of the computer programs. I also wish to thank to Mr.C.J.Elliott for suggesting the method for computer fitting of the oxidation curves.

I wish to thank to Mr.J.Brunel for allowing us to evaluate our interference fringes on his optical densitometer.

It is a great pleasure to thank the technical staff of the Physics Department and, in particular, Mr.H.McClung and Mr.N.Riebeek for dealing with my various problems in a co-operative manner.

I am most grateful to my wife, Mirjana, for her patience, understanding, and the constant encouragement. I am also indebted to her for typing this thesis.

Finally, it is pleasure to acknowledge the alternating financial support of the Physics Department and the National Research Council during the course of this work.

# TABLE OF CONTENTS

Chapter Page

I. INTRODUCTION 1

II. THE REVIEW OF PREVIOUS WORK ON PROXIMITY EFFECT 3

1. General Considerations 3
2. Critical Temperature of Proximity Sandwich 5
3. Excitation Spectrum of Proximity Sandwich 10
4. Experimental Difficulties 12

III. THE MCMILLAN TUNNELING MODEL OF PROXIMITY SANDWICH 15

1. Description of the Model 15
2. Computer Calculations of the Model for Aluminum - Tin Sandwich 18

IV. EXPERIMENTAL PROCEDURE 33

1. Sample Preparation 33
2. Oxidation (Tunneling Barrier) 34
3. Thickness Measurements 38
   a. The Tolansky Interferometer 38
   b. Quartz Crystal Thickness Monitor 40
4. Description of Apparatus and Production of Low Temperatures 44

V. DISCUSSION OF MATERIALS USED 49

1. Selection of Materials 49

2. Problem of Interdiffusion 49

3. Mean Free Path 50

VI. TUNNELING INTO A PROXIMITY SANDWICH 57

1. The Tunneling Integral 57

2. Tunneling into the N-Side of a Proximity Sandwich 58

a. Tunneling from a Normal Metal 58

b. Tunneling from a Superconductor 65

c. Dependence of Data on α and Thickness 72

3. Tunneling into the S-Side of a Proximity Sandwich 76

a. Tunneling from a Normal Metal 76

b. Tunneling from a Superconductor 78

c. Dependence of Data on α 81

VII. SUGGESTIONS FOR FURTHER WORK 88

VIII. CONCLUSION 90

Appendix

I. THE CALCULATION OF THE FUNCTION B 93

II. THE CALCULATION OF THE CRITICAL TEMPERATURE OF THE MCMILLAN MODEL 95

III. GLOW DISCHARGE OXIDATION OF FRESHLY EVAPORATED ALUMINUM FILMS 97

IV. THE EVALUATION OF THE THICKNESS FROM THE INTERFERENCE FRINGES 109

V. THE CIRCUIT DIAGRAM OF THE QUARTZ CRYSTAL THICKNESS MONITOR 116

VI. A SIMPLE, CONTINUOUS READING LIQUID LEVEL DETECTOR 119
VII. A DESCRIPTION OF A TYPICAL RUN 125
BIBLIOGRAPHY 129

## LIST OF TABLES

Table Page
I. The Mean Free Path of Evaporated Tin Films as a Function of Thickness 56
II. Transmission Probability α and $\Gamma_N$ as a Function of the Oxidation Conditions for Al-Sn Proximity Sandwiches at 1.4°K (Tunneling into the Aluminum Side of a Sandwich) 73
III. Transmission Probability α and $\Gamma_S$ as a Function of the Oxidation Conditions for Sn-Al Proximity Sandwiches. Peaks P1 and P2 Are Measured at 1.4°K unless otherwise stated. (Tunneling into the Tin Side of a Sandwich) 84
IV. Transmission Probability α for Barriers Formed by the Evaporation of SiO or Glow Discharge Oxidation. Peaks P1 and P2 Are Measured at 1.4°K. (Tunneling into the Tin Side of a Sandwich) 86

# LIST OF FIGURES

| Figure | | Page |
|---|---|---|
| III.1 | The McMillan normalized density of states in the N-side of an aluminum-tin proximity sandwich. | 19 |
| III.2 | The McMillan normalized density of states in the S-side of an aluminum-tin proximity sandwich. | 21 |
| III.3 | Temperature variation of the peaks P1 and P2 in the density of states in the aluminum side of the proximity sandwich and the potentials $\Delta_S^{ph}$ and $\Delta_N^{ph}$ when $d_N < d_S$. | 23 |
| III.4 | Temperature variation of the peaks P1 and P2 in the density of states in the tin side of the proximity sandwich and the potentials $\Delta_S^{ph}$ and $\Delta_N^{ph}$ when $d_N > d_S$. | 24 |
| III.5 | The critical temperature, $T_C$, of an aluminum-tin proximity sandwich plotted vs $\Gamma_N$. | 26 |
| III.6 | The self-consistent calculations of the McMillan model for an aluminum-tin sandwich when $d_N < d_S$. | 28 |
| III.7 | The self-consistent calculations of the McMillan model for an aluminum-tin sandwich when $d_N > d_S$. | 29 |

| | | |
|---|---|---|
| III.8 | The magnitude of the induced peak at 1°K according to the McMillan model. | 31 |
| IV.1 | The relative change of the resistance of an aluminum film during the glow discharge oxidation as a function of thickness. | 36 |
| IV.2 | Illustration of the thickness meassurement. | 39 |
| IV.3 | Schematic diagram of Tolansky interferometer. | 41 |
| IV.4 | Quartz crystal holder. | 42 |
| IV.5 | Schematic diagram of the evaporator - cryostat. | 45 |
| V.1 | Residual resistivity as a function of thickness for various values of mean free path. | 53 |
| V.2 | The mean free path of evaporated aluminum films as a function of thickness. | 54 |
| VI.1 | The experimental and calculated tunneling conductivity curves. | 59 |
| VI.2 | Experimental dependence of $[1 - \sigma(V = 0)]$ on $(1 - T/T_C)$ for the aluminum side of a proximity sandwich. | 61 |
| VI.3 | Calculated values of the exponent n in the empirical expression $[1 - \sigma(V = 0)] \propto (1 - T/T_C)^n$. | 63 |
| VI.4 | The normalized tunneling conductance $\sigma(V)$ between a normal metal and an aluminum-tin sandwich. | 64 |
| VI.5 | Illustration of the occurrence of | |

multiple peak structure in the tunneling conductance between an ordinary superconductor and the N-side of an aluminum-tin sandwich· 66

VI.6 Comparison of experimental and theoretical normalized conductance for tunneling from superconducting aluminum into the N-side of aluminum-tin proximity sandwich.(Weak coupling) . 67

VI.7 Comparison of experimental and theoretical normalized conductance for tunneling from superconducting aluminum into the N-side of aluminum-tin proximity sandwich.(Strong coupling) . 69

VI.8 The experimental temperature dependence of peak positions in the N-side of a proximity sandwich. 71

VI.9 The experimental dependence of $[1 - \sigma(V = 0)]$ on $(1 - T/T_C)$ for the tin side of a proximity sandwich. 77

VI.10 Illustration of the occurence of multiple peak structure in the tunneling conductance between an ordinary superconductor and the S-side of an aluminum-tin proximity sandwich. 79

VI.11 Comparison of experimental and theoretical normalized conductance for tunneling from superconducting aluminum into the S-side of an aluminum-tin proximity sandwich. 80

VI.12 The experimental temperature dependence of peak positions in the S-side of a proximity sandwich. 82

A.III.1 The change of crystal frequency vs time for glow discharge oxidation at I = 3.5 mA. 101

A.III.2 The change of crystal frequency vs time for different oxidation runs plotted in terms of parabolic law. 106

A.III.3 The crystal frequency vs logarithm of time for the oxidation run with I = 3.5 mA. 107

A.IV.1 The geometry of interference fringes. 111

A.V.1 Oscillators for quartz crystal thickness monitor. 117

A.V.2 Circuit diagrams for quartz crystal thickness monitor. 118

A.VI.1 The level detecting capacitance probe. 121

A.VI.2 Circuit diagram of liquid level detector. 122

# CHAPTER I

## INTRODUCTION

Within the past few years there has been considerable interest in experiments on the proximity effect between normal (N) and superconducting (S) materials, usually prepared by evaporation.

Theoretical difficulties arise in calculating the superconducting properties of proximity sandwiches, because in such systems the order parameter is space dependent. Solutions have been obtained only in the vicinity of the critical temperature, $T_C$. The De Gennes - Werthamer theory, which is representative of this approach, has been quite well verified in the range of its validity by a number of experiments.

McMillan avoids the problem of a space dependent order parameter by assuming that the N and S films are weakly coupled and that each metal is sufficiently thin that the superconducting properties are constant across it. He is then able to obtain a complete solution for his model valid for all temperatures $T < T_C$. A few experimenters found qualitative agreement with the McMillan model, but their experiments did not quite fulfil the assumptions of the model.

The purpose of this theses is to test the validity of the McMillan model for aluminum-tin proximity sandwiches.

We have carried out self - consistent computer calculations of the McMillan model to obtain a detailed analysis of the tunneling density of states. The results for Al-Sn sandwiches are presented in Chapter III in graphical form.

The tunneling experiments have been performed into both sides of Al-Sn proximity sandwiches evaporated at room temperature onto an oxidized aluminum electrode which may be either normal or superconducting. The coupling between the N and S films was made weak by allowing slight oxidation to occur at the interface. Comparison of the experimental tunneling conductivity with the calculated one shows satisfactory quantitative agreement and the results are presented in Chapter VI.

Chapter II contains a brief review of previous work done on the proximity effect. In Chapters IV and V the technology of the tunnel junctions preparation, the apparatus used and the mean free path are discussed.

The results of Chapter III.2 and VI.2.a, b, and c will be published in the Physical Review (Vrba J., Woods S.B., April,1971).

Unless otherwise stated,the Gaussian units are used in the theses.

# CHAPTER II

# THE REVIEW OF PREVIOUS WORK ON PROXIMITY EFFECT

## II.1. General Considerations

When a superconductor is placed in very close contact with a normal metal, the properties of both are changed. The normal metal may become superconducting, while the transition temperature and gap of the superconductor are lowered. If two different superconductors are placed into proximity contact, their properties change and the resulting gap and critical temperature are somewhere in between the values of each superconductor.

The early experimental works of Meissner (1960) on contacts between crossed wires of tin plated with different metals, Rose-Innes and Serin (1961) on gold plates coated by evaporated tin, Smith et al (1961) on evaporated films of lead and silver, and of Simmons and Douglass (1962) on films of tin and silver aroused the interest of other investigators in the proximity effect.

We may divide the attempts to solve the problem of the proximity effect into two main groups:

(a) works dealing with the critical temperature of the layered structure only, and

(b) works dealing with the excitation spectrum of the layered structure.

The smallness of the order parameter $\Delta$ around the critical temperature $T_c$ has been employed in theoretical considerations included in group(a). Therefore the results from group(a) cannot be used at lower temperatures. Group (b) includes both works valid around $T_c$ only and works valid at all temperatures $T < T_c$.

Common to the theoretical approach to the proximity effect is the notion that superconductivity in bulk material is characterised by an electron pair correlation over a distance of the order of $10^{-4}$ to $10^{-5}$ cm and that this correlation should extend a similar distance into a normal metal in contact with a superconductor. Deutscher and De Gennes (1969) show that if normal metal is "clean", i.e., the mean free path $\ell_N$ is large compared to the coherence length $\xi_N$ , then the probability amplitude $F = < \psi\uparrow\psi\downarrow >$ for finding a Cooper pair at a distance $|X|$ from the N-S boundary has the form

$$F=\Phi(X)e^{-K|X|} \qquad \text{for } |X| \text{ large,} \qquad \text{II.1}$$

where $\Phi(X)$ is a slowly varying function of X and $K^{-1} = \hbar v_{FN}/ 2\pi k_B T$, $v_{FN}$ is the Fermi velocity in the N-film and T is the temperature. When T goes to zero then, as pointed out by Falk (1963), the decrease of F with X is very slow, approximately as 1/X. If the normal metal is dirty ( $\ell_N < \xi_N$ ), the leakage of Cooper pairs is ruled by a diffusion process and the exponential form II.1 still holds, but $K^{-1}$ is replaced by $\xi_N = (\hbar v_{FN}\ell_N / 6\pi k_B T)^{1/2}$.

## II.2. Critical Temperature of Proximity Sandwich.

A simple picture of the proximity effect was presented by Cooper (1961, 1962). He considers a normal metal of thickness $d_N$ in perfect contact ( no oxide barrier ) with a superconductor of thickness $d_S$, both with the same Fermi energy and the same electronic effective mass. Due to the coherence distance associated with zero momentum pairs, the superconducting correlation can extend into the volume of normal metal, so that a pair samples an effective attractive potential which is simply the spatial average of the potential on the two sides of the interface. Assuming that both $d_N$ and $d_S$ are smaller than the coherence lengths and that $[N(0)V]_N=0$ in the normal metal and $[N(0)V]_S \neq 0$ in the superconductor, Cooper writes for the effective BCS coupling constant of the proximity sandwich

$$[N(0)V]_{eff} = \frac{d_S}{d_S + d_N} [N(0)V]_S . \qquad \text{II.2}$$

The BCS relationship for the resulting critical temperature of the sandwich may be written

$$T_C = 1.14\hbar\omega_D e^{-\frac{1}{[N(0)V]_{eff}}} .$$

However in actual experiments some adsorbed gas is always present in between the two metals. These atoms form a barrier which tends to separate metals. Therefore one should expect that eq.II.2 gives the greatest possible reduction of the effective electron - electron interaction. Cooper suggests that the actual reduction factor should have the form

$$\frac{d_S}{d_S + \beta d_N}\ , \quad 0 \leqq \beta \leqq 1\ ,$$

where $\beta$ is determined by the barrier between the films.

A more detailed theory was developed by De Gennes and Guyon (1963) and De Gennes (1964a). They restricted their considerations to dirty films in which the mean free path $\ell$ is small compared to the coherence length $\xi$. They expect to get better agreement with theory for dirty systems ($\ell < \xi$) than for clean ones, because the detailed atomic situation at the interface in a dirty system is not important and large scale motion of superconducting electrons is ruled by the diffusion equation.

De Gennes (1964a) assumes that the electrons are coupled by a point interaction, $V(r_i)\delta(r_i - r_j)$. In the S-film he puts $V=V_S$ positive and in the N-film $V=V_N$ may have either sign. The interaction is cut off at frequency $\omega_D^S$ or $\omega_D^N$. He restricts all considerations to the vicinity of the transition temperature $T_C$ of the proximity sandwich and assumes that the pair potential $\Delta(\underset{\sim}{r})$ is small at all points in space when the temperature is close to the transition point ( this arises from the assumption that the superconductivity transition is of the second order). Then he treats $\Delta(\underset{\sim}{r})$ as a perturbation and is able to write a linear integral equation for $\Delta$ (in units $\hbar = k = c = 1$):

$$\Delta(\underset{\sim}{r}) = V(\underset{\sim}{r}) \sum_{\omega} \int d^3\underset{\sim}{r}'\Delta(\underset{\sim}{r}')H_{\omega}(\underset{\sim}{r},\underset{\sim}{r}') \ , \qquad \text{II.3}$$

$$H_{\omega}(\underset{\sim}{r},\underset{\sim}{r}') = T \sum_{\omega} \sum_{n,m} \frac{1}{\varepsilon_n - i\omega} \frac{1}{\varepsilon_m + i\omega} w_n^+(\underset{\sim}{r}) w_m^+(\underset{\sim}{r}) w_n(\underset{\sim}{r}') w_m(\underset{\sim}{r}') , \qquad \text{II.4}$$

where $\omega = 2\pi T\ (\nu + 1/2)$, $\sum_{\omega}$ represents a sum over all (positive or negative or zero) integers $\nu$ and $T$ is the temperature.

The functions $w_n$ are one-electron wave functions in the normal state defined by

$$\left[ \frac{p^2}{2m} + U(\underset{\sim}{r}) \right] w_n = \varepsilon_n w_n .$$

They include the effect of impurity and boundary scattering. The boundary conditions at the interface are

$$\begin{array}{ll} \Delta/NV & \text{continuous} \\ (D/V)\,d\Delta/dX & \text{continuous} \end{array} \qquad \text{II.5}$$

where $D = \frac{1}{3} v_F \ell$ and $N$ is the density of states at the Fermi energy in the normal state.

Applying the Cooper assumption De Gennes is able to derive the effective BCS coupling constant

$$[\,NV\,]_{eff} = \frac{V_N N_N^2 d_N + V_S N_S^2 d_S}{N_N d_N + N_S d_S} . \qquad \text{II.6}$$

Eq. II.6 differs from Cooper's eq. II.2 by the weighting factors which are, according to De Gennes, $d_N N_N$ and $d_S N_S$, while according to Cooper they are $d_N$ and $d_S$.

The early experiments by Smith et al (1961) on Pb - Ag systems and by Simmons and Douglass (1962) on Sn - Ag systems might be interpreted in terms of Cooper's approximation, but the mean free path and coherence length were not controlled and therefore the assumptions for approximation cannot be verified.

De Gennes makes the following approximation for N-S sandwiches with thicknesses $d_S$ and $d_N$ larger than the corresponding coherence lengths $\xi_N$ and $\xi_S$: in the kernel $H_\omega(\underset{\sim}{r},\underset{\sim}{r}')$ (eq. II.4) he retains only the lowest frequency component $H_{\omega_0}$ ($\omega_0 = \pm\pi T$) for which the kernel has maximum range. All other components are replaced by suitable normalized $\delta$ functions. He is then able to derive the critical temperature $T_C$ of the sandwich (in units $\hbar=k=c=1$),

$$T_C = T_{lim} + \pi D_S \frac{b_\infty}{(d_S+b_\infty)^3} e^{-2Kd_N}, \qquad \text{II.7}$$

where $T_{lim}$ is the critical temperature when $d_N \to \infty$, extrapolation length $b = D_S N_S \coth(Kd_N)/KD_N N_N$, $b_\infty = \lim_{d_N\to\infty} b$ and

$K^2 = \frac{2\pi T}{D_N}\left(1-\frac{2N_N V_N}{1-CN_N V_N}\right)$. Eq. II.7 was first proposed on a purely experimental basis by Hilsch (1962) for Cu - Pb sandwiches.

If there was a thin oxide layer between the N and S films, the temperature shift $T_C - T_{lim}$ would be reduced but the value of K would remain the same (De Gennes).

Thus K is a characteristic length which can be measured even in the presence of impurities in the interface ( as long as the impurity content is somehow kept unchanged from the sample to sample ).

Werthamer (1963) is able, by transforming the integral equation II.3 into a differential equation and assuming that the N - side has a small (negligible) critical temperature $T_{CN}$, to derive equations for the critical temperature $T_C$ of a superposed sandwich. The refined version by Hauser, Theuerer and Werthamer (1964) leads to

$$\begin{aligned} &N_S \xi_S^2 k_S \tan(k_S d_S) = N_N \xi_N^2 k_N \tanh(k_N d_N)\,, \\ &\chi(\xi_S^2 k_S^2) = \ln \frac{T_{CS}}{T_C}\,, \qquad -\chi(-\xi_N^2 k_N^2) = \ln \frac{T_C}{T_{CN}}\,, \\ &\text{and} \quad \chi(z) = \Psi(1/2+z/2) - \Psi(1/2)\,, \end{aligned} \qquad \text{II.8}$$

where $\Psi$ is digamma function (see e.g. Davis (1935)), $T_{CS}$ is the critical temperature of the S - film of the sandwich, and $\xi^2 = \hbar v_F \ell / 6\pi k_B T_C$ plays the role of coherence length.

Hauser et al (1964) used eqs. II.8 to interpret their data on the critical temperature of Cu - Pb and Pt - Pb sandwiches, and Hauser and Theuerer (1965) tested the validity of eqs. II.8 for two superconductors in proximity ( Pb - Al sandwich ). In both cases the agreement with theory was satisfactory. Hauser et al (1966) also extended eqs. II.8 for the superposed films of superconductor and magnetic film ( using the Abrikosov - Gor'kov model of superconductivity in dilute magnetic alloys ) and they found a reasonable agreement with experiment.

## II.3 Excitation Spectrum of Proximity Sandwich.

Fulde and Maki (1965), in order to explain the experiments of Woolf and Reif (1965) on superimposed films of superconductor and paramagnetic material, calculated the density of states in superimposed sandwiches of both superconductor and normal nonmagnetic metal and superconductor and magnetic metal. They obtained the expression for the density of states $N(\underset{\sim}{r},\omega)$ valid from both sides of the superimposed sandwich,

$$N(\underset{\sim}{r},\omega) = N(0)\left[1+ \frac{|\underset{\sim}{\Delta}(r)|^2}{2}\,\frac{\omega^2-\alpha^2}{(\omega^2+\alpha^2)^2}\right] , \qquad \text{II.9}$$

where $\alpha = \tau_{tr} v_F^2 k^2/6$, $\tau_{tr}$ is the transport collision time, and $k = k_S$ (or $k_N$) is determined by eqs. II.8. In case of a contact between a superconducting and a paramagnetic film the spin - flip scattering relaxation constant $\tau_s$ due to the paramagnetic ions is introduced and $k_N$ in eq.II.8 is replaced by $k_p$, for which new equation is valid :

$$-\chi\left( \frac{1}{\pi\tau_s T_C} - \xi^2 k_p^2\right) = \ln \frac{T_C}{T_{Cp}} .$$

Expression II.9 is equivalent to the one obtained by De Gennes (1964b) in the gapless region for superconductors with paramagnetic impurities or type II superconductors with $\alpha$ characterising the strength of the depairing effect.

De Gennes and Mauro (1965) pointed out that Fulde and Maki's derivation of eq. II.9 is valid only for homogeneous samples. They showed that the expansion of the density-of-states in powers of the order parameter $\Delta(\underset{\sim}{r})$ does not converge, but a similar expansion for the tunneling characteristic I(V) does converge at sufficiently high temperatures. Then Fulde and Maki's approximation is valid for $d_S > \sqrt{\hbar D_S/2\pi k_B T}$ for the S - film and for $d_N > (K-1/\xi_N)^{-1}$ for the N-film.

Their results were generalized and tested experimentally by Guyon et al (1966) for superimposed sandwiches of dirty films of InBi alloys and Zn. The agreement with the theory is very good. Claeson and Gygax (1966) and Claeson et al (1967) investigating the tunneling into Pb-Al, Pb-Ag, and Pb-Mn sandwiches and Hideki Tsuya (1967) investigating Ag-Sn, Ag-Pb, Fe-Sn, and Fe-Pb sandwiches found general agreement with the Fulde and Maki calculations.

McMillan (1968) circumvented the problems with the solution of integral equation II.3 for the pair potential $\Delta$ by proposing a simple, soluble tunneling model of proximity effect. The potential barrier is assumed to separate the N and S films and tunneling through this barrier is treated by the tunneling Hamiltonian method. Using this model McMillan was able to calculate the tunneling density of states in each film of an N - S sandwich for all temperatures $T < T_C$. The thickness of each film is assumed to be smaller than the corresponding coherence length and therefore the calculation does not involve the coherence length directly. Kaiser and Zuckermann (1970) extended the McMillan model to the case when the normal metal contains magnetic impurities. They also made a slight numerical correction to one relation among the model parameters.

Freake and Adkins (1969) measured the tunneling conductance between normal metal and Cu-Pb sandwiches at temperatures of 0.06° - 0.08°K. Adkins and Kington (1969) measured tunneling from normal aluminum into Ag-Pb, Cu-Pb, and Sn-Pb sandwiches.Both groups of authors found qualitative agreement with McMillan's predictions, which is as much as could be expected since their films were rather strongly coupled, and the theory only applies strictly to weak coupling between the two films.

## II.4 Experimental Difficulties.

To conclude this chapter the experimental difficulties connected with proximity effect experiments are discussed. All interpretations of the experimental results should be done with regard to these problems.

(a) As pointed out first by Rose-Innes and Serin (1961), the change of critical temperature of a superconductor evaporated on top of a normal metal may be caused by spurious interdiffusion effects. This effect was studied in more detail by Chiou and Klokholm (1964) on Ag-Sn sandwiches, Klokholm and Chiou (1964) on Au-Sn sandwiches, Caswell (1964) on Pb-Cu, Pb-Ag, and Pb-Au sandwiches and by Van Gurp (1963) on Sn-Al, In-Al, and In-Mg. It was concluded that when intermetallic compounds are known to exist the change of critical temperature is determined by the formation of compounds rather than by true proximity effect.

(b) Hilsch (1962) first observed irreversibility, i.e. the dependence of transition temperature of a sandwich on the order of deposition of the metals. Hauser et al (1966) argue on the basis of their improved experimental arrangement that the irreversibility is caused by strong dependence of resistivity (or mean free path) of the first few layers of a deposited film on the type of surface where growth is initiated. They rule out the possibility of a thin oxide layer at the film interface (Hauser et al (1964)). However on the basis of our experience gained during the present work we believe, that at least for metals which oxidize readily, the thin oxide layer in the N-S interface plays a very important role. Also experiments by Van Gurp (1963) on sandwiches containing aluminum, in which no proximity effect was observed, may be explained by the presence of a thin oxide layer rather than deformed structure of metals at the interface. Experiments by Miles and Smith (1963) on Al-In sandwiches (in which $T_C$ increased as the sandwiches were aged) may be explained on the basis of decoupling the metal films by the introduction of a gas layer in the interface.

(c) As pointed out first by Hilsch (1962), the resulting critical temperature of a proximity sandwich is strongly dependent on the mean free path in the normal metal. The mean free path is also embedded in the DeGennes-

Guyon-Werthamer theory for dirty superimposed metals. In McMillan's theory the exact theoretical dependence of proximity effect on mean free path is not known, but for constant ratio of the mean free path to the film thickness the effect is roughly insensitive to mean free path. The mean free path is usually measured from the residual low - temperature resistivity, but for thin evaporated films a few assumptions have to be made which are difficult to verify.

# CHAPTER III

## THE MCMILLAN TUNNELING MODEL OF PROXIMITY SANDWICHES

### III.1 Description of the Model

The following assumptions are made about the experimental system:

(a) A film of superconductor S of thickness $d_S$ is separated by a potential barrier with electron transmission probability $\alpha$ from a film of normal metal N (or different superconductor) with thickness $d_N$. The electron transmission probability $\alpha$ includes not only the effect of the oxide layer but also that of any impurity or imperfection at the interface of the two films. Thus even a "clean" interface might have $\alpha < 1$.

(b) The tunneling Hamiltonian is used to describe the penetration of electrons though the barrier, which restricts the transmission probability $\alpha$ to be much less than one.

(c) Both N and S are thin compared with the coherence length.

(d) The ratio of the mean free path $\ell$ to the film thickness is greater than or equal to unity.

Using this model, McMillan has derived the simultaneous self-energy equations for fixed BCS potentials $\Delta_S^{ph}$ and $\Delta_N^{ph}$ (in films S and N respectively) to be

$$\Delta_N(E) = \left(\Delta_N^{ph} + \frac{i\Gamma_N\Delta_S(E)}{[E^2-\Delta_S^2(E)]^{1/2}}\right)\bigg/\left(1 + \frac{i\Gamma_N}{[E^2-\Delta_S^2(E)]^{1/2}}\right),$$
$$\Delta_S(E) = \left(\Delta_S^{ph} + \frac{i\Gamma_S\Delta_N(E)}{[E^2-\Delta_N^2(E)]^{1/2}}\right)\bigg/\left(1 + \frac{i\Gamma_S}{[E^2-\Delta_N^2(E)]^{1/2}}\right). \qquad \text{III.1}$$

The self-consistency conditions for the BCS potentials at temperature T are

$$\Delta_N^{ph} = \lambda_N \int_A^B \mathrm{Re}\{ \frac{\Delta_N(E)}{[E^2-\Delta_N^2(E)]^{1/2}} \}\tanh \frac{E}{2kT}\, dE,$$
$$\Delta_S^{ph} = \lambda_S \int_C^D \mathrm{Re}\{ \frac{\Delta_S(E)}{[E^2-\Delta_S^2(E)]^{1/2}} \}\tanh \frac{E}{2kT}\, dE . \qquad \text{III.2}$$

The correct integration limits are $\Delta^{ph}$ and $[\omega_C^2+(\Delta^{ph})^2]^{1/2}$ but the contribution to the integrals is zero between zero and $\Delta^{ph}$, and $\Delta^{ph} << \omega_C$ so the limits may be written 0 and $\omega_C$, thus $B = \omega_C^N$, $D = \omega_C^S$, and $A = C = 0$.

The electronic density of states can be computed from

$$N_{S,N} = \mathrm{Re}\ \{\ |E|/[E^2-\Delta_{S,N}^2(E)]^{1/2}\}. \qquad \text{III.3}$$

In the above equations $\Gamma_S$ and $\Gamma_N$ fulfil the conditions correctly stated by Kaiser and Zuckermann

$$\Gamma_N = \pi M^2 A d_S N_S(0) = h/2\tau_N,$$
$$\Gamma_S = \pi M^2 A d_N N_N(0) = h/2\tau_S,$$

where M is the tunneling matrix element, A is the area of the junction, $N_{N,S}(0)$ is the density of states at the Fermi level in the normal state, and $\tau_{N,S}$ are relaxation times in the normal and superconducting material respectively.

The average time $\tau_{N,S}$ which an electron spends in the N or S film respectively may be written as

$$\tau_{N,S} = L_{N,S}/v_{FN,S}\alpha ,$$

where $v_{FN,S}$ is the Fermi velocity and $L_{N,S}$ is the average electron path length between collisions with the barrier in the N or S film respectively.

$L_{N,S} = 4d_{N,S}$ if the following conditions are fulfilled: (1) the mean free path $\ell_{N,S}$ is infinite and (2) the probability that an electron penetrates the barrier to enter the film at an angle $\Theta$ to the normal obeys the cosine law (see Appendix I). For a film which does not fulfil these conditions, we may write

$$L_{N,S} = 2B_{N,S}\left( \frac{\ell_{N,S}}{d_{N,S}} \right) d_{N,S} ,$$

where B is a function of the ratio of the mean free path to the film thickness. Also, we can write

$$\Gamma_N = \frac{\hbar v_{FN}\alpha}{4B_N d_N} \quad \text{and} \quad \Gamma_S = \frac{\hbar v_{FS}\alpha}{4B_S d_S} \quad . \qquad \text{III.4}$$

A maximum practical value for these parameters is $\Gamma \simeq 10$ meV. This is obtained with $d \simeq 15$ Å (where our films became continuous), $v_F \simeq 10^8$ cm/sec, $B_N = 2$, and $\alpha \simeq 0.1$.

When it is assumed that $v_{FN} = v_{FS}$ and $B_N = B_S$, then $\Gamma_S/\Gamma_N = d_N/d_S$ and $\Gamma_{N,S} \propto \alpha/d_{N,S}$.

These simplified relations facilitate a physical understanding of the results of computations using the McMillan model.

## III.2 Computer Calculations with the Model for Aluminum - Tin Sandwiches

We have carried out detailed computer calculations for the aluminum-tin proximity sandwich with an analysis of the tunneling density of states from both sides of the sandwich. The results are presented here in graphical form. We refer to aluminum as the normal metal (even if it is a superconductor) and tin is the superconductor. The calculations have been done for the thickness range $d_N < d_S$ for the aluminum side of the sandwich and for the thickness range $d_N > d_S$ for the tin side of the sandwich.

The interesting feature of the McMillan model is the double-peaked density of states that appears in the aluminum side of the sandwich when $d_N < d_S$ $(\Gamma_S/\Gamma_N < 1)$ and $\alpha$ is small, and in the tin side of the sandwich for all ratios of the thicknesses as soon as $\alpha$ is sufficiently small. In the N-side when $d_N$ approaches $d_S$ $(\Gamma_S/\Gamma_N \rightarrow 1)$ the peak P2 (see Fig.III.1) is very small and not observable, but when $\alpha$ is increased, the density of states exhibits a broad single peak. The exact shape and energy position of the peaks depends on parameters $\Gamma_S$, $\Gamma_N$, $\Delta_S^{ph}$, and $\Delta_N^{ph}$. The situation in the N-film is illustrated in Fig.III.1 for

FIG. III.1

The McMillan normalized density of states in the N-side of an aluminum - tin proximity sandwich at fixed values of the potentials $\Delta_S^{ph}$ = 1.0meV, $\Delta_N^{ph}$ = 0.1 meV and $B_N = B_S = 2$, $v_{FN} = v_{FS}$ = 10 cm$^8$sec$^{-1}$ and

| | $d_S$(Å) | $d_N$(Å) | $\Gamma_S$(meV) | $\Gamma_N$(meV) | $\Gamma_S/\Gamma_N$ | $\alpha$ |
|---|---|---|---|---|---|---|
| a | 75 | 75 | 0.2 | 0.2 | 1.0 | 0.02 |
| b | 750 | 75 | 0.02 | 0.2 | 0.1 | 0.02 |
| c | 7500 | 75 | 0.002 | 0.2 | 0.01 | 0.02 |
| d | 75 | 75 | 2.0 | 2.0 | 1.0 | 0.2 |
| e | 750 | 75 | 0.2 | 2.0 | 0.1 | 0.2 |
| f | 7500 | 75 | 0.02 | 2.0 | 0.01 | 0.2 |

For higher $\alpha$ the peaks are closer together and larger $d_S$ is required to resolve the double-peaked structure.

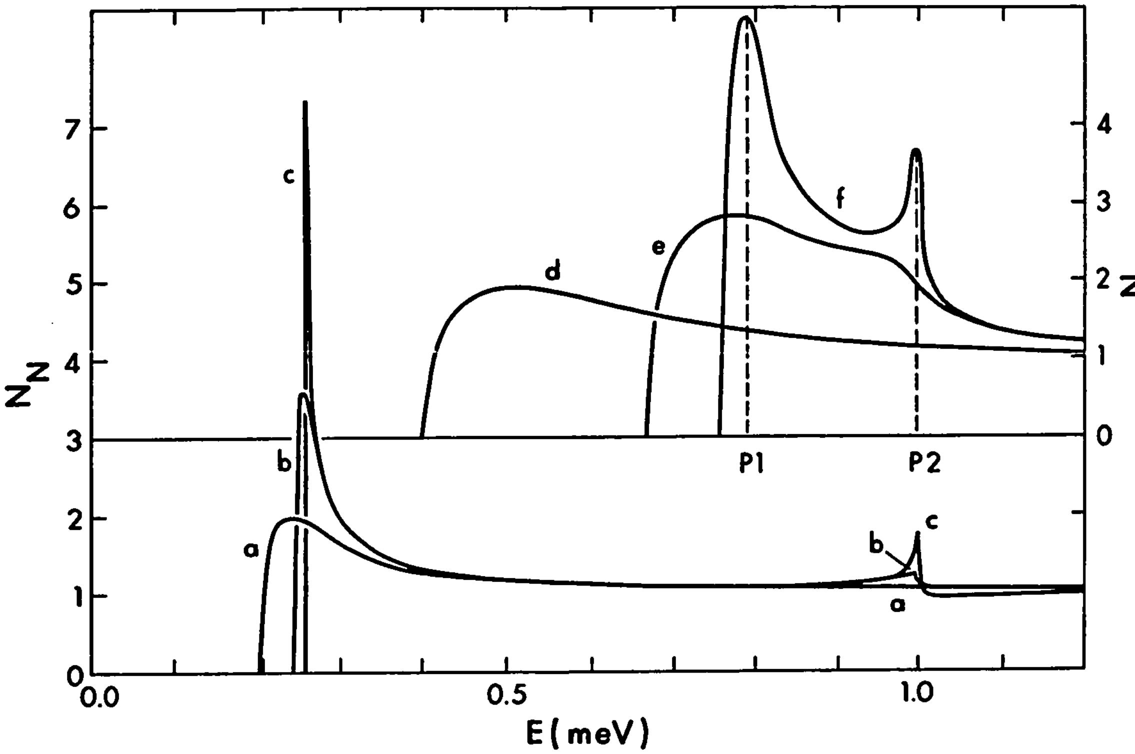

7
6
5
4
3
2
1
0
$N_N$
4
3
2
1
0
$N_N$
c
b
a
d
e
f
P1
P2
b
c
a
0.0
0.5
1.0
E(meV)

two different values of $\alpha$, and for the S-film in Fig.III.2 for three different values of $\alpha$. The curves in Figs.III.1 and III.2 were calculated using eqs.III.1, fixed potentials $\Delta_S^{ph} = 1$ meV, and $\Delta_N^{ph} = 0.1$ meV, and the simplifying conditions $B_S = B_N = 2$ and $v_{FN} = v_{FS} = 10^8$ cm/sec.

The appearance of the double-peaked structure may be understood qualitatively in terms of two effects that the presence of each metal has on the other. First, the wave functions of the excitations in the tin are coupled into the aluminum creating a peak in the aluminum density of states near $\Delta_S^{ph}$, and the wave functions of the excitations in aluminum are coupled into tin creating a peak in the tin density of states near $\Delta_N^{ph}$; second, as $\alpha$ increases the pairing energies in the two metals move toward a common value determined largely by the thicker metal. Thus for $d_S > d_N$ the low energy excitation peak in aluminum moves to higher energies as $\alpha$ increases, and also the eigenstates of the system become less well defined, so that the peaks gradually broaden and merge. Similarly for $d_N > d_S$ the high energy excitation peak in tin moves to lower energies as $\alpha$ increases.

The temperature variation of the peak positions and of the BCS potentials, $\Delta_S^{ph}$ and $\Delta_N^{ph}$, can be calculated by combining the self-energy eq.III.1 with the self-consistent condition expressed by eq.III.2. For aluminum and tin the bulk values $\lambda_N = 0.171$, $\omega_C^N = 32.21$ meV, $\lambda_S = 0.246$, and $\omega_C^S = 16.78$ meV were substituted. The situation for $d_N < d_S$

FIG. III.2

The McMillan normalized density of states in the S-side of an aluminum - tin proximity sandwich at fixed values of the potentials $\Delta_S^{ph} = 1.0$ meV, $\Delta_N^{ph} = 0.1$ meV and $B_N = B_S = 2$, $v_{FN} = v_{FS} = 10$ cm$^8$sec$^{-1}$ and

| | $d_S$ (Å) | $d_N$ (Å) | $\Gamma_S$ (meV) | $\Gamma_N$ (meV) | $\Gamma_S/\Gamma_N$ | $\alpha$ |
|---|---|---|---|---|---|---|
| a | 75 | 7.5 | 0.02 | 0.2 | 0.1 | 0.002 |
| b | 75 | 75 | 0.02 | 0.02 | 1 | 0.002 |
| c | 75 | 750 | 0.02 | 0.002 | 10 | 0.002 |
| d | 75 | 75 | 0.2 | 0.2 | 1 | 0.02 |
| e | 75 | 750 | 0.2 | 0.02 | 10 | 0.02 |
| f | 75 | 7500 | 0.2 | 0.002 | 100 | 0.02 |
| g | 75 | 750 | 2.0 | 0.2 | 10 | 0.2 |
| h | 75 | 7500 | 2.0 | 0.02 | 100 | 0.2 |

At a given value of $\alpha$ the shape of peak structure is almost insensitive to the actual thickness of the films. For clarity the origin $N_S = 0$ is displaced for different curves. The results of this figure and Fig.III.1 are not to be mixed with the selfconsistent discussion in page 20.

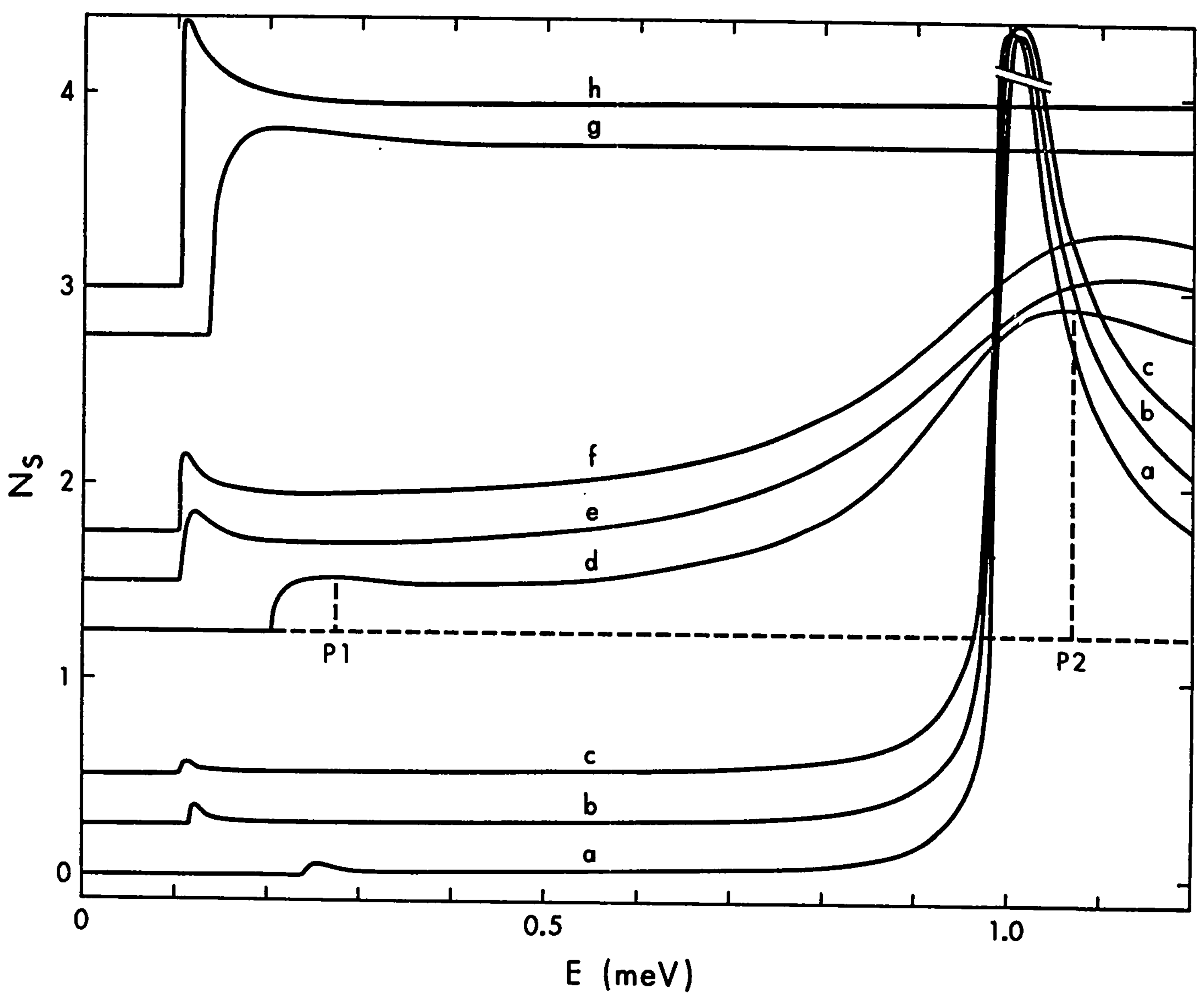

N_S
4
3
2
1
0
0
0.5
1.0
E (meV)
h
g
f
e
d
c
b
a
c
b
a
P1
P2

is shown in Fig.III.3. The calculations were done for the ratio $\Gamma_S/\Gamma_N = 0.1$. It can be seen that for weak coupling between the films (case a) the higher energy peak $P2 \simeq \Delta_S^{ph}$ follows closely the BCS temperature variation of the tin gap, while the lower energy peak P1 and $\Delta_N^{ph}$ at low temperature follow the BCS temperature dependence for the aluminum gap, but deviate progressively as the temperature is raised and finally approach zero at $T_C$ of the overall sandwich. As the interaction between the films is made stronger, (cases b and c in that order), the value of $P2 \simeq \Delta_S^{ph}$ is lowered for all temperatures, while P1 and $\Delta_N^{ph}$ are shifted to higher energies. The critical temperature of the sandwich is very close to the critical temperature of pure tin.

The temperature variation of the peak positions, of $\Delta_S^{ph}$, and $\Delta_N^{ph}$ for $d_N > d_S$ is shown in Fig.III.4. The calculations were done for the ratio $\Gamma_S/\Gamma_N = 5$. Qualitatively the same general behaviour of the peak positions, $\Delta_S^{ph}$, and $\Delta_N^{ph}$ as in Fig.III.3 is observed, but in this case the critical temperature of the sandwich is very much different from the critical temperature of pure tin.

When the superconductor is very little disturbed by proximity effect (that is, either $d_N << d_S$ or $\alpha$ is very small) the temperature dependence of $\Delta_S^{ph}$ is well approximated by the BCS relationship for $\Delta(T)/\Delta(T=0)$, so that the critical temperature $T_C$ of the sandwich may be

FIG. III. 3

Temperature variation of the peaks P1 and P2 in the density of states in the aluminum side of an aluminum-tin proximity sandwich and the potentials $\Delta_S^{ph}$ and $\Delta_N^{ph}$ when $d_N < d_S$.

Bulk values $\omega_c^N = 32.21$ meV, $\lambda_N = 0.171$ were used for aluminum; $\omega_c^S = 16.78$ meV, $\lambda_S = 0.246$ for tin. $\Gamma_S/\Gamma_N = 0.1$ for all curves, $\Gamma_N = 0.005$ meV for a, $\Gamma_N = 0.05$ meV for b, $\Gamma_N = 0.5$ meV for c. $\Delta_S^{ph}$ is usually indistinguishable from P2. BCS variation of the tin gap is indistinguishable from $\Delta_{Sa}^{ph}$. $T_C = 3.80$°K for a, $T_C = 3.77$°K for b, $T_C = 3.69$°K for c. These critical temperatures were obtained using eq.III.5.

----- BCS variation of the aluminum gap.

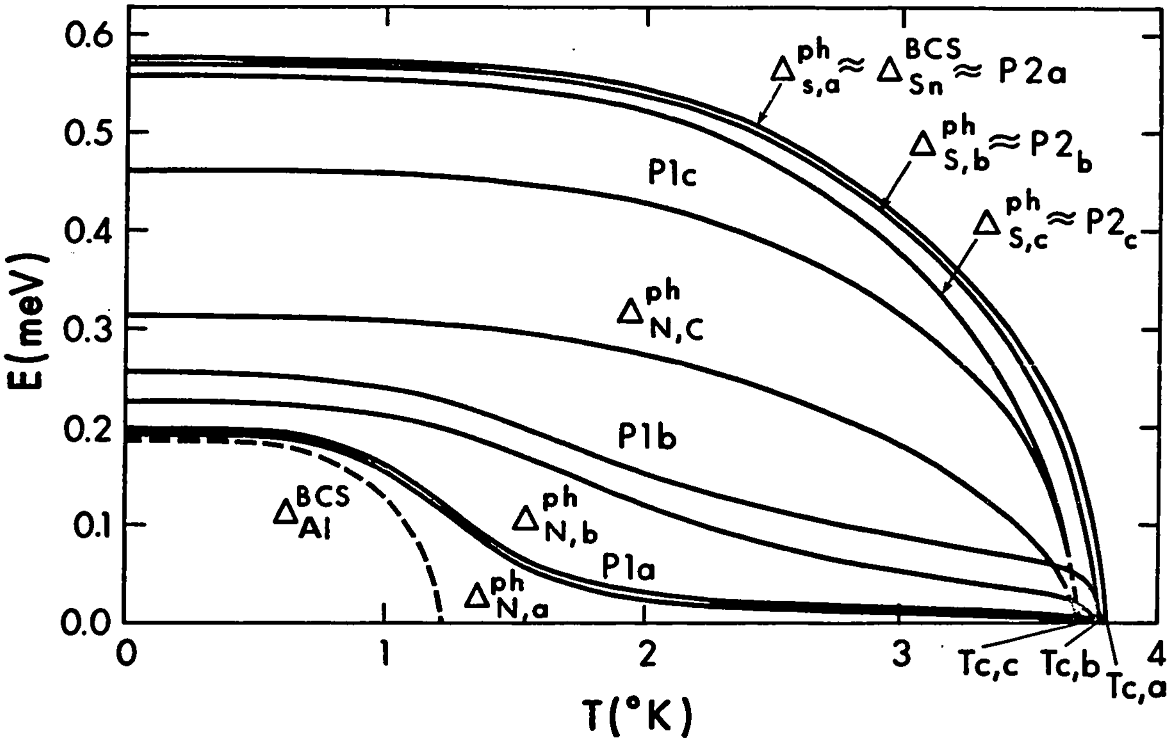

0.6
0.5
0.4
0.3
0.2
0.1
0.0
E(meV)
0
1
2
3
4
T(°K)
$\Delta^{ph}_{s,a} \approx \Delta^{BCS}_{Sn} \approx P2a$
$\Delta^{ph}_{S,b} \approx P2_b$
$\Delta^{ph}_{S,c} \approx P2_c$
P1c
$\Delta^{ph}_{N,C}$
P1b
$\Delta^{BCS}_{Al}$
$\Delta^{ph}_{N,b}$
P1a
$\Delta^{ph}_{N,a}$
Tc,c
Tc,b
Tc,a

FIG. III. 4

Temperature variation of the peaks P1 and P2 in the density of states in the tin side of an aluminum - tin proximity sandwich and the potentials $\Delta_S^{ph}$ and $\Delta_N^{ph}$ when $d_N > d_S$.

Bulk values $\omega_c^N$ = 32.21 meV, $\lambda_N$ = 171 were used for aluminum; $\omega_c^S$ = 16.78 meV, $\lambda_S$ = 0.246 for tin. $\Gamma_S/\Gamma_N$ = 5 for all curves, $\Gamma_S$ = 0.005 meV for a, $\Gamma_S$ = 0.05 meV for b, and $\Gamma_S$ = 0.5 meV for c. BCS variation of the tin gap is indistinguishable from $\Delta_{Sa}^{ph}$ . $T_C$ = 3.80°K for a , $T_C$ = 3.42°K for b , and $T_C$ = 1.78°K for c .

------ BCS variation of aluminum gap.

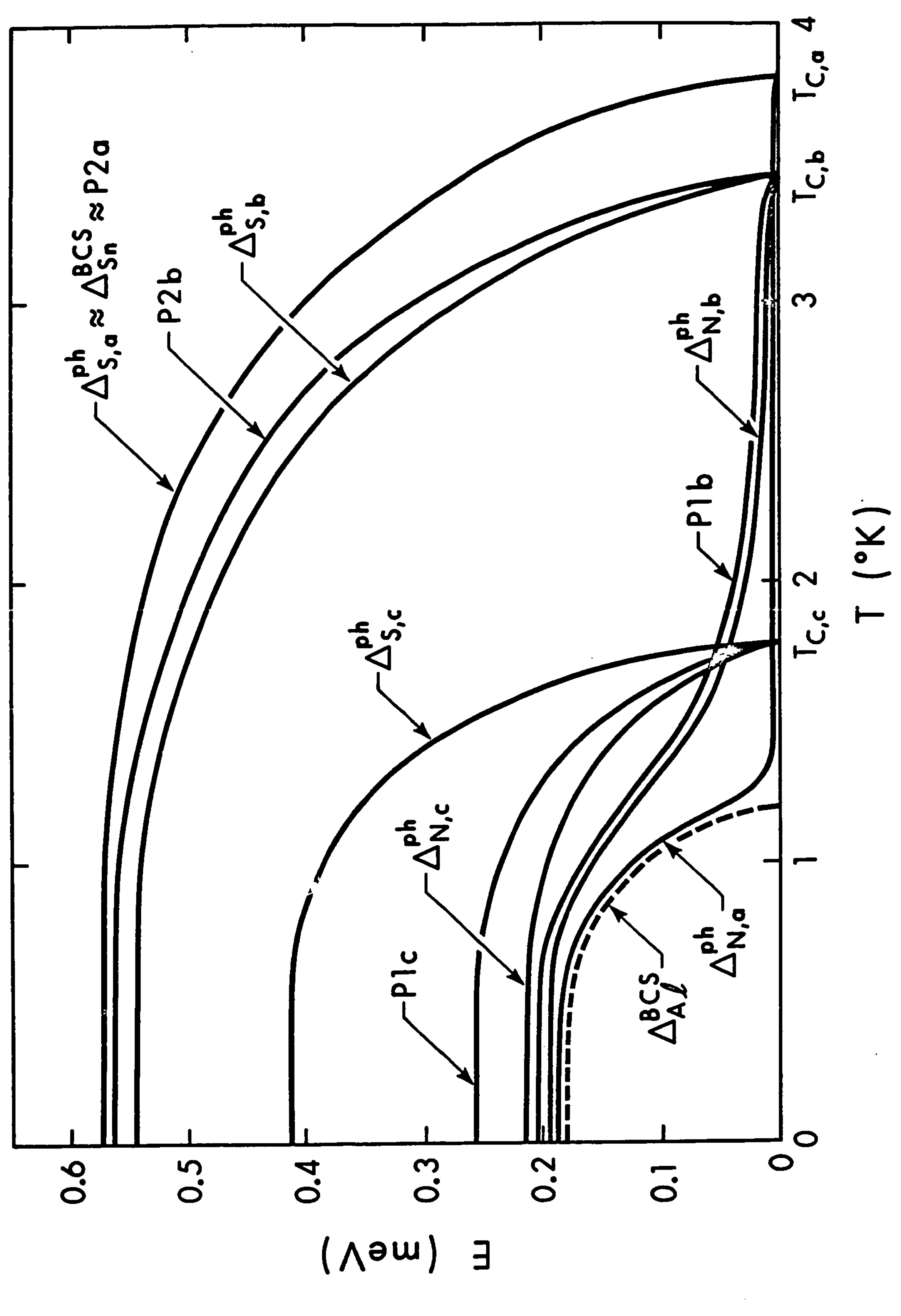

$\Delta^{ph}_{S,a} \approx \Delta^{BCS}_{Sn} \approx P2a$
P2b
$\Delta^{ph}_{S,b}$
$\Delta^{ph}_{S,c}$
$\Delta^{ph}_{N,c}$
P1c
P1b
$\Delta^{ph}_{N,b}$
$\Delta^{BCS}_{A\ell}$
$\Delta^{ph}_{N,a}$
$T_{C,c}$
$T_{C,b}$
$T_{C,a}$
0
1
2
3
4
T (°K)
E (meV)
0
0.1
0.2
0.3
0.4
0.5
0.6

found from the BCS relationship

$$2\Delta_S^{ph}(T = 0) \; / \; kT_C \simeq 3.5 \qquad \text{III.5}$$

This is the case for the curves in Fig.III.3 and for curve a in Fig.III.4. When the conditions for the approximation III.5 are not fulfilled, we may estimate $T_C$ directly from plots similar to Figs.III.3 and III.4, or use the approximation suggested by Mr.R.Teshima (see Appendix II), which enables us to calculate $T_C$ directly. (Direct calculation of $T_C$ from the self-consistent eqs.III.2 cannot be done because convergence of the iteration method that was used is very slow around $T_C$). The results of Teshima's approximation (full line) and the estimation of $T_C$ from Figs.III.3 and III.4 or from the approximation III.5, when applicable, are plotted vs $\Gamma_N$ in Fig.III.5. One can see that Teshima's approximation and the approximation III.5 agrees within 2% (curves for $\Gamma_S/\Gamma_N$ = 0.1, 0.05, and 0.01). Estimation of $T_C$ from plots similar to Figs.III.3 and III.4 differs from Teshima's approximation at most by about 0.2°K (curves for $\Gamma_S/\Gamma_N$ = 0.5, 1, 5, and 10), but one has to keep in mind the poor accuracy of the $T_C$ estimated from Figs.III.3 and III.4. We regard Teshima's approximation as satisfactory.

Each line of constant $\Gamma_S/\Gamma_N$ in Fig.III.5 is a line for constant ratio of thicknesses $d_N/d_S$. $\Gamma_N$ may then be increased, while keeping $d_N$ constant, by the increasing $\alpha$, that is, producing a cleaner interface. We see that at

FIG. III.5

The critical temperature, $T_C$, of an aluminum-tin proximity sandwich plotted vs $\Gamma_N$. The parameter is $\Gamma_S/\Gamma_N$.

| | |
|---|---|
| ———— | Teshima's approximation, |
| ■, ▲, □, ◆ | estimate from plots similar to Figs. III. 3 and III.4, |
| ●, △, ○ | estimate using approximation eq. III.5. |

The meaning of the symbols is as follows:

| | $\Gamma_S/\Gamma_N$ | | $\Gamma_S/\Gamma_N$ |
|---|---|---|---|
| ● | 0.01 | ▲ | 1.0 |
| △ | 0.05 | □ | 5.0 |
| ○ | 0.1 | ◆ | 10.0 |
| ■ | 0.5 | | |

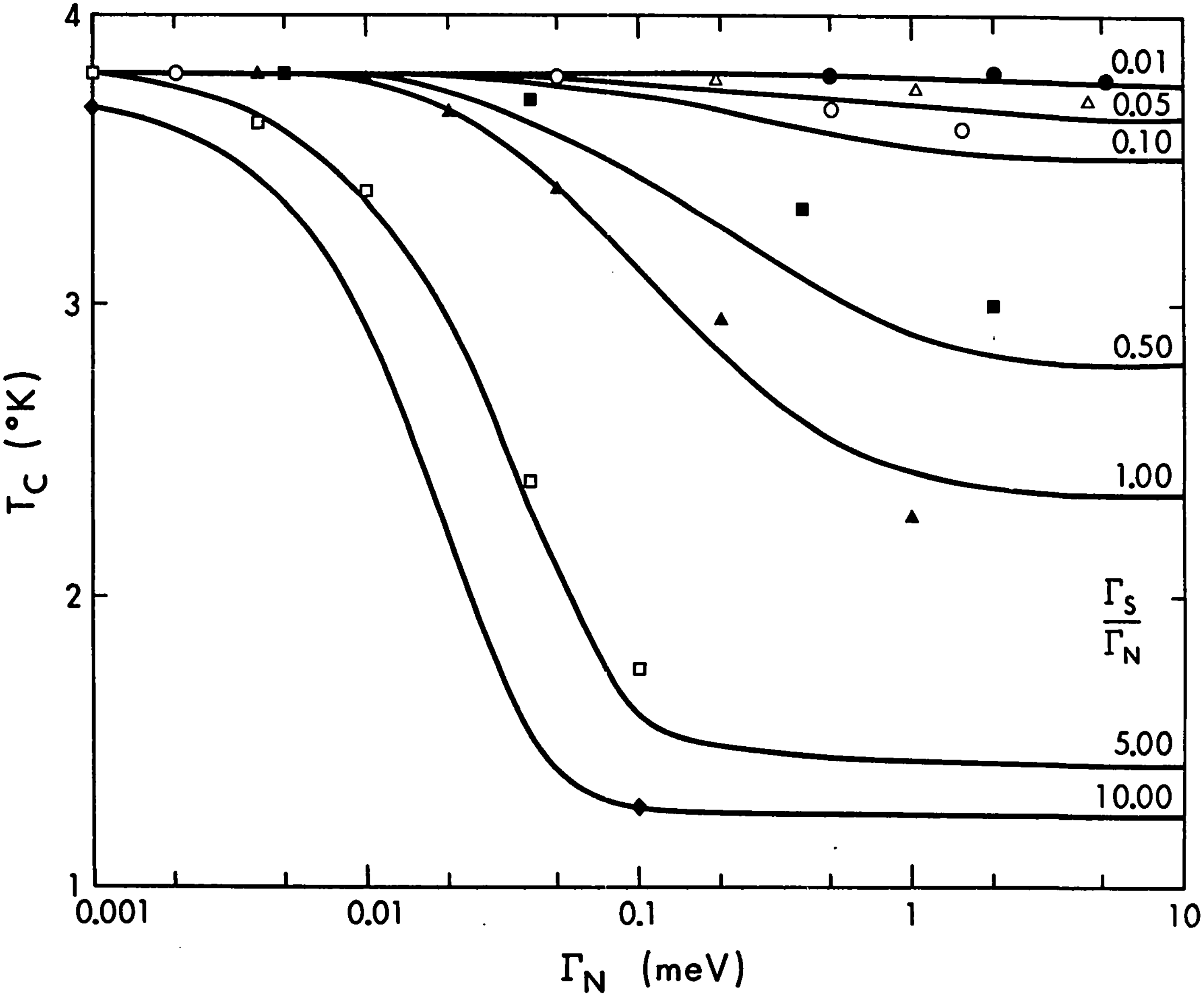
4
3
2
1
$T_C$ (°K)
0.001
0.01
0.1
1
10
$\Gamma_N$ (meV)
0.01
0.05
0.10
0.50
1.00
$\frac{\Gamma_S}{\Gamma_N}$
5.00
10.00

fixed thicknesses, $d_N$ and $d_S$, the critical temperature $T_C$ approaches a constant limiting value as the interface is made cleaner (higher $\Gamma_N$). The value of $T_C$ when the interface is clean, therefore depends only on the ratio of thicknesses $d_N/d_S$ ($\simeq \Gamma_S/\Gamma_N$) and does not depend on $\alpha$. This behaviour of $T_C$ is similar to the behaviour of the Cooper model of the proximity effect with a perfectly clean interface (see eq.II.2), which is also dependent on the ratio of thicknesses only.

When self-consistent values of $\Delta_N^{ph}$ and $\Delta_S^{ph}$, and of peak positions and peak separations in the N side of the proximity sandwich are plotted against $\Gamma_N$ for different ratios $\Gamma_S/\Gamma_N$, one finds a very important result. When $d_N < d_S$ the properties of the system, shown in Fig.III.6a, b, c, are independent of $\Gamma_S$ (and therefore of $B_S$ or $d_S$) over a wide range of $\Gamma_N$. This feature is used for evaluation of our experimental data. In Fig.III.6d $\Delta_S^{ph}$ and $\Delta_N^{ph}$ are shown as functions of $\Gamma_S$ for different ratios of $\Gamma_S/\Gamma_N$ to emhasize that these properties are much more dependent on $\Gamma_N$ than on $\Gamma_S$.

On the other hand, when $d_S < d_N$, the situation is reversed and, as shown in Fig.III.7a, $\Delta_N^{ph}$ and $\Delta_S^{ph}$ are relatively independent of $\Gamma_N$ ( and therefore of $B_N$ or $d_N$). In Fig.III.7b these quantities are plotted against $\Gamma_N$ to emphasize that they depend more strongly on $\Gamma_S$ than on $\Gamma_N$. In Fig.III.7c and d the peak positions in the S-side of the proximity sandwich are plotted vs $\Gamma_S$ at 1.0°K and at 1.4°K.

FIG. III.6

The self-consistent calculations of the McMillan model for an aluminum-tin sandwich when $d_N < d_S$.

(a) Peak positions in the N side as a function of $\Gamma_N$.

(b) Peak separation in the N side determined from (a) as a function of $\Gamma_N$.

(c) Values of potentials $\Delta_S^{ph}$ and $\Delta_N^{ph}$ as a function of $\Gamma_N$.

(d) the same as (c) but as a function of $\Gamma_S$. The properties of the system are weakly dependent on $\Gamma_S$ whereas the strong dependence on $\Gamma_N$ is emphasized in (d).

All curves are plotted at 1.4°K.

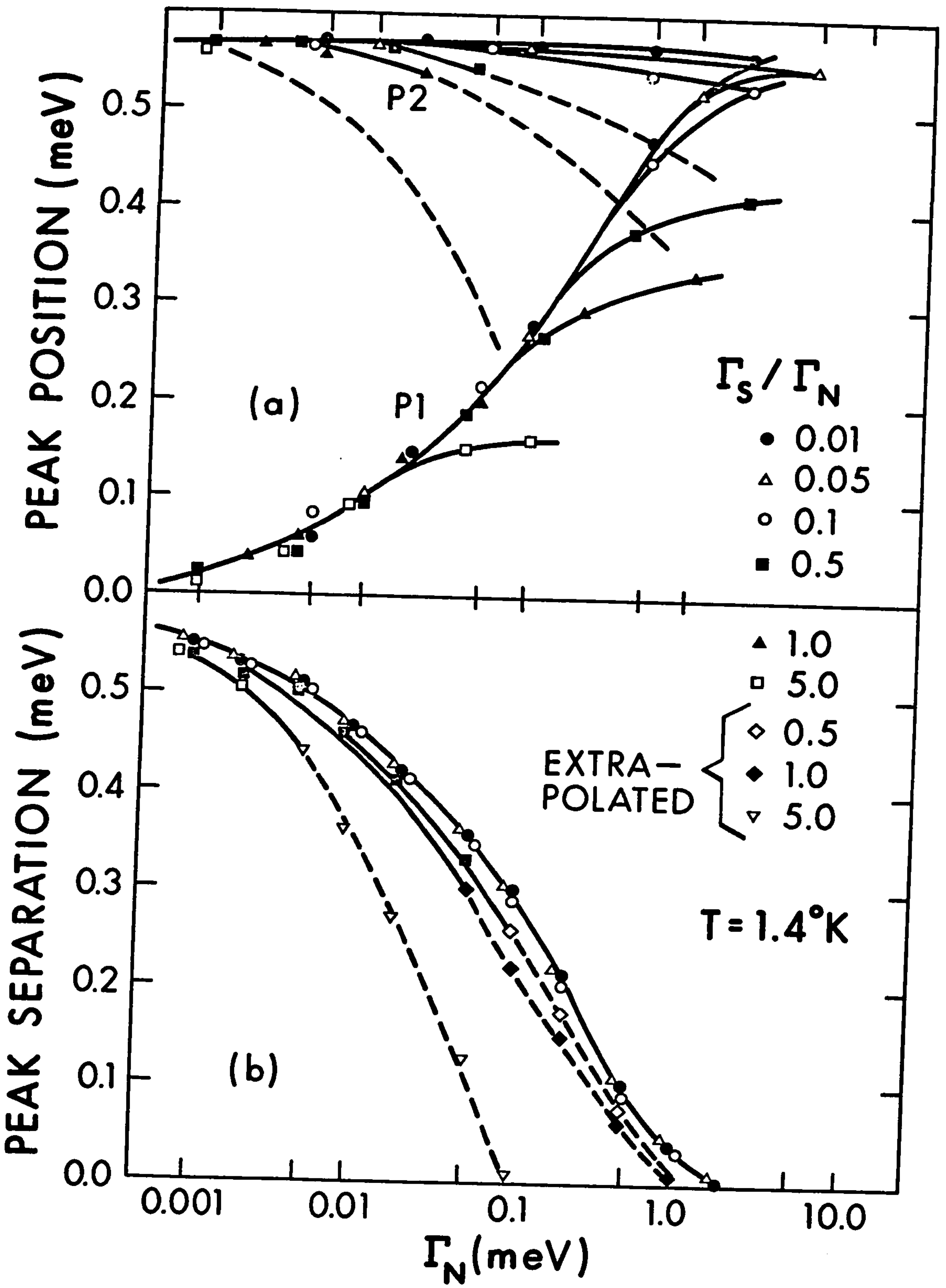
PEAK POSITION (meV)
0.0
0.1
0.2
0.3
0.4
0.5
P2
P1
(a)
Γ_S / Γ_N
● 0.01
△ 0.05
○ 0.1
■ 0.5
▲ 1.0
□ 5.0
EXTRA-POLATED
◇ 0.5
◆ 1.0
▽ 5.0
T = 1.4°K
PEAK SEPARATION (meV)
0.0
0.1
0.2
0.3
0.4
0.5
(b)
0.001
0.01
0.1
1.0
10.0
Γ_N (meV)

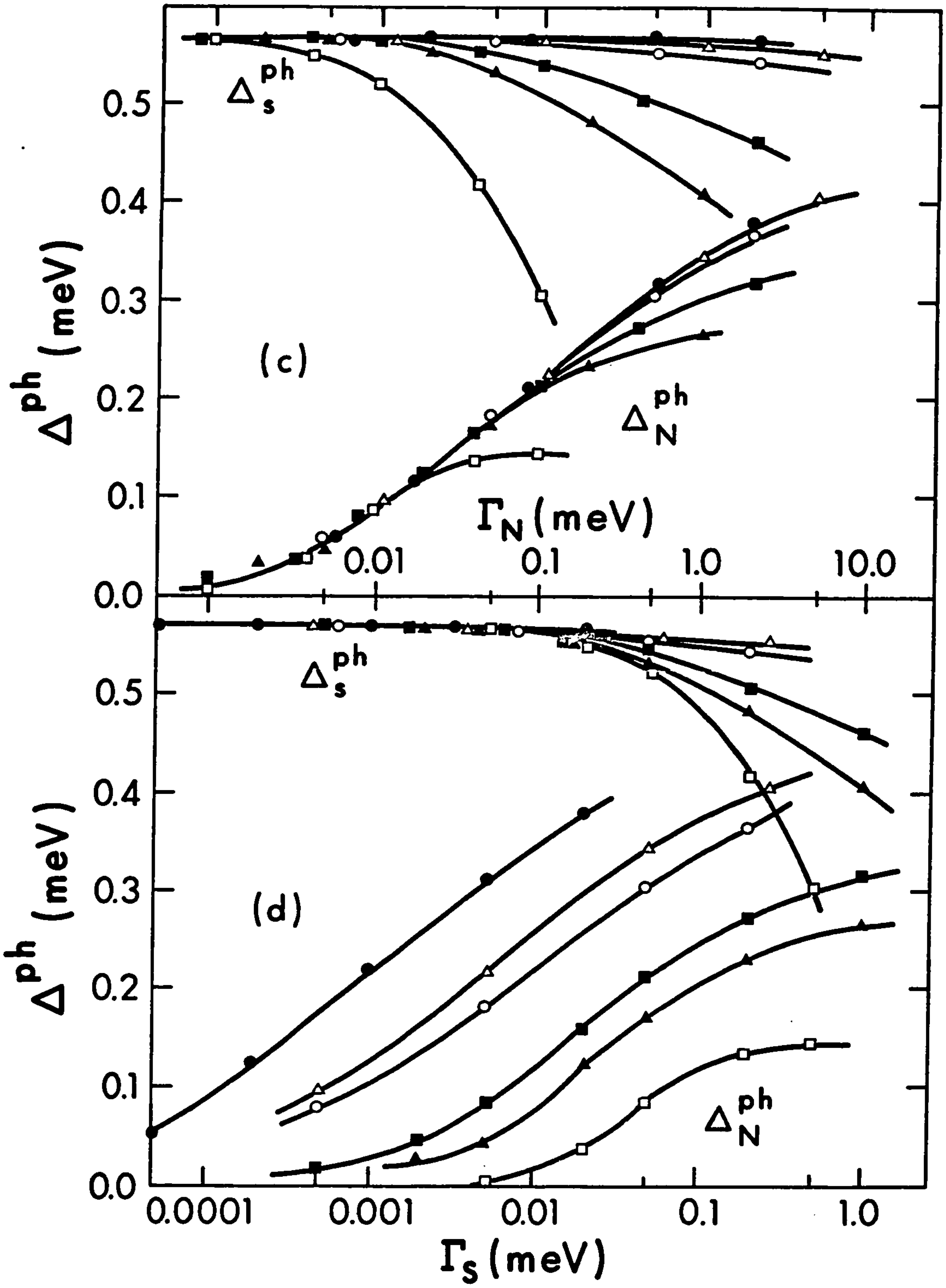

(c)
$\Delta_s^{ph}$
$\Delta_N^{ph}$
$\Delta^{ph}$ (meV)
$\Gamma_N$ (meV)
0.0
0.1
0.2
0.3
0.4
0.5
0.01
0.1
1.0
10.0
(d)
$\Delta_s^{ph}$
$\Delta_N^{ph}$
$\Delta^{ph}$ (meV)
0.0
0.1
0.2
0.3
0.4
0.5
0.0001
0.001
0.01
0.1
1.0
$\Gamma_S$ (meV)

FIG. III.7

The self-consistent calculations of the McMillan model for an aluminum - tin sandwich when $d_N > d_S$.

(a) Values of potentials $\Delta_S^{ph}$ and $\Delta_N^{ph}$ as a function of $\Gamma_S$ at 1.0°K.

(b) The same as (a) but as a function of $\Gamma_N$.

(c) Peak positions in the S - side as a function of $\Gamma_S$ at 1.0°K.

(d) Peak positions in the S - side as a function of $\Gamma_S$ at 1.4°K.

▲ $\Gamma_S/\Gamma_N = 1$, □ $\Gamma_S/\Gamma_N = 5$, ◆ $\Gamma_S/\Gamma_N = 10$, and ◇ $\Gamma_S/\Gamma_N = 50$.

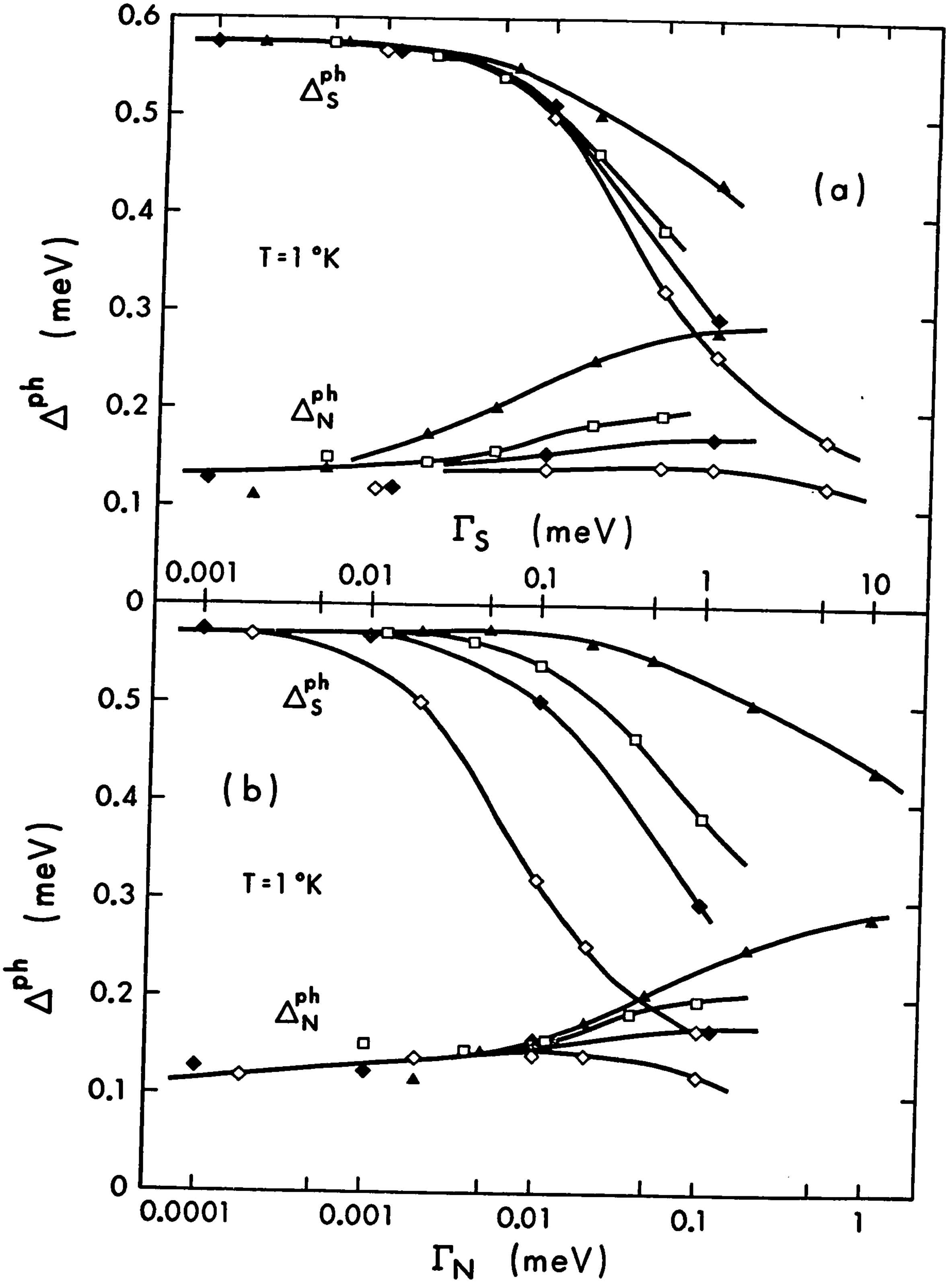
0.6
0.5
0.4
0.3
0.2
0.1
0
$\Delta^{ph}$ (meV)
$\Delta_S^{ph}$
$\Delta_N^{ph}$
T = 1 °K
(a)
$\Gamma_S$ (meV)
0.001
0.01
0.1
1
10
0.5
0.4
0.3
0.2
0.1
0
$\Delta^{ph}$ (meV)
$\Delta_S^{ph}$
$\Delta_N^{ph}$
(b)
T = 1 °K
0.0001
0.001
0.01
0.1
1
$\Gamma_N$ (meV)

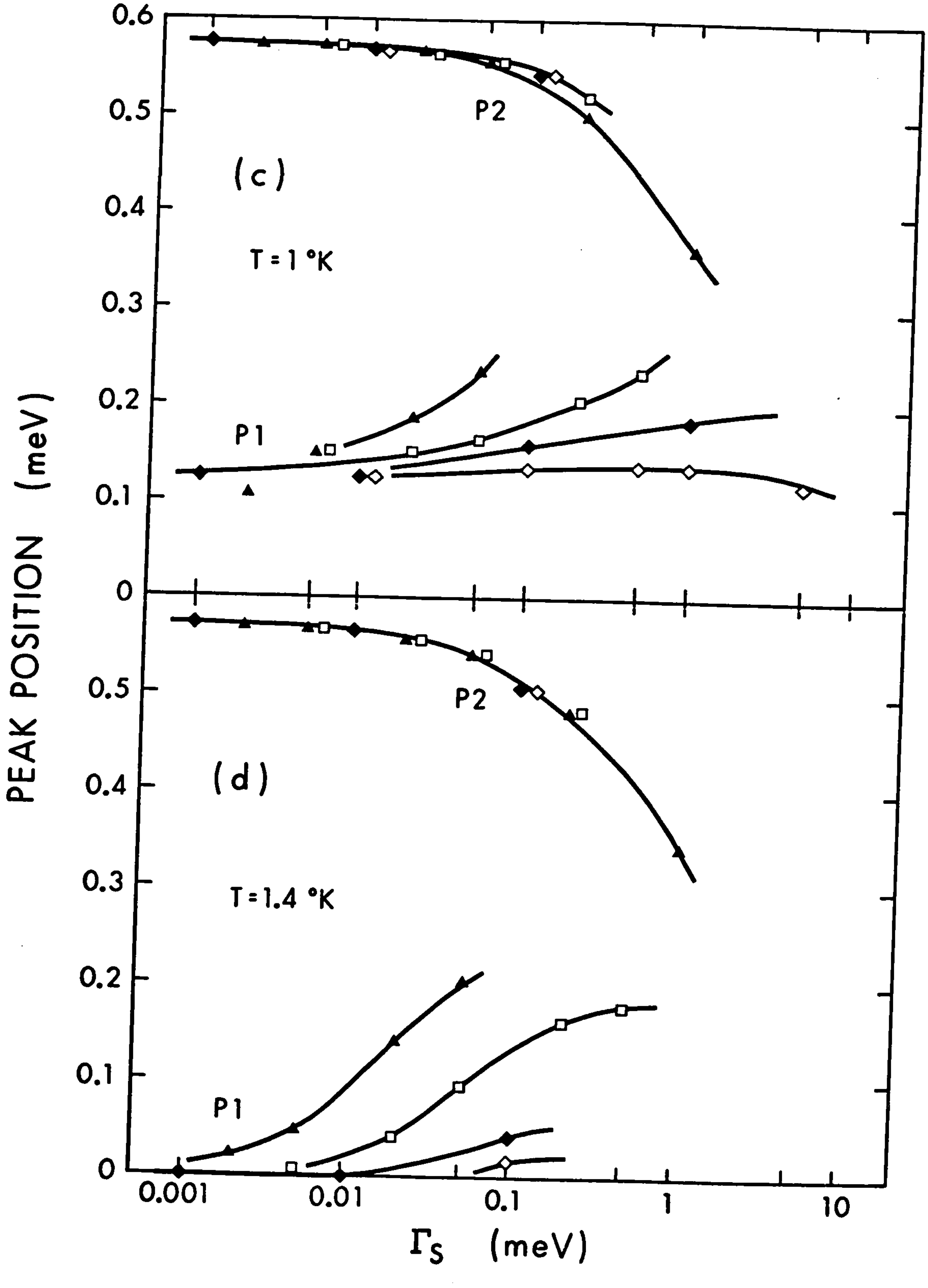

0.6
0.5
0.4
0.3
0.2
0.1
0
P2
(c)
T = 1 °K
P1
0.5
0.4
0.3
0.2
0.1
0
P2
(d)
T = 1.4 °K
P1
PEAK POSITION (meV)
0.001
0.01
0.1
1
10
$\Gamma_S$ (meV)

The dependences in Figs.III.6 and III.7c are plotted for a temperature of 1.4°K (above the critical temperature of aluminum) while in Fig.III.7a, b, and d they are plotted for 1°K, which is below the critical temperature of aluminum. Therefore $\Delta_N^{ph}$ and peak positions approach zero at extremely weak coupling (small $\Gamma$) in Figs.III.6 and III.7c whereas they approach the value $\Delta_{Al}(T = 1°K) \simeq 0.13$ meV in Fig.III. 7a, b, and d.

Next it is useful to consider the conditions under which the double peak in the density of states may be experimentally observed.We may deduce from Figs.III.6a and III.7a that two separated peaks exist for $\Gamma_N \lesssim 1$ meV in the N-side of the proximity sandwich and for $\Gamma_S \lesssim 1$ meV in the S-side of the proximity sandwich. For higher $\Gamma$'s the peaks merge. Lower bounds for each $\Gamma$ may be estimated from the plot of peak magnitudes in Fig.III.8. If we consider 0.01 change in the normalized density of states as the minimum resolvable change (because of large variations of the density of states in the gap region, smaller changes are difficult to observe), then we can set the following limits,

$$0.005 \text{ meV} \lesssim \Gamma_N \lesssim 1 \text{ meV}, \quad \text{N-side,}$$
$$0.001 \text{ meV} \lesssim \Gamma_S \lesssim 1 \text{ meV}, \quad \text{S-side.} \qquad \text{III.6}$$

Using eqs.III.4 and $v_{FN} = v_{FS} = 10^8$cm/sec and $B_N = B_S = 2$, we may rewrite eq.III.6 in the form

FIG. III.8

The magnitude of the induced peak at 1°K according to the McMillan model. The left hand side refers to peak P2 created in aluminum by the presence of tin and the right hand side refers to peak P1 created in tin by the presence of aluminum. The magnitude of the peaks means the distance from the dip between the two peaks to the corresponding peak maximum, as shown in the inserts.

Note that the tin peak induced in aluminum is already very small for $\Gamma_S/\Gamma_N \simeq 1$, while the aluminum peak induced in tin is reasonably large for all ratios of $\Gamma_S/\Gamma_N$.

The scatter is caused by calculation of the density of states at discrete energy points only. The meaning of the symbols is the same as in Figs. III.6 and III.7.

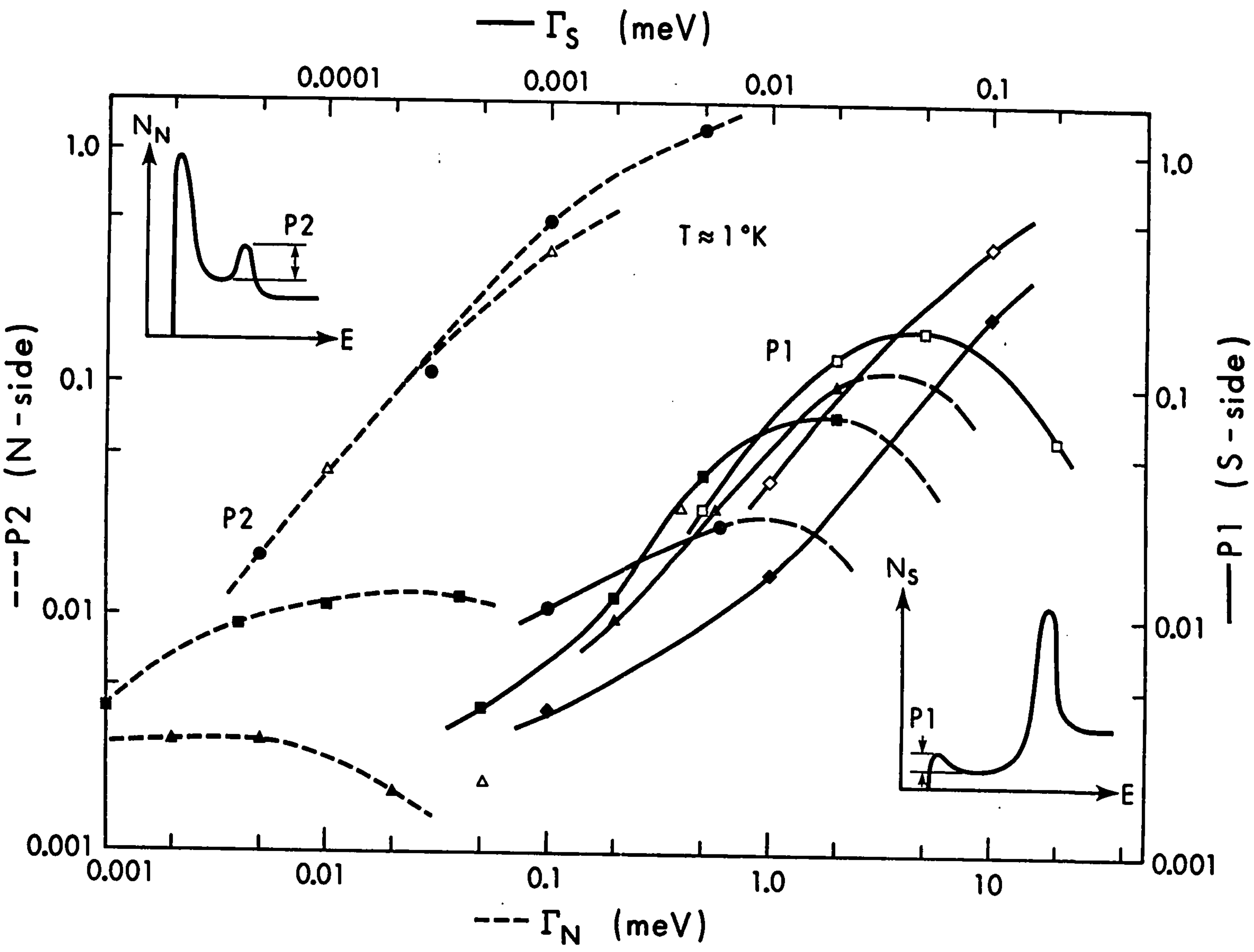
— Γ_S (meV)
0.0001
0.001
0.01
0.1
---P2 (N-side)
1.0
0.1
0.01
0.001
—P1 (S-side)
1.0
0.1
0.01
0.001
0.001
0.01
0.1
1.0
10
--- Γ_N (meV)
N_N
P2
E
T ≈ 1 °K
P1
P2
N_S
P1
E

$$6 \times 10^{-6} \lesssim \frac{\alpha}{d_N} \lesssim 10^{-3}, \qquad \text{N-side,}$$

$$1 \times 10^{-6} \lesssim \frac{\alpha}{d_S} \lesssim 10^{-3}, \qquad \text{S-side,} \qquad \text{III.7}$$

where $d_N$ or $d_S$ are expressed in Å. If e.g. $d_N \simeq 100$ Å, then we should be able to observe the double peaked structure in the N-side for $\alpha$ in the range $6 \times 10^{-4} \lesssim \alpha \lesssim 0.1$, which agrees reasonably with our experimental observations.

# CHAPTER IV

# EXPERIMENTAL PROCEDURE

## IV.1. Sample Preparation

All tunnel junctions were prepared on Fisher brand 12 - 550 glass microscope slides, which were found to have very smooth surfaces. The slides were washed with detergent and then slightly flame polished. Contacts were soldered to the glass slides with indium and coated with gold prior to the actual junction preparation. Some of the slides were also precoated with SiO (Strongin at al (1970)) in order to obtain continuous metallic films at smaller thicknesses. The effect of SiO precoating is discussed later. The films of metals were evaporated from a distance of about 50 cm through wedge shaped masks which were pressed against the substrate. It was found, using the Tolansky interferometer, that wedge shaped masks produced films with more rectangular cross-section than "chimney" shaped masks. The width of the films was ≃ 0.8 mm. Aluminum was evaporated from a helix or basket made from stranded tungsten wire; tin was evaporated from a tantalum boat. The evaporation rate for tin was from 50 to 100 Å/sec,for aluminum from 5 to 10 Å/sec.

The vacuum system consisted of a 6 inch oil diffusion pump with a liquid nitrogen cold trap backed by a mechanical pump. During evaporation liquid nitrogen was also passed through a coil in the evaporation space. The vacuum was about 1 x $10^{-7}$ Torr before evaporations were started and usually did not exceed $10^{-6}$ Torr during the evaporation.

### IV.2 Oxidation (the Formation of a Tunneling Barrier)

The standard procedure during the tunnel junction preparation was as follows. The base layer of aluminum was evaporated onto the glass substrate and oxidized to form a tunnel barrier; then cross strips of another metal were evaporated over the oxidized aluminum to form tunnel junctions.

To oxidize the aluminum base layer we chose a glow discharge oxidation method. A quantitative discussion of glow discharge oxidation of evaporated aluminum films for a particular geometry of glow electrode is presented in Appendix III. For different geometries of the glow electrode the oxidation rates were different, but the oxidation laws were the same. In most cases the glow electrode was a ring of aluminum wire 2 inches in diameter, located about 3 inches from the substrate. The aluminum strip was oxidized for about 350 sec in an atmosphere of dry oxygen at a pressure of $\simeq 0.15$ Torr. The electrode was maintained at a negative potential of about 350 V and the glow current was one mA. This oxidation procedure produced a junction resistance about $100\Omega$ for an Al-$Al_2O_3$-Al junction if the aluminum of the proximity sandwich was evaporated within a few minutes after the oxidation and was at least 100 Å thick. Thinner layers required less oxidation time to produce the same resistance whereas a delay of about 2 hours before evaporating the aluminum cover layer necessitated twice the oxidation time. If tin was evaporated onto the aluminum oxide, the reduction of the oxidation time was found to agree with Handy's (1962) measurements.

The actual oxidation time depended on such factors as the evaporation rate of the aluminum, vacuum during the evaporation, aluminum thickness, the kind of substrate (glass or SiO) and temperature. The exact relationships between these effects and the oxidation time necessary to produce a good junction were not studied but an attempt was made to keep them the same for every junction prepared. Then the oxidation by glow discharge was very reproducible and the junction resistivity could be predicted with about 20% accuracy.

The usual method for estimating the oxide thickness during the oxidation is to measure the oxidation time and to use the assumption that the resistivity increases linearly with time (Appendix III.). The measurement of the resistance change of the aluminum film which is being oxidized would provide an alternate method for determinating the oxidation progress. Assume that a slab of material has before oxidation a thickness d and resistance R (see Fig.IV.1a). During oxidation a thickness

FIG. IV.1

The relative change of the resistance of an aluminum film during the glow discharge oxidation as a function of thickness.

(a) Configuration of the metal film and oxide used to estimate the resistance change during oxidation.

(b) ○ experimental $\frac{\Delta R}{R}$ vs d,

------- plot of eq. IV.1 for $\delta = 3$ Å ,

-·-·-·- plot of eq. IV.1 for $\delta = 6$ Å.

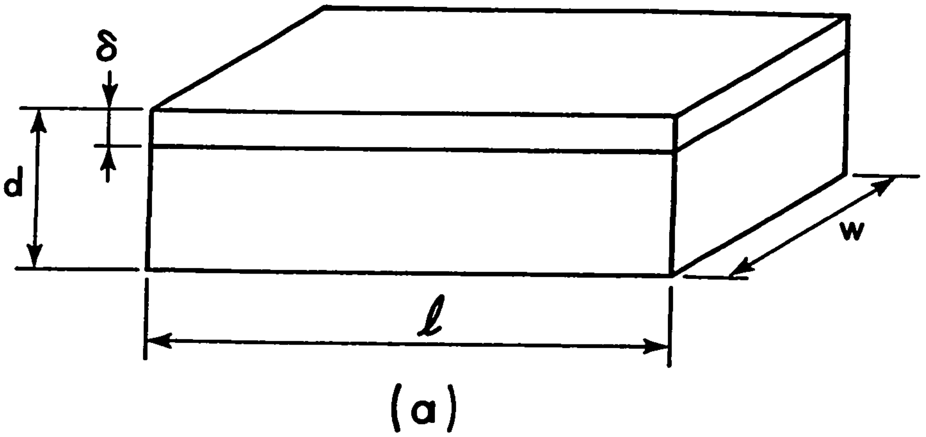
δ
d
w
ℓ
(a)

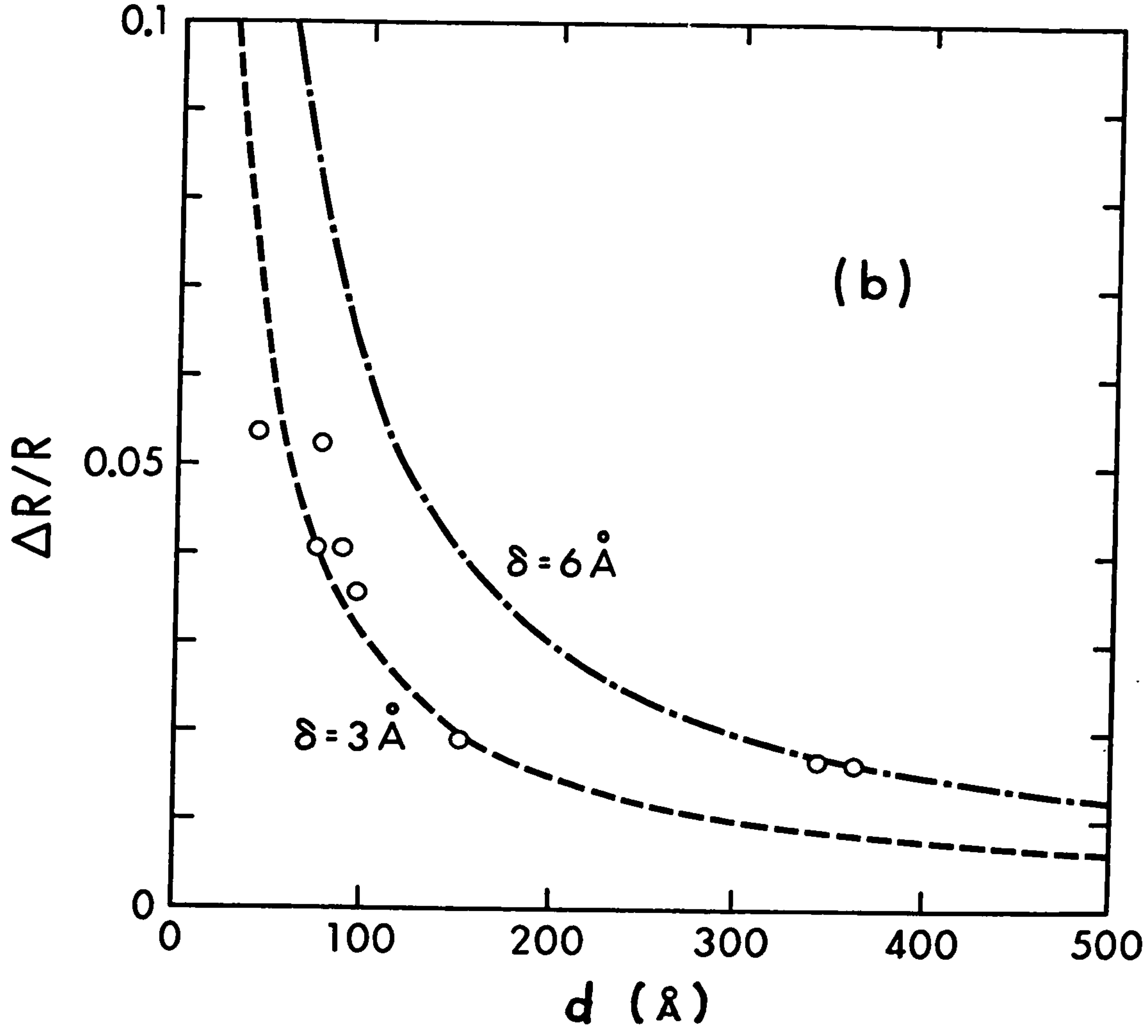
0.1
0.05
0
ΔR/R
0
100
200
300
400
500
d (Å)
(b)
δ = 6 Å
δ = 3 Å

$\delta$ of aluminum metal is used to build the oxide and the resistance increases by $\Delta R$. Then, assuming, that the electron scattering at the oxidized surface is unchanged by the oxidation, we may write

$$\frac{\Delta R/R}{1+\Delta R/R} = \frac{\delta}{d} \quad \text{or} \quad \frac{\Delta R}{R} = \frac{\delta}{d}\,, \qquad \text{IV.1}$$

if $\Delta R/R \ll 1$ (which is usually the case). A plot of eq.IV.1 for $\delta = 3$ Å and $\delta = 6$ Å is compared with experiment in Fig. IV.1b. For thicknesses below 200 Å the oxidized thickness of aluminum is $\delta \simeq 3$ Å, for higher thicknesses $\delta \simeq 6$ Å. On the average 4 to 5 Å of aluminum metal are used for oxidation. The scatter in the experimental results may be caused by many effects - e.g. change of strain in the film, annealing during the oxidation, or change in the kind of electron scattering at the surface as it is oxidized. When 5 Å of aluminum is completely oxidized, then using the oxide density $\rho_{ox} = 3.17\ g/cm^3$ (Dignam et al (1966)) and assuming perfect $Al_2O_3$, one obtains $\sim$9 Å for the oxide thickness. A direct measurement of the mass gain of oxygen during the oxidation (see Appendix III) gives $\sim$27 Å for the oxide thickness (again assuming perfect $Al_2O_3$ and $\rho_{ox} = 3.17\ g/cm^3$). The difference indicates that the composition of oxide is not $Al_2O_3$. If we assume that 5 Å of aluminum metal ($0.135\ \mu g/cm^2$) is combined with $0.4\ \mu g/cm^2$ of oxygen to form an oxide (corresponding to 27 Å of oxide with density $3.17\ g/cm^3$), then instead of having stoichiometric composition $Al_2O_3$ we shall get composition $Al_2O_8$ or $Al_2O_9$. One has to remember inaccuracies of the methods; e.g., annealing during the oxidation should decrease the resistance of the aluminum film, therefore the resulting resistance change is smaller than without annealing and the calculated content of oxygen is greater.

## IV.3 Thickness Measurements

### IV.3.a The Tolansky interferometer

The basic tool for the measurement of the thickness of thin films is the Tolansky multiple beam interferometer, described by Tolansky (1948), Tolansky (1960) and Heavens (1951). When the thin wedge of air formed by two reflecting mirrors (one of them partially transparent) is placed in the path of a light beam, the interference fringes arising from path differences between the light reflected at the two surfaces can be observed. A narrow thin film evaporated onto the surface of the opaque mirror produces a shift of the position of the fringes as shown in Fig.IV.2. The height of the step $\Delta$ produced on each fringe at the edge of the thin film is related to its thickness d by the following expression:

$$d = \frac{\lambda}{2}\frac{\Delta}{\ell}, \qquad \text{IV.2}$$

where $\ell$ is the separation of the fringes and $\lambda$ is the wavelength of the light. The actual experimental procedure is as

FIG. IV.2

Illustration of the thickness measurement .

(a) Cross-section through the interference element ,

(b) The resulting fringe pattern .

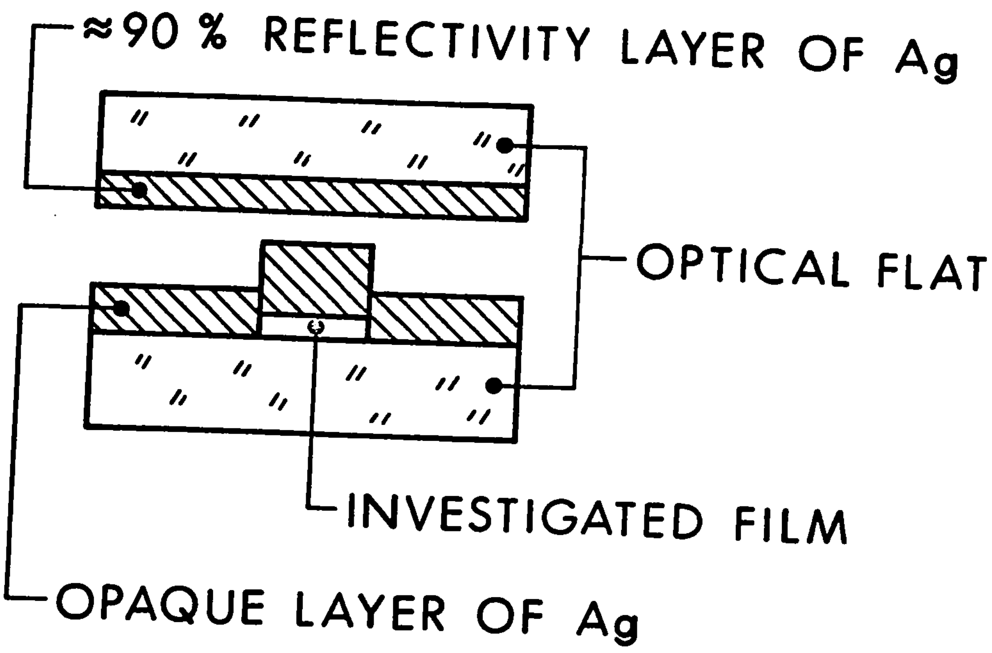
≈90 % REFLECTIVITY LAYER OF Ag
OPTICAL FLAT
INVESTIGATED FILM
OPAQUE LAYER OF Ag

(a)

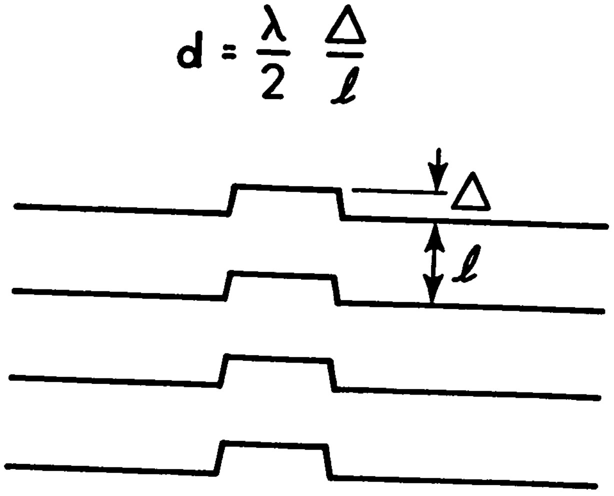

$$d = \frac{\lambda}{2} \frac{\Delta}{\ell}$$

(b)

follows. Two optical flats are cleaned by washing in $H_2O_2$ and then exposing them to a glow discharge.The film whose thickness is to be measured is evaporated onto the surface of one optical flat and is subsequently coated by an opaque layer of evaporated silver. Another optical flat is coated with a layer of silver with about 94% reflectivity (resulting in about 60 or more beam interferences). The optical flats are placed together to produce a thin wedge of air as shown in Fig.IV.2.a.

Fig.IV.3 is a diagram of our interferometer. The light from the mercury lamp is passed through a green filter and condensed onto an aperture of ∿ 1 mm diameter. A parallel beam of light is formed by a lens with a focal length of 10 cm. The light then passes through a half-transparent mirror, interferes in the thin wedge of air and is reflected into the lens system and camera. Manipulation of the thin wedge of air is facilitated by the holder described by Heavens (1950). Photographs of the fringes are evaluated by the method described in Appendix IV.

### IV.3.b The Quartz crystal thickness monitor

The thickness of the evaporated films was monitored during the evaporation by the quartz crystal monitor. Two 5 MHz crystals were mounted in the same water-cooled holder. One crystal was exposed directly to the evaporating material, the other was simply in thermal contact with copper holder (see Fig.IV.4), resulting in at least partial

FIG. IV.3

Schematic diagram of Tolansky interferometer .

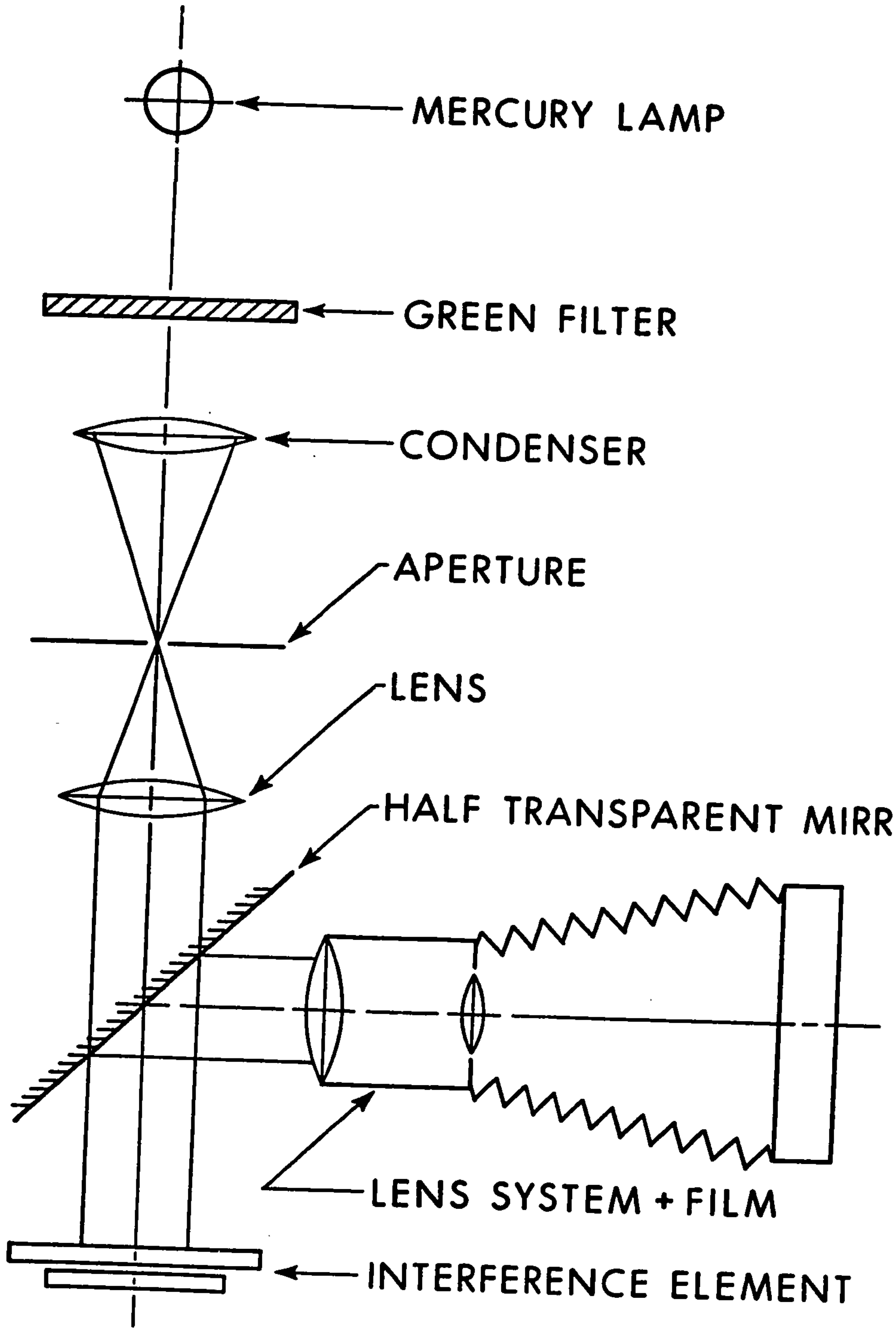
MERCURY LAMP
GREEN FILTER
CONDENSER
APERTURE
LENS
HALF TRANSPARENT MIRROR
LENS SYSTEM + FILM
INTERFERENCE ELEMENT

FIG. IV.4

Quartz crystal holder. The springs used are as weak as possible.

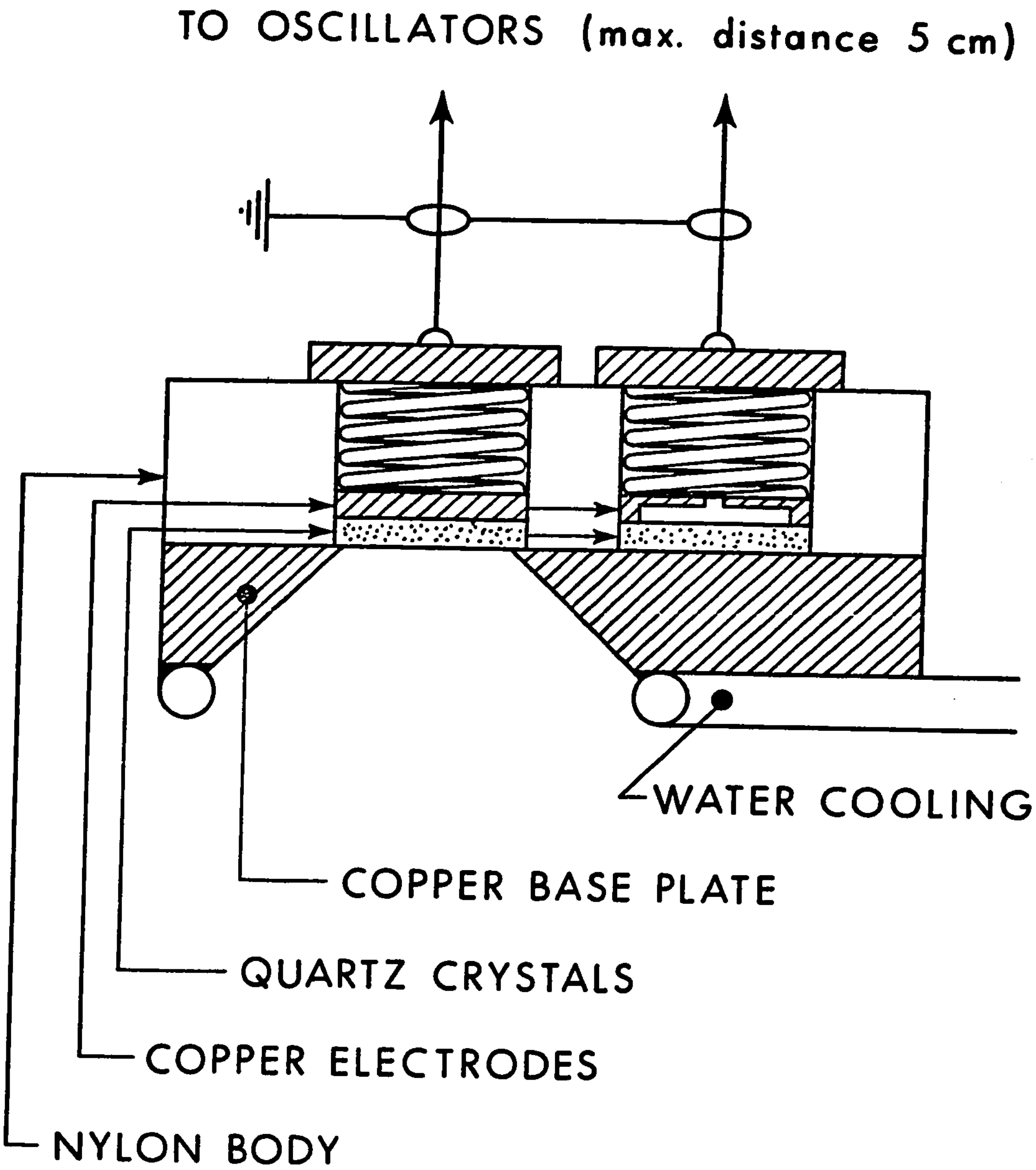TO OSCILLATORS (max. distance 5 cm)
WATER COOLING
COPPER BASE PLATE
QUARTZ CRYSTALS
COPPER ELECTRODES
NYLON BODY

compensation for the heat shock during evaporation. The heat shock produced a slow drift of the frequency toward a steady value, after the evaporation was completed. The magnitude of the drift was proportional to the evaporation rate and to the amount of evaporated material, factors that are connected with the amount of heat supplied, and was zero when very thin films were evaporated. With the two crystal arrangement the frequency drift was usually about 1% of the total frequency change.

The circuit diagram of the quartz crystal monitor is shown in Appendix V.

The crystal thickness monitor was placed about 32 cm above the evaporation sources, while the sample was placed about 50 cm above the sources. Taking into account the geometry following Holland (1963), the sensitivity of the crystal monitor, as calibrated by the Tolansky interferometer was

$$\frac{d_{\text{sample}}}{\Delta f} = 0.366 \text{ Å/Hz} \quad \text{for Al},$$

$$\frac{d_{\text{sample}}}{\Delta f} = 0.115 \text{ Å/Hz} \quad \text{for Sn},$$

where $d_{\text{sample}}$ is the thickness of the film at the sample position and $\Delta f$ is the frequency change of the quartz crystal monitor. When the ratio of frequency change per Å for Al and Sn was compared with the ratio of the densities $\rho_{\text{Al}}$ and $\rho_{\text{Sn}}$ of Al and Sn it is found that

$$\left(\frac{\Delta f_{Al}}{\Delta f_{Sn}}\right)_{1Å} = 0.315, \quad \frac{\rho_{Al}}{\rho_{Sn}} = 0.370.$$

The difference between these values may be caused by a different porosity of the evaporated films or by a different sticking probability for impinging metal atoms on the optical flat or quartz crystal surface.

People usually use silver- or gold-coated crystals (e.g. Riegert (1968)). However, we have only used crystals coated with silver because their frequency stability was superior to those coated with gold.

The crystals usually stopped oscillating after they were loaded with mass equivalent to about $10^5$Hz.

## IV.4 Description of the Apparatus and the Production of Low Temperatures

The tunnel junctions were prepared in the metal evaporator - cryostat apparatus and cooled down without breaking the vacuum. This was necessary because the transfer of a junction into a cryostat through the air always destroyed them when very thin metal films were involved. Also when proximity sandwiches were involved, reproducible results could not be obtained if they were exposed to air. Probably the interface between the metals in proximity was influenced by the air.

Fig.IV.5 is a schematic diagram of the apparatus. The cryogenic part was manufactured by Sulfrian Cryogenics,

FIG. IV.5

Schematic diagram of the evaporator-cryostat.

A - port for liquid He input into the He pot
B - outlet for the measurement of He vapor pressure in the He pot
C - connection to the pump
D - port for liquid He input into the main He vessel
E - liquid helium level detector
F - radiation baffle
G - carbon resistor for liquid helium level sensing
H - guide tube for steel piano wire
I - pulleys for mask operation and pressing system
J - ports for wires
K - germanium thermometer
L - sample
M - spring-loaded balls for easy location of mask position
N - movable mask
O - pressing mechanismus
P - movable shutter on LN temperature shield
Q - window for observation of glow discharge electrode
R - glow discharge electrode
S - liquid nitrogen coiled tube
T - optical flat for calibration of quartz crystal thickness monitor
U - quartz crystal thickness monitor

V - window with mirror for observation of evaporation sources

W - high vacuum pump

Y - shutter

Z - multi-filament carousel

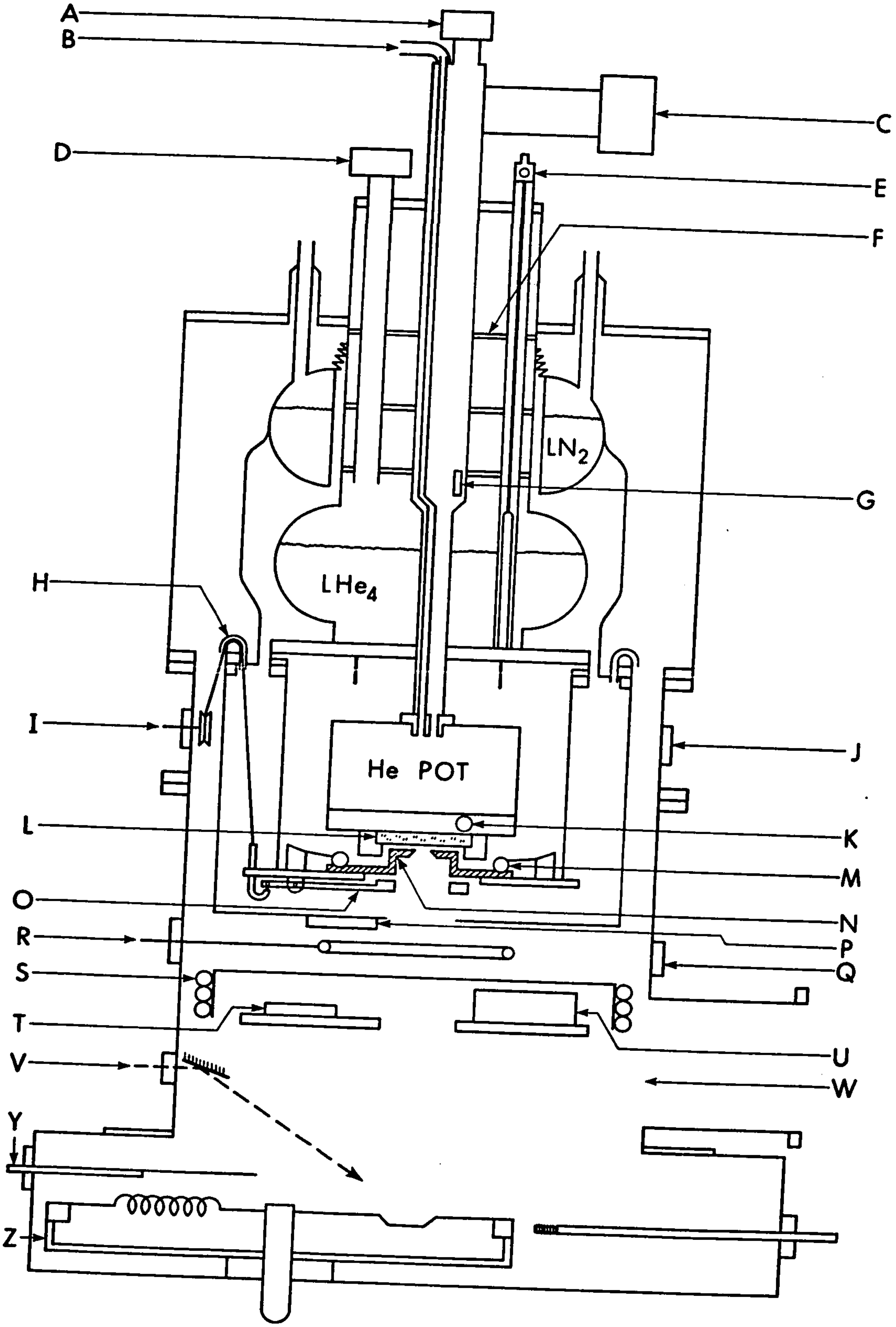
A
B
C
D
E
F
LN$_2$
G
LHe$_4$
H
I
J
He POT
L
K
M
O
N
R
P
S
Q
T
U
V
W
Y
Z

Inc. The liquid level was detected by a capacitance level detector (see Appendix VI), which was immersed in either liquid nitrogen or liquid helium. The 200 $cm^3$ $He_4$ pot was attached to the cryogenic part by a single stainless steel tube. The helium and nitrogen temperature shields were connected to the corresponding baths by a greased metal flange. Shutters that could be operated from outside the apparatus normally covered the apertures through which the evaporating metal reached the glass substrate. The substrate was clamped to the bottom of the helium pot and Apiezon N grease served as a thermal contact. The mask and the mechanisms which could press the mask against the substrate were operated from the outside by steel piano wire (0.010 inch diameter). The glow discharge electrode was placed outside the nitrogen temperature shield. Boats or filaments were mounted in the circular carrousel, which permitted succesive evaporation from six independent sources. One of the sources was equipped with a feeding mechanism so that additional metal could be added to the source during evaporation of thick films. A window with a mirror was provided for observation of the evaporation sources. A typical run is described in Appendix VII.

Temperatures in the range between 1.3°K and 4.2°K were measured by a germanium resistor placed on the bottom of the pumping pot. The resistor was calibrated against vapor pressure measurements and the experimental points were fitted by a computer to the formula (shown e.g. by Blakemore et al (1970))

$$R = A\ T^{-B}\ e^{C/T}\ ,$$

where A, B, and C are constants. A table of R vs T was compiled in 10 m°K steps, which is the limit of resolution of our data collected over about four months of experiments. In the range between 1.05°K (lowest attainable temperature in our system) and 1.3°K the vapor pressure was compared with the 1958 $He_4$ Scale of temperatures compiled by Dijk et al (1960). The agreement of the sample temperature with the temperature reading was checked at 3.8°K (the critical temperature of tin) and by comparison of tunneling measurements with the BCS variation of tunneling conductance.

The cryostat was wired with No.40 B&S gauge copper wires which were thermally anchored at liquid nitrogen temperature, liquid helium temperature and on the $He_4$ pot before they were connected to the sample.

The conductivity measurements were done on a tunneling conductance bridge similar to the one described by Rogers (1970).

# CHAPTER V

## DISCUSSION OF MATERIALS USED

### V.1 The Selection of Materials

We have selected aluminum for the base layer because it is easily oxidized to form a tunneling barrier and also its critical temperature (1.2°K for bulk material and higher for thin films) is convenient; experiments can be done readily with the base layer either normal or superconducting.

Aluminum and tin have been selected for the proximity sandwich. Again aluminum was selected because of its critical temperature and ease of oxidation which is important in the control of the transmission probability, $\alpha$ . Tin was selected because it becomes superconducting below 3.8°K, and within our range of measurement we could then have neither, only one, or both metals of the proximity sandwich in its superconducting state.

### V.2 The Problem of Interdiffusion

As suggested first by Rose-Innes and Serin (1961) interdiffusion may often occur in proximity sandwiches. However according to Hansen (1958), and Elliott (1965) the solid solubilities for the aluminum - tin system are very restricted and no intermetallic compounds are known. Also in the experiments reported here a thin oxide layer was formed between the aluminum and tin which would further reduce diffusion effect. Perhaps the strongest evidence that our procedures produced proximity structures with distinct aluminum and tin films lies in the tunneling results, which exhibit several characteristics that would not arise in badly interdiffused or alloyed structure. An alloy, as pointed out by Guyon et al (1966), should behave like a BCS superconductor.

### V.3 Mean Free Path Considerations

The important condition for the McMillan tunneling model of the proximity effect to be valid is that the electron mean free path be comparable with the thickness of the metallic films in question.The measurement of the mean free path from the residual resistivity of a very thin film is usually complicated by the presence of surface scattering. If we consider pure bulk material with its bulk mean free path $\ell_0$ and bulk resistivity $\rho_0$, then the following expression, shown e.g. by Kahan et al (1960), is valid:

$$\rho_0 \ell_0 = \frac{h}{n^{2/3} e^2} \left(\frac{3}{8\pi}\right)^{1/3} = \text{constant}, \qquad \text{V.1}$$

where n is the number of conduction electrons per cm$^3$, e is the electron charge and h is the Planck constant. If we assume that a thin layer is cut from the bulk piece of material, without otherwise changing the structure, then the specific resistivity of the thin layer will be larger than the bulk value due to the additional scattering at the surface. The resistivity increase as a function of thickness was first calculated by Fuchs (1938) and recalculated by Sondheimer (1952). The experimental results of, e.g. Andrew (1949) on very pure rolled thin tin foils and on mercury wires agreed quite well with the predictions of the theory. A pure material has very long mean free path and therefore relatively thick foil - which has the structure of bulk material - is already affected by the surface scattering. However the experiments of Hilsch (1962) and of Basewitz and Minnigerode (1964) on thin evaporated films cannot be fitted to the Sondheimer calculations. The resistivity increases more rapidly with decreasing thickness than predicted by the calculation. We believe that in thin films the bulk structure is not preserved and as the film is made thinner more defects are introduced. Assume for a moment, that we have bulk material with the same structure as a thin film. Then its mean free path is $\ell_B$ and bulk resistivity is $\rho_B$. Further we assume, that eq.V.1 is still valid for the material with the thin film structure and that (as suggested by Mayadas and Shatzkes (1970))

$$\rho_0\ell_0 = \rho_B\ell_B . \qquad \text{V.2}$$

The specific resistivity of our thin film is not $\rho_B$ but $\rho$ (because of additional surface scattering) and we assume that $\rho$ is connected with $\rho_B$ by Sondheimer's calculation with the mean free path $\ell_B$.

Therefore to find the mean free path $\ell_B$ of a thin film from its thickness d and residual resistivity $\rho$ we proceed as follows. The constant in equation V.1 is found for a given material (see e.g. Bassewitz and Minnigerode (1964) who list $\rho_0\ell_0$ for various metals) and the Sondheimer dependences of $\rho$ vs d are calculated for different pairs of $\rho_B$ and $\ell_B$ (which are in accord with eq.V.2). The family of calculated $\rho$ vs d curves with $\ell_B$ as a parameter is plotted together with experimental points of $\rho$ vs d (see Fig.V.1) and the corresponding mean free path is determined as a function of thickness d. For faster data processing we have written a computer program, which for given values of $\rho$, d, and the constant in eq.V.1, finds the corresponding mean free path. All calculations have been done for diffuse scattering at the film surfaces.

In Fig.V.2 the mean free paths for thin aluminum films evaporated at room temperature onto glass substrates and glass substrates coated by 500 Å of SiO are presented. The value $\rho_0\ell_0 = 4.9 \times 10^{-12}\ \Omega\ \text{cm}^2$ was used and the 5 Å correction was applied to the thickness due to the oxidation of the surface (see Chapter IV.2). It is very interesting to note that aluminum films evaporated onto an SiO surface possess a shorter mean free path than the films evaporated onto a glass surface. The glass substrate is usually precoated with SiO in order to "improve" the quality of

FIG. V.1

Residual resistivity as a function of thickness for various values of mean free path.

— calculation for Al, $\rho_B \ell_B = 4.9 \times 10^{-12}\ \Omega\mathrm{cm}^2$,

○ experimental data, aluminum films evaporated onto glass substrate ,

△ experimental data, aluminum films evaporated onto glass substrate coated by $\sim$ 500 Å of SiO.

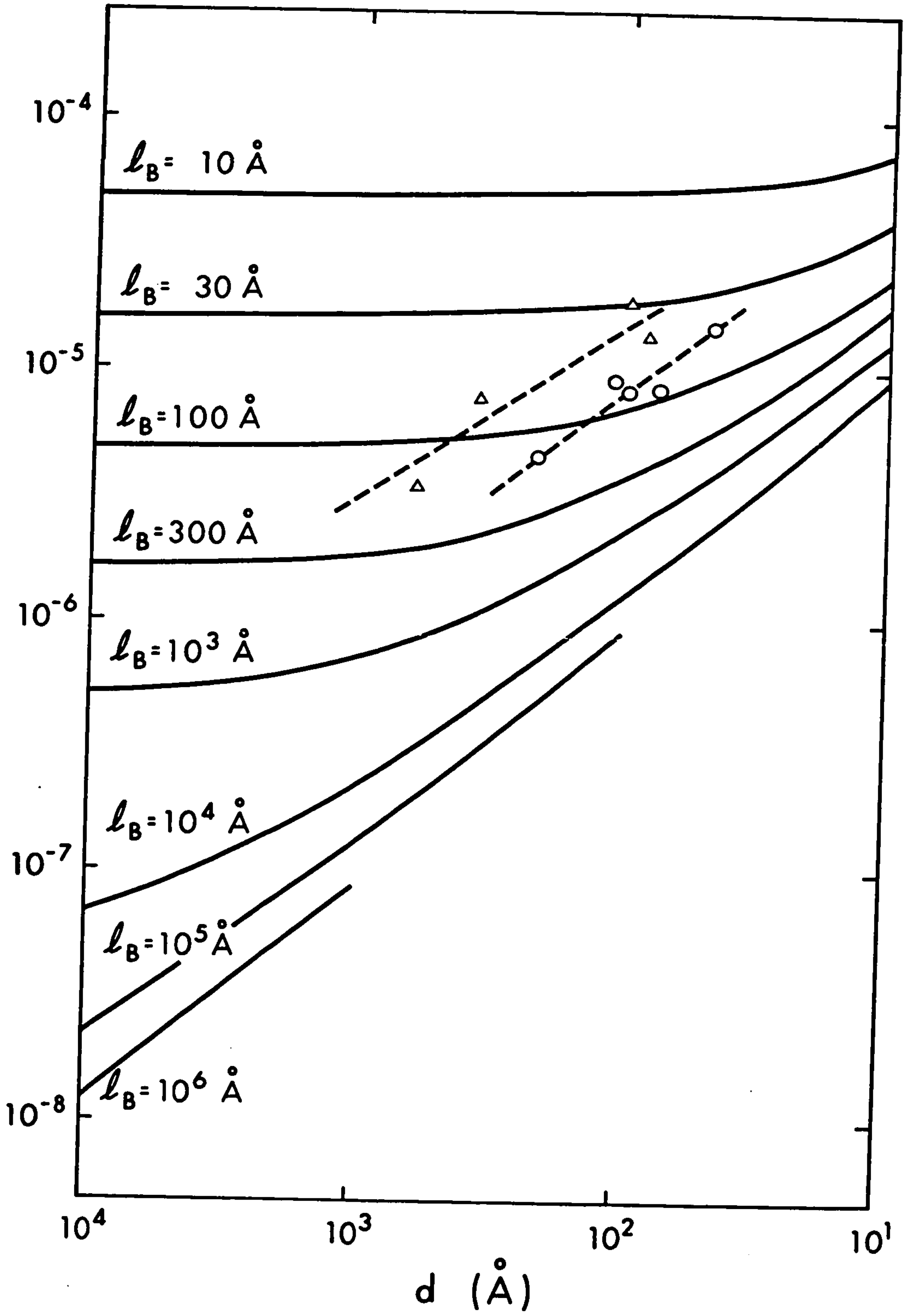
$10^{-4}$
$10^{-5}$
$10^{-6}$
$10^{-7}$
$10^{-8}$
$\rho$ ($\Omega$ cm)
$\ell_B$ = 10 Å
$\ell_B$ = 30 Å
$\ell_B$ = 100 Å
$\ell_B$ = 300 Å
$\ell_B$ = $10^3$ Å
$\ell_B$ = $10^4$ Å
$\ell_B$ = $10^5$ Å
$\ell_B$ = $10^6$ Å
$10^4$
$10^3$
$10^2$
$10^1$
d (Å)

FIG. V.2

The mean free path of evaporated aluminum films as a function of thickness ( evaporation done at room temperature ). The value $\rho_B \ell_B = 4.9 \times 10^{-12} \Omega cm^2$ and 5 Å thickness correction ( due to oxidation ) was used.

○ glass substrate,

△ glass substrate precoated with 500 Å of SiO.

When the value $\rho_B \ell_B = 8.2 \times 10^{-12} \Omega cm^2$ is used the trend of $\ell_B$ vs d is shown by

----- for glass substrate, and by

-·-·- for glass substrate coated with 500 Å of SiO.

Solid lines represent visual fit to the experimental points.

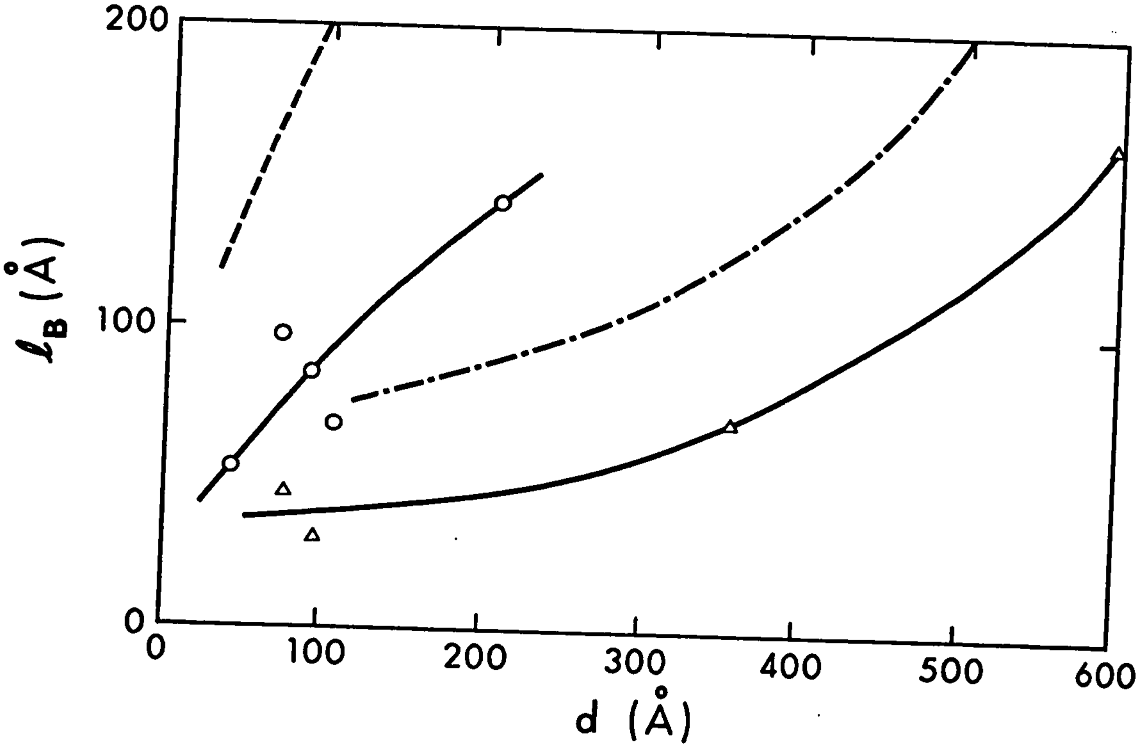

200
100
0
$\ell_B$ (Å)
0
100
200
300
400
500
600
d (Å)

the films and to make them continuous at smaller thicknesses (Strongin et al (1970)). We have actually observed that films evaporated onto the SiO surface become continuous sooner. The effect is probably connected with the formation of droplets of evaporated material the size of which depends on the substrate. Small droplets with short mean free paths are probably interconnected sooner than bigger droplets with longer mean free path. Slight oxidation probably maintains the partial separation of drops and short mean free path even when the film is thick.

The mean free path for tin films evaporated onto a glass substrate is listed in Table I. The value $\rho_0 \ell_0 = 10.5 \times 10^{-12}\ \Omega\text{cm}^2$ was used. Note, that the ratio $\ell_B/d$ is generally greater for tin than for aluminum.

The scatter in the data is probably connected with the fact that all evaporations were done at room temperature which results in uncontrolled annealing.Also the aluminum films were oxidized in a glow discharge (in order to produce the tunnel junction) which might change the surface scattering and therefore the residual resistivity.

The mean free path fulfils the McMillan assumption $\ell_B \gtrsim d$ even if it is calculated by using the smallest values of $\rho_0 \ell_0$ found in the literature. If e.g. the mean free path of aluminum is estimated using the value $\rho_0 \ell_0 = 8.2 \times 10^{-12}\ \Omega\,\text{cm}^2$ obtained by Holwech and Jeppesen (1967) it would be at least twice as big as the mean free path which we obtained using the Chambers' (1950) value $\rho_0 \ell_0 = 4.9 \times 10^{-12}\ \Omega\text{cm}^2$.

# TABLE I

The mean free path of evaporated tin films as a function of thickness.

| $d$ (Å) | $\ell_B$ (Å) | $\ell_B/d$ |
|---|---|---|
| 264 | 2156 | 8.2 |
| 345 | 2382 | 6.9 |
| 376 | 3345 | 8.9 |
| 960 | 1570 | 1.7 |

# CHAPTER VI

## TUNNELING INTO A PROXIMITY SANDWICH

### VI.1 The Tunneling Integral

The normalized differential conductance $\sigma(V)$ of a tunnel junction formed between two metals A and B can be expressed in terms of their normalized densities of electronic states $N_A$ and $N_B$ (assuming constant tunneling matrix elements) by the expression

$$\sigma(V) = \frac{(dI/dV)_S}{(dI/dV)_N} = \int_{-\infty}^{+\infty} N_A(E)\left[\frac{\partial N_B(E-V)}{\partial V}\,\phi(E,V) + N_B(E-V)\frac{\partial\phi(E,V)}{\partial V}\right]dE, \qquad \text{VI.1}$$

where E is energy, V is the applied voltage in energy units, and $\phi(E,V) = [1+\exp(E-V)/kT]^{-1} - [1+\exp E/kT]^{-1}$.

In order to carry out numerical calculations the functions $N_A$, $N_B$, and the derivative $\partial N_B/\partial V$ must be finite. We have used the approximation

$$N_B = 1 \qquad \text{if B is a normal metal,}$$

$$N_B = \mathrm{Re}[|E|/(E^2-\Delta^2)^{1/2}] \quad \text{if B is a superconductor} \qquad \text{VI.2}$$

where $\Delta = \Delta_B(1 + i\delta)$

with $\Delta_B$ the BCS energy gap in metal B.

$N_A$ is the McMillan density of states of the proximity sandwich.

The constant $\delta$ has been evaluated by fitting eq.VI.1

to experimental tunneling data. $\delta_{Al} = 0.013$ was obtained by putting $N_A = N_B = N_{Al}$ and fitting to data for an Al-I-Al junction at T = 0.4°K, then using this value eq.VI.1 was again fitted to results for an Al-I-Sn junction at T = 1.0°K, yielding $\delta_{Sn} = 0.038$. A comparison of the calculated and experimental curves for this junction is shown in Fig.VI.1.a. The approximate density of states for a superconductor was then used in eq.VI.1 to calculate the tunnel conductance of a normal metal-superconductor junction. Comparison with Bermon's (1964) calculations for a similar junction, plotted in Fig.VI.1.b, shows that the conductance values agree within 1%. We conclude that the approximate density of states of eq.VI.2 is adequate to use in the calculation of the tunnel conductance of a junction formed between a superconductor (or a normal metal) and a proximity sandwich characterized by the McMillan density of states.

## VI.2 Tunneling into the N-side of a Proximity Sandwich

### VI.2.a Tunneling from a normal metal

A general feature of tunneling from a normal metal into the N-side of a proximity sandwich may be observed by considering the experimentally measurable quantity $[1 - \sigma(0)]$. For tunneling into a BCS superconductor $[1 - \sigma(0)] \propto 1 - T/T_C \propto \Delta^2$ whereas it increases less

FIG. VI. 1

(a) The normalized tunneling conductance $\sigma(V)$ in the junction Al-I-Sn,

——— experimental curve ,

● calculation using the smeared BCS density of states (see eq.VI.2) with $\Delta_{Al} = 0.22$ meV, $\delta_{Al} = 0.013$, $\Delta_{Sn} = 0.60$ meV, and $\delta_{Sn} = 0.036$.

(b) The deviation of Bermon's conductance $\sigma_B$ from the normalized tunneling conductance $\sigma(V)$ between a normal metal and the smeared superconducting density of states ( $\delta = 0.013$, $\Delta/kT = 2.0$).

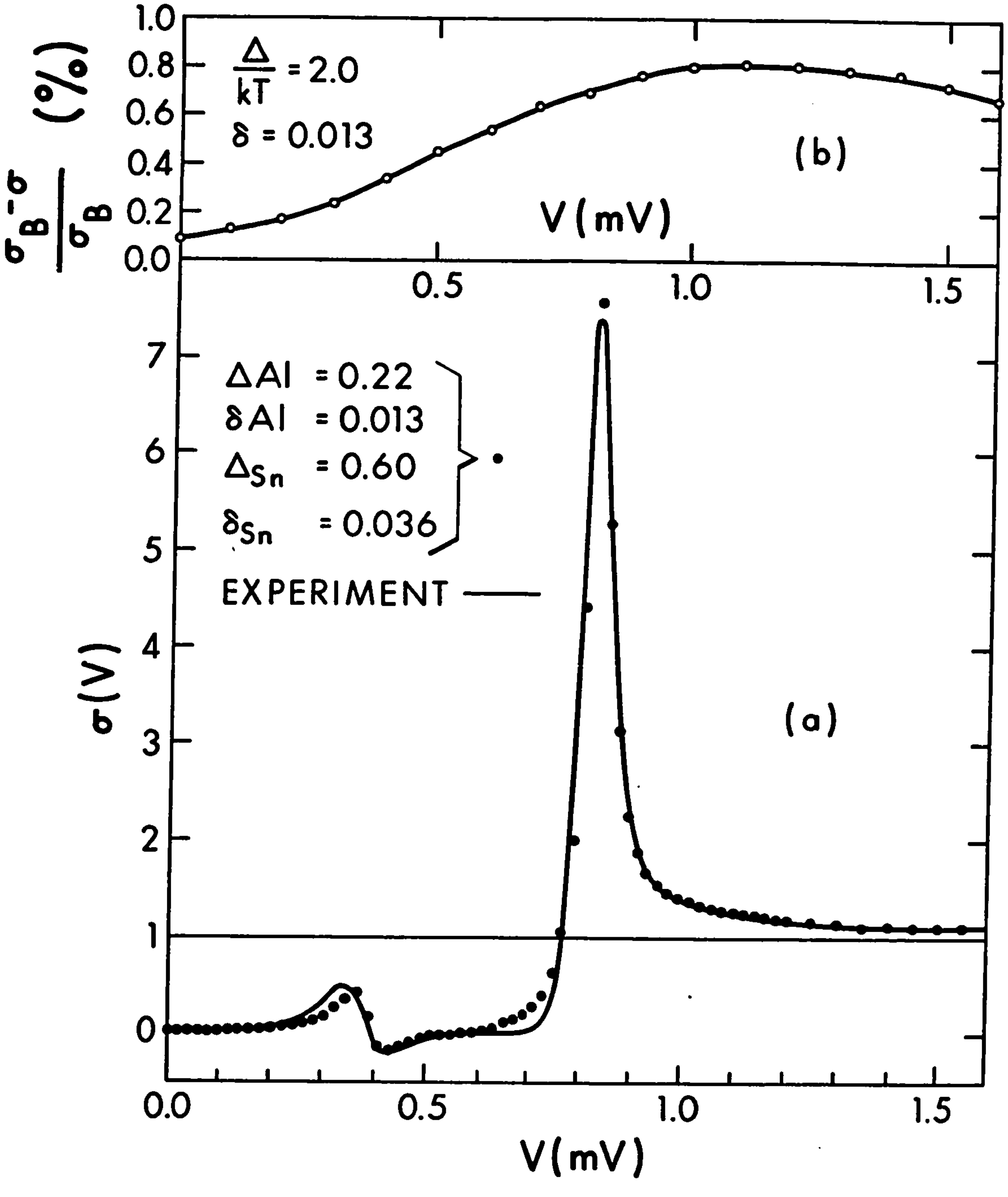

$\frac{\sigma_B - \sigma}{\sigma_B}$ (%)
$\frac{\Delta}{kT} = 2.0$
$\delta = 0.013$
(b)
V(mV)
0.0
0.2
0.4
0.6
0.8
1.0
0.5
1.0
1.5
$\Delta Al = 0.22$
$\delta Al = 0.013$
$\Delta_{Sn} = 0.60$
$\delta_{Sn} = 0.036$
EXPERIMENT
σ(V)
(a)
0
1
2
3
4
5
6
7
0.0
0.5
1.0
1.5
V(mV)

rapidly than this with decreasing temperature just below $T_C$ for tunneling into the N-side of a proximity structure and then grows faster as the temperature is lowered. Guyon et al (1966) proposed the empirical relationship $[1 - \sigma(0)] \propto (1 - T/T_C)^n$ which fits their data for proximity sandwiches made with zinc and indium-bismuth alloys. They and Claeson et al (1967) have obtained n-values between 2.3 and 3.0, but their N-films were at least 1000 Å thick and it is probable that the electron mean free path was smaller, thus violating one of the conditions of the McMillan model.

In Fig.VI.2 the behaviour of our aluminum-tin samples, in which the slopes range from about 1 to 6, is shown. Slopes of higher value are very difficult to measure because the temperature where the energy gap develops, which is used as the experimental $T_C$, cannot be measured accurately when $\sigma(0)$ is varying very slowly with temperature.

These results are in good accord with the McMillan model. For weak coupling (small $\alpha$) the magnitude of $\Delta_N^{ph}$ is very small, as may be seen in Fig.III.3, and increases slowly with decreasing temperature producing the same behavior in $[1 - \sigma(0)]$ until temperatures near the critical temperature of aluminum are reached; thereafter these quantities both rise rather sharply. For the strong coupling cases (case c, Fig.III.3) $\Delta_N^{ph}$ approaches the BCS behavior and so does the experimental slope of $[1 - \sigma(0)]$. We calculated $\sigma(0)$ as a function of temperature for different combinations of $\Gamma_N$ and $\Gamma_S$, using the relationships of the

FIG. VI.2

Experimental dependence of [1 - $\sigma(V=0)$] on ($1 - T/T_c$). $\sigma(V=0)$ is the normalized tunneling conductance at zero bias between a normal metal and the N-side of an aluminum-tin proximity structure. The appropriate experimental values of $\Gamma_N$ determined from Fig. VI.3 are : ■ $\Gamma_N$ = 1.0 meV, ▲ $\Gamma_N$ = 0.55 meV, □ $\Gamma_N$ = 0.05 meV, and ● $\Gamma_N$ = 0.02 meV.

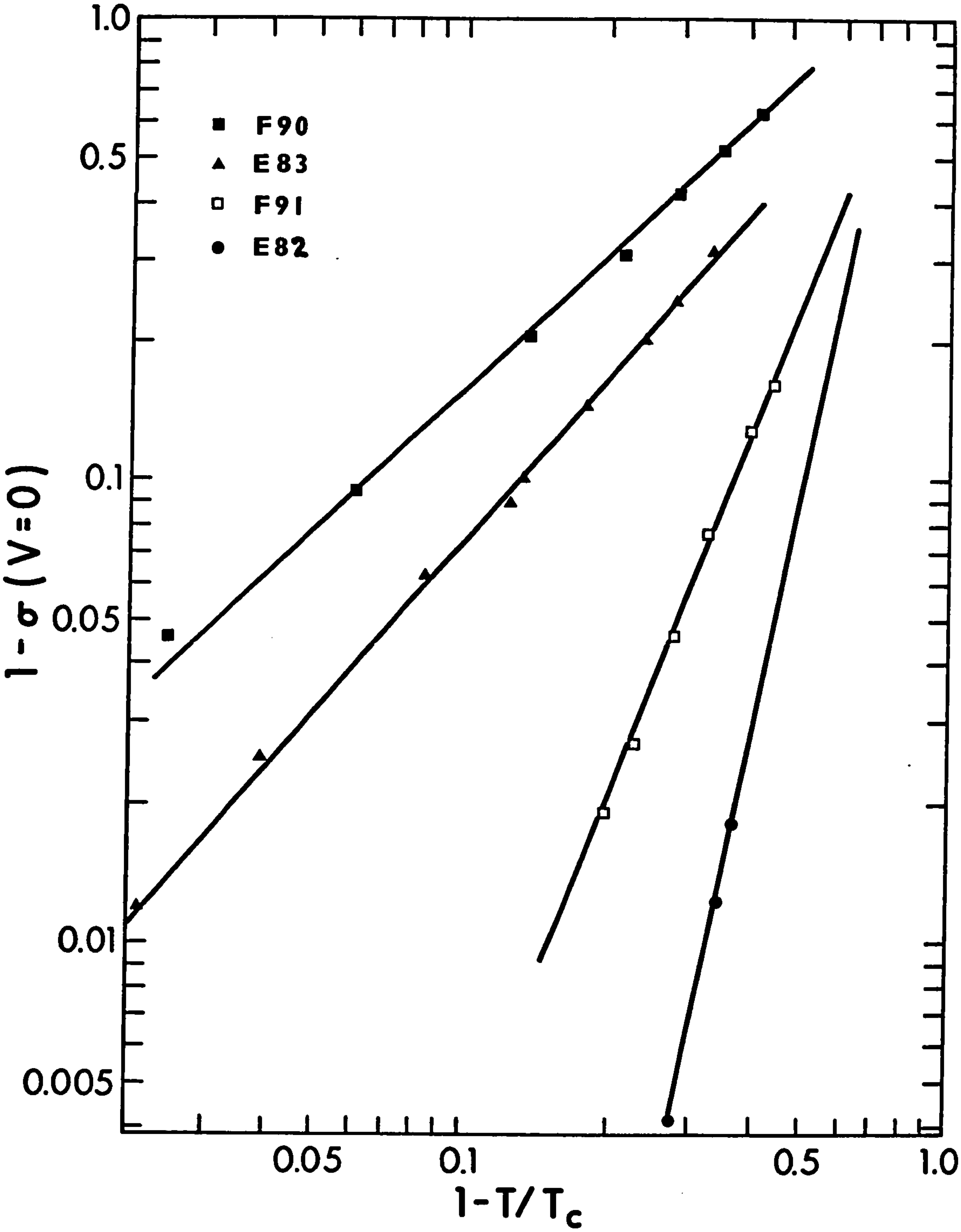
1.0
0.5
0.1
0.05
0.01
0.005
1 - σ (V=0)
■ F90
▲ E83
□ F91
● E82
0.05
0.1
0.5
1.0
1-T/T_c

McMillan model. $T_C$ was estimated using eq.III.5 and $[1 - \sigma(0)]$ vs $(1 - T/T_C)$ was plotted logarithmically as shown in Fig.VI.3. The curvature of these graphs is small and straight lines were readily fitted and their slopes, n, determined. These n-values were plotted as a function of $\Gamma_N$ for different ratios of $\Gamma_S/\Gamma_N$. Just as for the properties shown in Fig.III.6, the value of the slope is independent of $\Gamma_S$ over a wide range of $\Gamma_N$. This important result facilitates the determination of $\Gamma_N$ (or $\alpha/B_N$) for experimental samples without the necessity of knowing $\Gamma_S$ (or $B_S$). The calculations with McMillan's model for $\Gamma_N$ between 5.0 and 0.001 meV show that n may vary from 1 (strong coupling) to 25 (weak coupling ).

In Fig.VI.4 $\sigma(V)$ has been plotted as a function of applied voltage for sample D81 (with $d_N = 115$ Å, $d_S = 3150$ Å), together with the curve for tunneling into a BCS superconductor and the curve for the McMillan model, all at $T/T_C = 0.73$. It is immediately clear that the experimental results are vastly different from the BCS results and fit the McMillan model very well, particularly when the effects of a slight error in the determination of the tunnel conductance when the proximity sandwich is just above $T_C$ are considered. In order to obtain the curve for the McMillan model, the values $\Gamma_N = 0.047$ meV and $T = 2.63$°K were used, and assuming $B_N = B_S$, $v_{FN} = v_{FS}$ we obtained $\Gamma_S/\Gamma_N = 0.05$. The results are relatively insensitive to the value of $\Gamma_S/\Gamma_N$, $T_C$ is the same as that for the experimental

FIG. VI.3

Calculated values of the exponent n in the empirical expression $[1 - \sigma(V=0)] \propto (1 - T/T_c)^n$ for tunneling from a normal metal into the McMillan model for aluminum-tin using different values of $\Gamma_S/\Gamma_N$. In the insert the calculated dependence of $[1 - \sigma(V=0)]$ on $(1 - T/T_c)$ is shown.

———— McMillan model $\Gamma_N/\Gamma_S = 0.1$. (a) $\Gamma_N = 2.0$ meV, (b) $\Gamma_N = 0.5$ meV, (c) $\Gamma_N = 0.2$ meV, and (d) $\Gamma_N = 0.05$ meV.

------- BCS dependence.

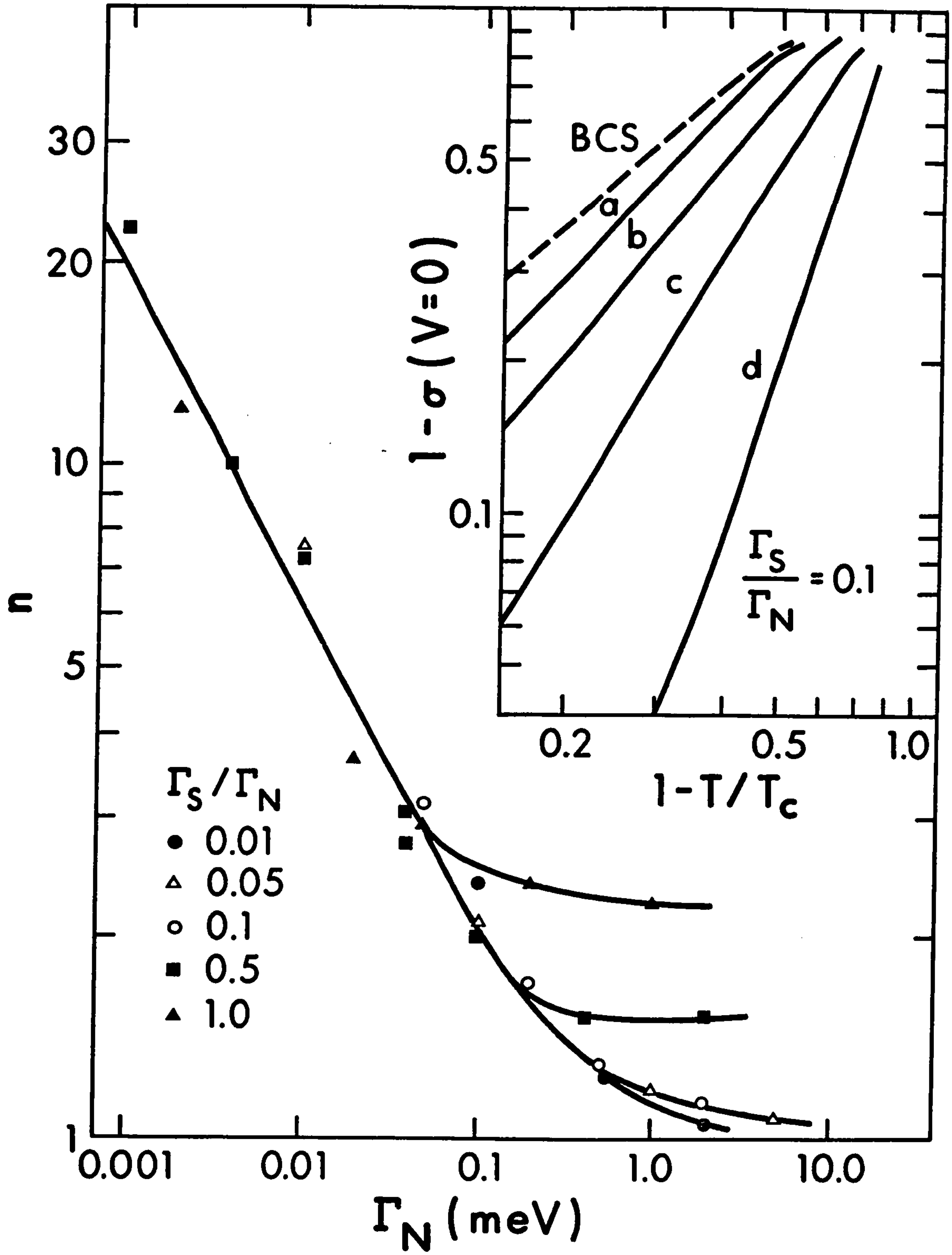

n
30
20
10
5
1
0.001
0.01
0.1
1.0
10.0
$\Gamma_N$ (meV)
$\Gamma_S/\Gamma_N$
● 0.01
△ 0.05
○ 0.1
■ 0.5
▲ 1.0
$1-\sigma(V=0)$
0.5
0.1
0.2
0.5
1.0
$1-T/T_c$
BCS
a
b
c
d
$\frac{\Gamma_S}{\Gamma_N}=0.1$

FIG. VI. 4

The normalized tunneling conductance σ(V) between a normal metal and an aluminum-tin sandwich.

○ experiment D81, $T_C$ = 3.6°K, $d_{Al}$ = 115 Å, $d_{Sn}$ = 3150 Å.

——— calculated from the McMillan model with $\Gamma_N$ = 0.047 meV, $\Gamma_S$ = 0.0024 meV, $\Delta_S^{ph}$ = 0.474 meV, and $\Delta_N^{ph}$ = 0.061 meV. T = 2.626°K and $T/T_C$ = 0.73 for both.

At zero bias only, the theoretical calculations are included for $\Gamma_S/\Gamma_N$ = 0.05 and $\Gamma_N$ = 0.04 meV ( ▲ ), $\Gamma_N$ = 0.06 meV ( □ ).

For comparison, part of the Bermon conductance $\sigma_B$ for the same $T/T_C$ is shown by dashed line. $\sigma_B(V = 0)$ = 0.514.

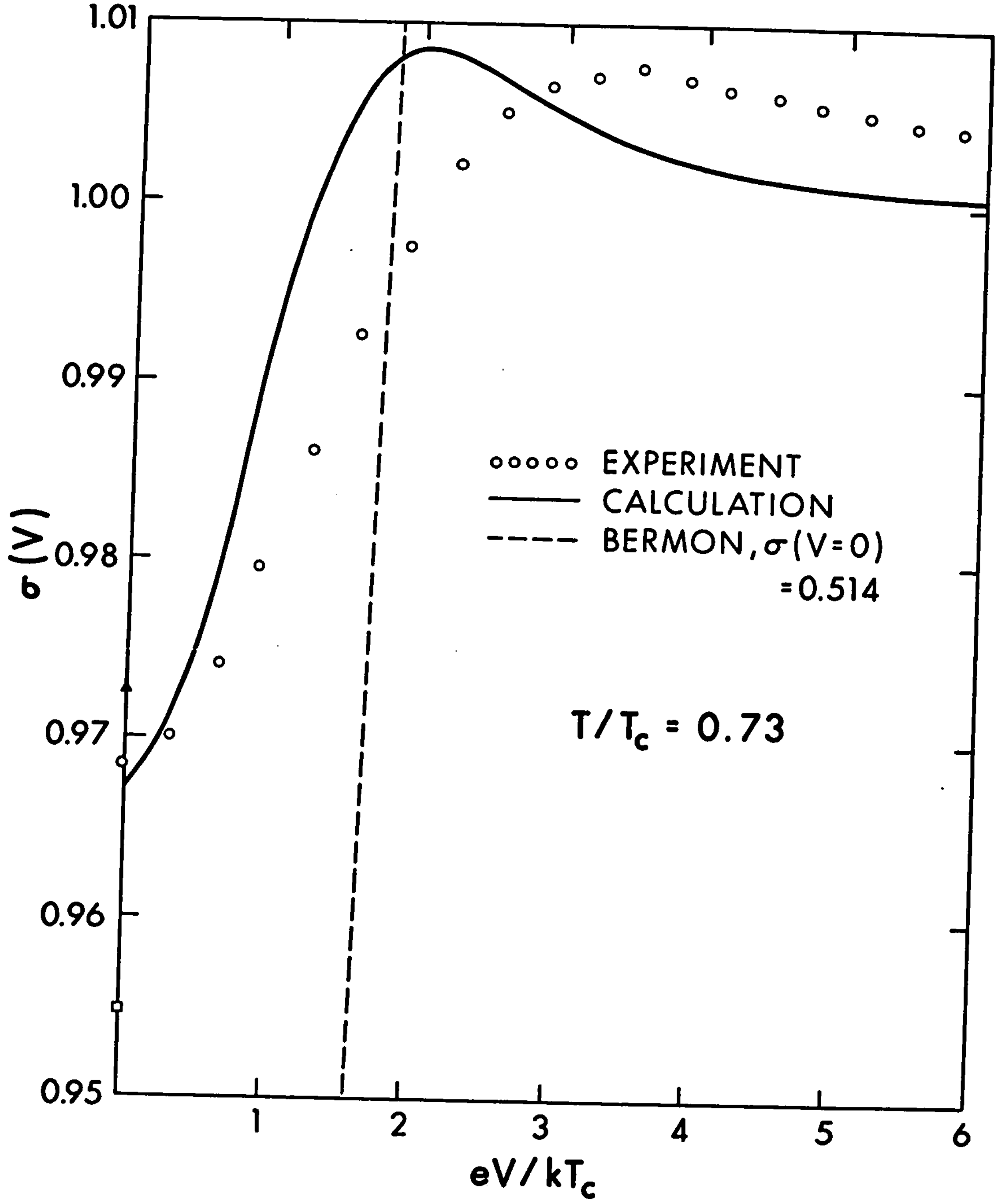
1.01
1.00
0.99
0.98
0.97
0.96
0.95
σ(V)
1
2
3
4
5
6
eV/kT_c
ooooo EXPERIMENT
CALCULATION
BERMON, σ(V=0)
=0.514
T/T_c = 0.73

sample, and $\Gamma_N = 0.047$ meV fits the slope n = 3.48 (see Fig.VI.3) which was determined from a plot like Fig.VI.2 for sample D81.

### VI.2.b Tunneling from a superconductor

Although tunneling into a proximity structure from a normal metal above 1°K is clearly distinguishable from that into an ordinary superconductor only after some analysis, the normalized conductance for tunneling from a superconductor into a weakly-coupled proximity sandwich exhibits the very characteristic multiple-peaked structure shown in Fig.VI.5. b. This curve was constructed for tunneling at 1.4°K between the density of states for aluminum and the McMillan density of states shown in Fig. VI.5. a. The expected energies of structure are indicated by arrows at $P1 \pm \Delta$ and $P2 \pm \Delta$. The structure at $P2 - \Delta$ is usually very small because the concentration of thermally excited electrons which contribute most of this peak and the change in the density of states in P2 are usually much smaller than in P1.

In Fig.VI.6 an experimental curve (for $d_N = 100$ Å, $d_S = 2260$ Å) is compared with a calculated curve using $\Gamma_N = 0.1$ meV and $\Gamma_S = 0.005$ meV. There are two possible ways of fitting the calculated and experimental curves. From experiment the peak separation can be measured and the resulting $\Gamma_N$ obtained from Fig.III.6b, or the position of structure P1 can be measured (taking account of the

FIG. VI.5

Illustration of the occurrence of multiple peak structure in the tunneling conductance between an ordinary superconductor and the N-side of an aluminum-tin proximity sandwich.

(a) The normalized densities of states in the superconducting aluminum, $N_{Al}$ (characterized by $\Delta_{Al} = 0.20$ meV, $\delta_{Al} = 0.013$), and proximity sandwich, $N_{prox}$ (characterized by $\Gamma_S = 0.025$ meV, $\Gamma_N = 0.5$ meV, $\Delta_S{}^{ph} = 0.56$ meV, and $\Delta_N{}^{ph} = 0.31$ meV). When voltage is applied the densities of states shift on the energy scale.

(b) The resulting calculated tunneling conductance at 1.4°K (continuous line). Expected structures at $P1 \pm \Delta$ and $P2 \pm \Delta$ are indicated by arrows.

For comparison the tunneling conductance between a normal metal and the same proximity sandwich at the same temperature is also plotted (dashed line).

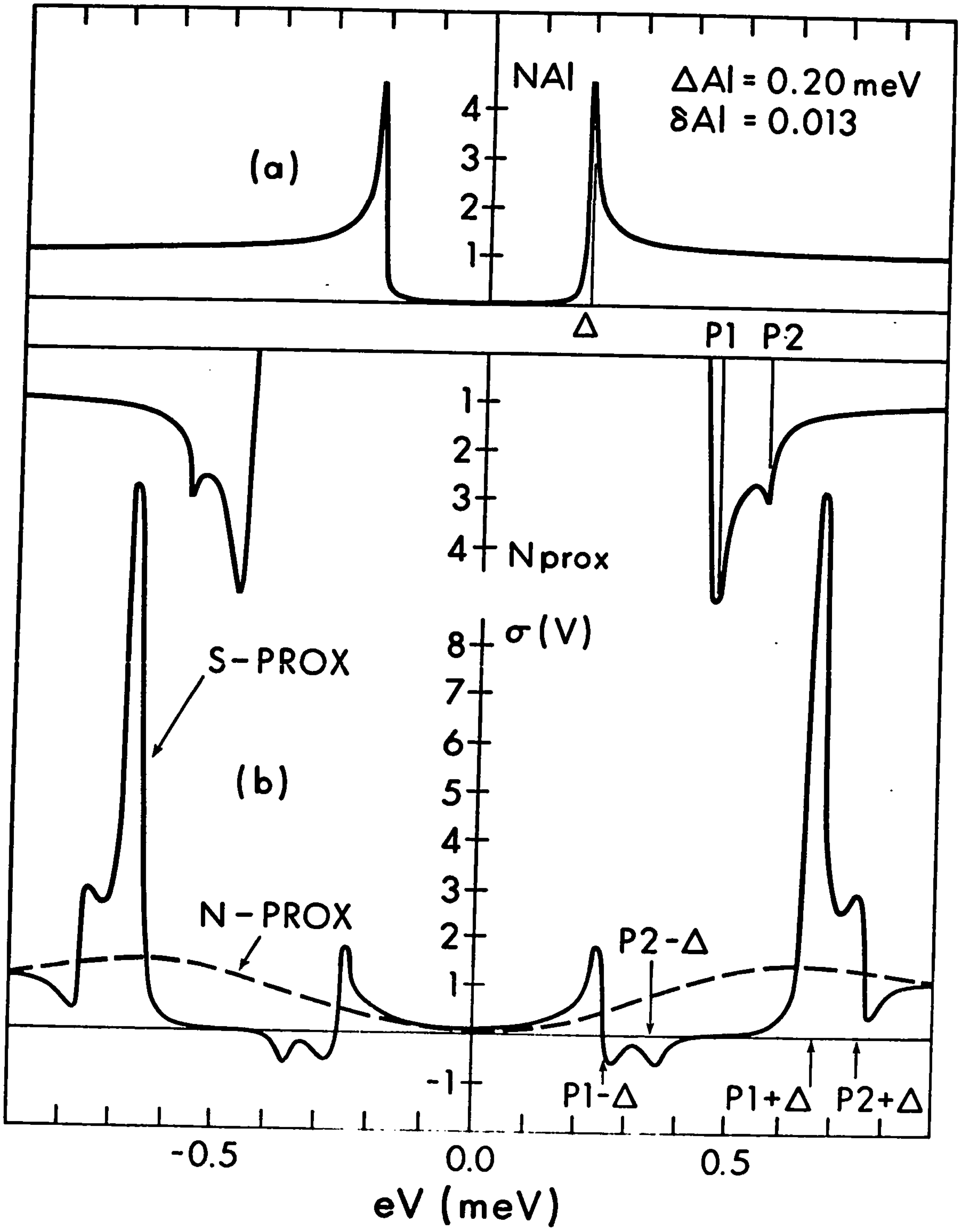
(a)
NAl
ΔAl = 0.20 meV
δAl = 0.013
4
3
2
1
Δ
P1
P2
1
2
3
4
Nprox
σ(V)
8
7
6
5
4
3
2
1
-1
S-PROX
(b)
N-PROX
P2-Δ
P1-Δ
P1+Δ
P2+Δ
-0.5
0.0
0.5
eV (meV)

FIG. VI.6

Comparison of experimental and theoretical normalized conductance for tunneling from superconducting aluminum into the N-side of aluminum-tin proximity sandwich.

——— experiment E82 , T = 1.4°K, $d_{Al}$ = 100 Å, and $d_{Sn}$ = 2260 Å.

------ calculated, $\Gamma_S$ = 0.005 meV, $\Gamma_N$ = 0.1 meV, $\Delta_S^{ph}$ = 0.56 meV,and $\Delta_N^{ph}$ = 0.22 meV. Aluminum electrode from which the tunneling was done is characterised by $\Delta_{Al}$ = 0.20 meV and $\delta$ = 0.013.

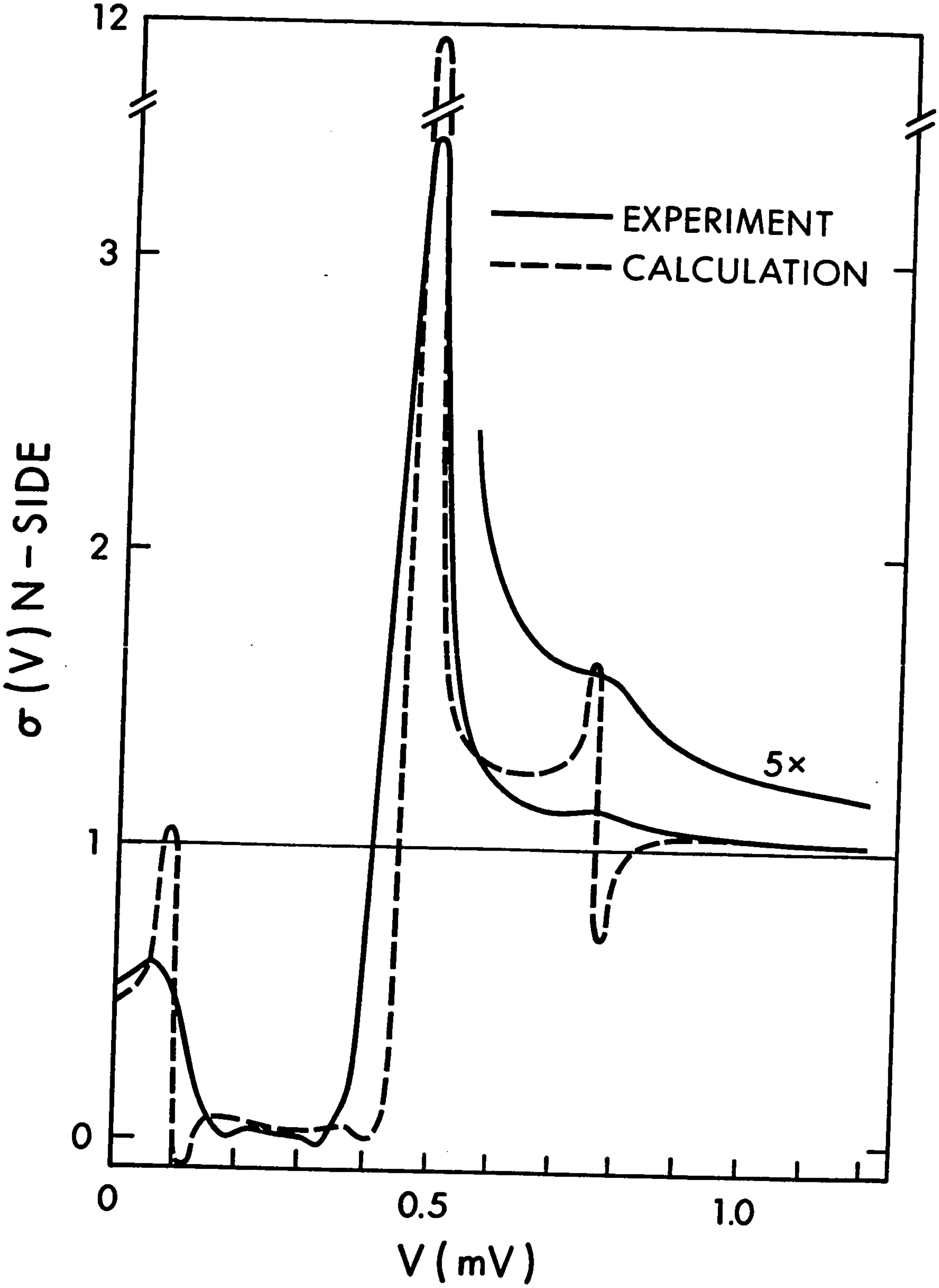

12
3
2
1
0
σ (V) N-SIDE
EXPERIMENT
CALCULATION
5×
0
0.5
1.0
V (mV)

influence of the gap of the pure aluminum electrode) and $\Gamma_N$ can be determined from Fig.III.6.a. Structure P1 is selected because its sensitivity to $\Gamma_N$ is higher than that of P2. The first method was used in constructing Fig.VI.6 and values of $\Delta_S^{ph}$ and $\Delta_N^{ph}$ were estimated from Fig.III.6.c. As expected the fit of the position of the structure is insensitive to $\Gamma_S$ so that the assumptions $B_N = B_S$ and $v_{FN} = v_{FS}$ are adequate. We then obtain $\Gamma_S/\Gamma_N \simeq d_N/d_S \simeq 0.05$ and $\Gamma_S = 0.005$ meV.

In Fig.VI.7 another experimental curve (for $d_N = 266$ Å, $d_S = 2370$ Å) is compared with a calculated curve using $\Gamma_N = 1.0$ meV and $\Gamma_S = 0.05$ meV. The fitting procedure is the same as for the curve in Fig.VI.6. We may see the difference in the shape of the curves for different transmission probabilities $\alpha$. For the curves in Fig.VI.6 the $\alpha$ is approximately 10 x bigger than for the curves in Fig.VI.7.

The structures on the calculated curves are sharper than the experimental structures. However our assumed density of states for aluminum has been shown to produce less sharply peaked structure than experiment (Fig.VI.1.a) so it cannot be responsible for this observed difference. A better fit to the shape of the structure in Fig.VI.6 would be obtained using $\Gamma_S = 0.05$ meV. This would require $B_N/B_S \simeq 10$ in order to keep $\Gamma_N = 0.1$. We do not know the exact theoretical dependence of the B values on the ratio of the mean free path to the thickness ($\ell/d$). However we may assume that if

FIG. VI.7

Comparison of experimental and theoretical normalized conductance for tunneling from superconducting aluminum into the N-side of an aluminum tin proximity sandwich.

——— experiment C93 , T = 1.395°K, $d_{Al}$ = 266 Å, and $d_{Sn}$ = 2370 Å.

---- calculated, $\Gamma_S$ = 0.05 meV, $\Gamma_N$ = 1.0 meV, $\Delta_S^{ph}$ = 0.56 meV, and $\Delta_N^{ph}$ = 0.34 meV. The aluminum electrode from which the tunneling was done is characterized by $\Delta_{Al}$ = 0.245 meV and $\delta$ = 0.013.

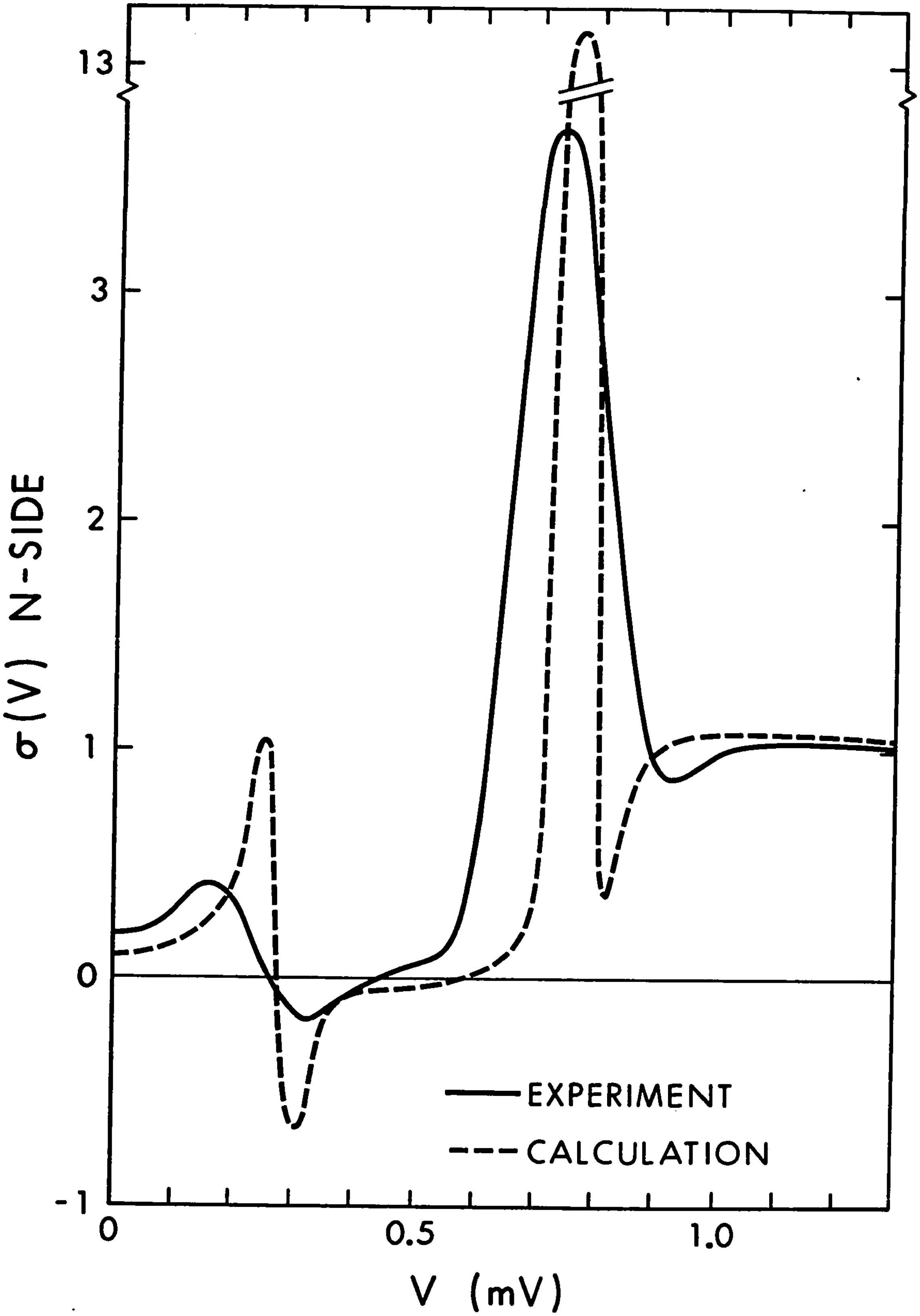
13
3
2
1
0
-1
σ(V) N-SIDE
0
0.5
1.0
V (mV)
EXPERIMENT
CALCULATION

$\ell/d \to 0$ then B goes monotonically to infinity (B is connected with average path of the electron in a given film; see App.I). Therefore, in order to get a better shape fit we have to assume that $\ell/d$ is smaller in the N-film than in the S-film so that $B_N/B_S \simeq 10$. This is qualitatively consistent with the experiment (see Chapter V.3), but because of unknown dependence of B on $\ell/d$ we cannot argue that the ratio $B_N/B_S \simeq 10$ is reached.

However the experimental curve may be a combination of different McMillan's curves such as would be obtained if the transmission probability $\alpha$ was not constant over the area of the junction.

The temperature dependence of McMillan's peak structure should follow the curves marked by P1 and P2 in Fig.III.3. This dependence is combined in the tunneling experiment with the BCS temperature dependence of the gap edge in the aluminum electrode, to form the temperature dependence of $P1 \pm \Delta$ and $P2 \pm \Delta$. The results of a typical experiment are plotted in Fig.VI.8. At most temperatures the structure $P2 - \Delta$ was not resolved but, since there are four structures and only three unknowns P1, P2, and $\Delta$, it is possible to calculate the unknowns at each temperature from three structures and reconstruct the position of the fourth or check the consistency of the method where all four structures are resolved. Also $\Delta$, the gap of the aluminum electrode, can be compared with the temperature variation of a BCS gap with $T_C = 1.7°K$ as has been done

FIG. VI.8

The temperature dependence of the peak positions

● experimental points corresponding to P1 − $\Delta$, P1 + $\Delta$, and P2 + $\Delta$, E82, $d_{Al} = 100$ Å, $d_{Sn} = 2260$ Å.

○ calculated positions of P2 − $\Delta$ using the experimental points. Note the consistency of the results at 1.63°K where calculated and experimental points coincide.

■ P1, □ P2 positions calculated from experimental points. In the lower graph the gap of the aluminum electrode is shown from which tunneling into the proximity structure was performed (○) as calculated from experimental points in the upper part. For comparison the BCS temperature variation of a gap is included.

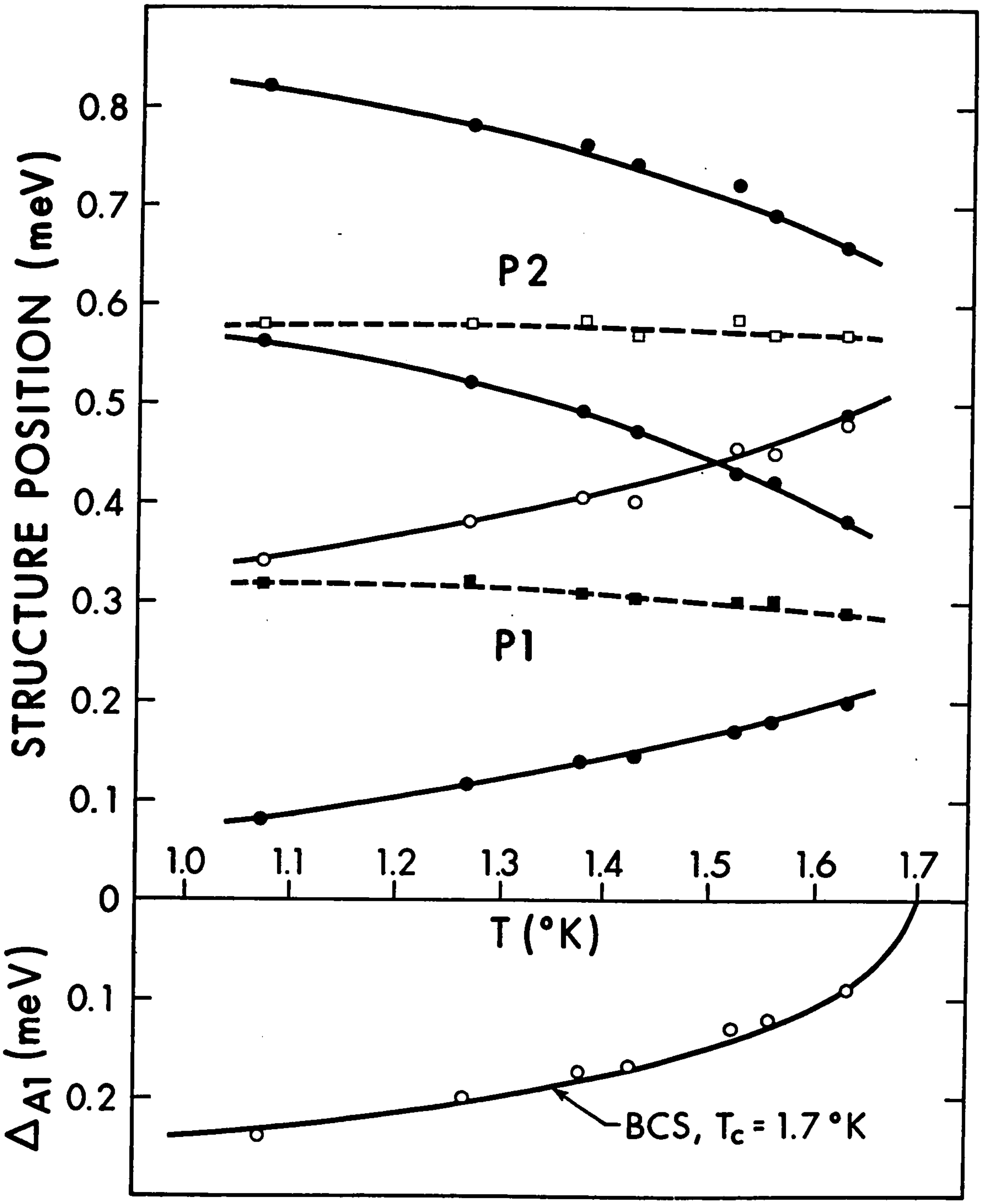

STRUCTURE POSITION (meV)
0.8
0.7
0.6
0.5
0.4
0.3
0.2
0.1
0
P2
P1
1.0
1.1
1.2
1.3
1.4
1.5
1.6
1.7
T (°K)
$\Delta_{A1}$ (meV)
0.1
0.2
BCS, $T_c$ = 1.7 °K

in the lower part of Fig.VI.8. Remarkably good agreement is obtained. The values of P2 from the McMillan model calculations lie within the scatter of the experimental values; whereas the values of P1 lie about 0.025 meV lower than the experimental curve at all temperatures.

Other experimenters have possibly seen some evidence of the multiple peaks in thicker films. Claeson et al (1967) observed structure with an aluminum-lead sandwich that they assigned to the superconducting properties of the contacts. It disappeared at lower temperatures, possibly because the smaller peaks are more difficult to resolve there. Adkins and Kington (1969) observed "unexplained dips in the density of states above the gap and structure at zero voltage" on the tunneling conductance from aluminum into a copper-lead proximity sandwich at 1.25°K. This is just the kind of structure to be expected if the aluminum was superconducting and their copper-lead sandwich had a clean interface with a high $\alpha$ (see Fig.VI.7). Freake and Adkins (1969) have observed broad multiple peaks in normal metal-proximity tunneling done at $T \simeq 0.06°K$ and Hauser (1966) reported structure near $\Delta$ for lead when tunneling into an aluminum-lead sandwich.

### VI.2.c Dependence of data on $\alpha$ and thickness

In Table II the $\Gamma_N$-values determined from experimental data by the three different methods discussed earlier are compared. Only the peak position method was used for the

# TABLE II

Transmission probability $\alpha$ and $\Gamma_N$ as a function of the oxidation conditions for Al-Sn proximity sandwiches at 1.4°K.(Tunneling into the aluminum side of a proximity sandwich).

| Section | Junction[a] | $d_N$(Å) | $d_S$(Å) | Peak Separation P2-P1 | | | Peak Position P1 | | | Slope n | | |
|---|---|---|---|---|---|---|---|---|---|---|---|---|
| | | | | P2-P1 (meV) | $\Gamma_N$ (meV) | $\alpha$ ($B_N$=2) | P1 (meV) | $\Gamma_N$ (meV) | $\alpha$ ($B_N$=2) | n | $\Gamma_N$ (meV) | $\alpha$ ($B_N$=2) |
| I | A84 | 105 | 2300 | 0.10 | 0.5 | 0.066 | 0.65 | 1.0 | 0.13 | | | |
| | A85 | 123 | 1030 | | | | 0.65 | 1.0 | 0.16 | | | |
| | B87 | 113 | 397 | 0.085 | 0.6 | 0.085 | 0.45 | 0.5 | 0.072 | | | |
| | C92 | 39 | 790 | | | | 0.56 | 2.0 | 0.097 | 1.01 | 2.0 | 0.097 |
| | C93 | 266 | 2370 | | | | 0.49 | 0.7 | 0.23 | 1.37 | 0.4 | 0.13 |
| II | D81 | 115 | 3150 | 0.20 | 0.22 | 0.032 | 0.30 | 0.13 | 0.043 | 3.48 | 0.047 | 0.0078 |
| | E82 | 100 | 2260 | 0.26 | 0.15 | 0.018 | 0.27 | 0.10 | 0.034 | 5.20 | 0.02 | 0.0026 |
| | E83 | 67 | 2480 | 0.17 | 0.34 | 0.028 | 0.52 | 0.7 | 0.044 | 1.17 | 0.55 | 0.046 |
| | F90 | 42 | 783 | 0.20 | 0.22 | 0.011 | 0.50 | 0.8 | 0.041 | 1.05 | 1.0 | 0.051 |
| | F91 | 221 | 821 | 0.39 | 0.025 | 0.0068 | 0.29 | 0.12 | 0.033 | 2.81 | 0.05 | 0.014 |
| III | G89 | 105 | 910 | | | | 0.14 | 0.02 | 0.0026 | | | |
| | H53[b] | 89 | 1450 | | | | 0.08 | 0.009 | 0.0010 | | | |
| | H54[b] | 117 | 2120 | | | | 0.10 | 0.01 | 0.0015 | | | |

[a] Junctions designated by the same letter were prepared at the same time on the same substrate.

[b] These specimens were exposed to room atmosphere before measurement.

samples of Sec.III because neither $T_C$ nor the position P2 could be accurately determined for these weakly-coupled (low $\alpha$) sandwiches. The $\alpha$-values were determined using eq.III.4 and putting $B_N = 2$ which may be an assumption of limited accuracy because $B_N$ probably rises rapidly above this value if the condition $\ell_N >> d_N$ is not fulfilled.

The difference among the $\alpha$-values determined by the three methods arises partly because bulk values of $\omega_C$ and $\lambda$ for aluminum were used in the self-consistent calculations whereas it is well-known that different values apply to thin films (see Strongin et al(1965)).These bulk values mainly affect the relationship between n and $\Gamma_N$ for the McMillan model and thus affect the reliability of the slope method of determining $\Gamma_N$ because of its dependence on $T_C$. However it is clear that $\alpha$ decreases systematically as the amount of oxidation at the interface increases, being in about the ratio 80:20:1 for the samples of Sec.I, II and III respectively. This range of $\alpha$-values was achieved by creating the following conditions during the time interval $\Delta t$ between the evaporation of the aluminum and tin.

Sec.I samples: pressure ~ $2 \times 10^{-7}$ Torr, $\Delta t \simeq 1$ min, and a shield around the sample was held at liquid nitrogen temperatures.

Sec.II samples: pressure ~ $5 \times 10^{-7}$Torr, $\Delta t \simeq 1$ min.

Sec.III samples: specimen chamber isolated from pumps, pressure >> $10^{-7}$Torr for $\Delta t \simeq 10$ min. All pressures were read on a cold-cathode ionization gauge.

The process of trying to control $\alpha$ is very complex and cannot be done with precision. In a vacuum of $3 \times 10^{-6}$ Torr a monolayer strikes a clean surface in about one sec so one cannot hope for an ideally clean surface especially on aluminum, which oxidizes readily. Adsorbed layers are partially penetrated by the next metal that is evaporated so that interface properties will depend on many factors including the specific metals involved (see Handy (1962)).

Finally it may be noted from Table II that the measurable parameters depend on the thickness $d_N$ in accord with the McMillan model. Samples from different sections cannot be compared because the $\alpha$-dependence masks the thickness effect. Samples prepared at the same time provide the most striking comparison; for example the E samples have $d_N(E82)/d_N(E83) = 1.5$ whereas from the peak separation method $\Gamma_N(E83)/\Gamma_N(E82) = 1.55$. As expected the properties are only slightly dependent on the thickness of the tin film.

Experiments with thicker films would be interesting but it will then be more difficult to satisfy the condition $\ell > d$ necessary for the McMillan model. It would be valuable to have a model that would connect the De Gennes (1964a) assumption of the dirty limit in thick S-films with McMillan's assumptions in thin N-films.

## VI.3 Tunneling into the S-side of a Proximity Sandwich

### VI.3.a Tunneling from a normal metal

In contrast to tunneling into the N-side of a proximity sandwich tunneling from a normal metal into the S-side of a sandwich does not offer any information that will aid in the identification of the parameters of the proximity sandwich. The dependences of $[ 1 - \sigma(0)]$ on $( 1 - T/T_C)$, as calculated from the McMillan model, are very close to the BCS dependences. These results are to be expected because in the S-side of the proximity sandwich the peak P2 in the density of states is more dominant. For all $\alpha$ the temperature dependence of this peak (see Fig.III.4) resembles the temperature dependence of the gap in a BCS superconductor and therefore the behaviour of the proximity sandwich must be BCS-like.

The observations agree quite well with the theoretical predictions. The plot of the experimental dependences for three junctions with different $\alpha$ is presented in Fig.VI.9. The slopes are very close to unity but in some cases the lines are shifted toward smaller values of $1 - \sigma(0)$. The largest shift was observed for junction Q30 in Fig.VI.9. The shift could be caused by a background conductivity (zero bias anomaly) that varies with temperature, or by variation of $\alpha$ over the sample area, or by a combination of both effects. A variation of $\alpha$

FIG. VI. 9

The experimental dependence of $[\ 1 - \sigma(V = 0)]$ on $(1 - T/T_C)$. $\sigma(V = 0)$ is the normalized tunneling conductance at zero bias between a normal metal and the S-side of an aluminum - tin proximity structure.

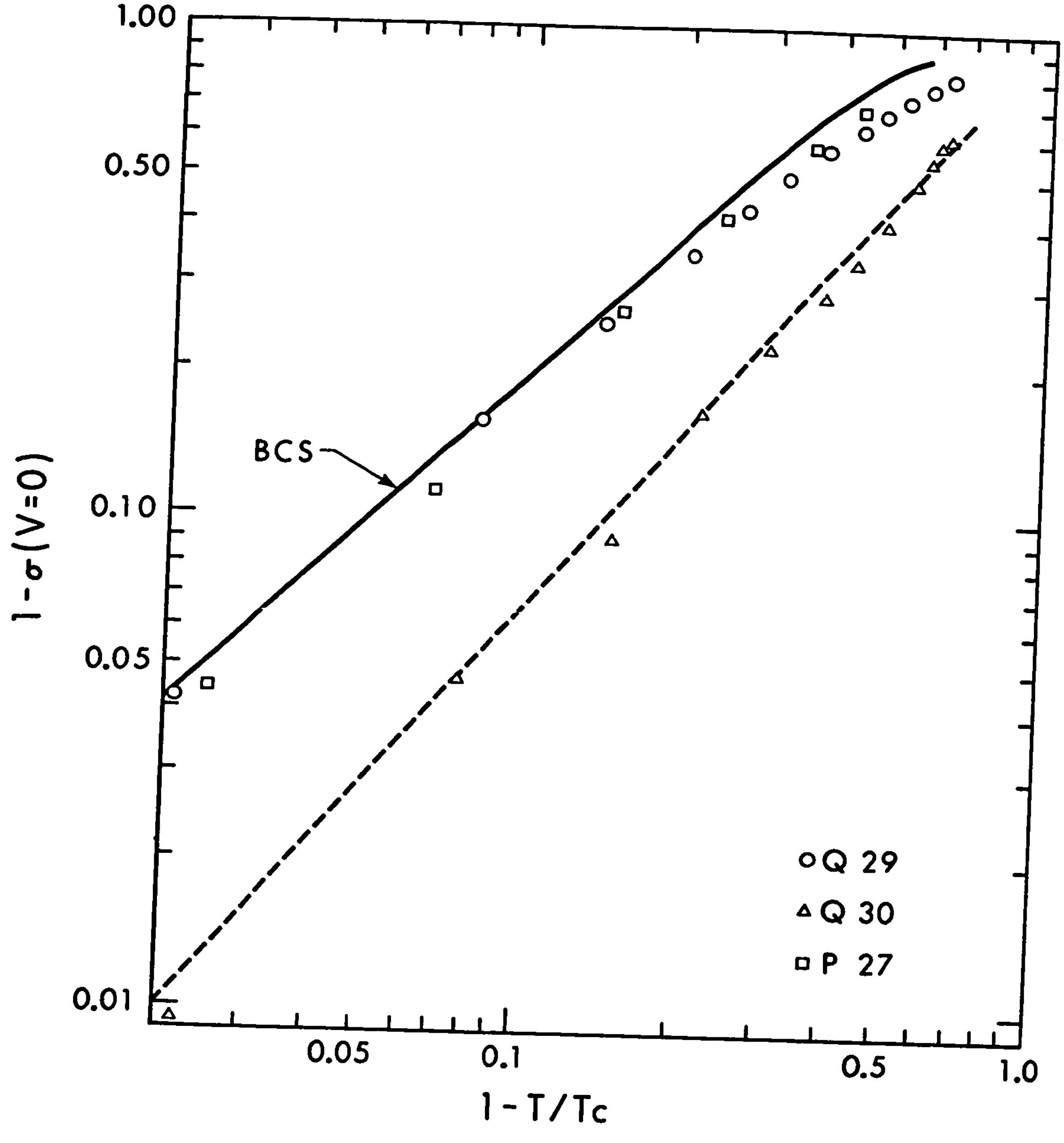
1.00
0.50
0.10
0.05
0.01
1 - σ(V=0)
BCS
0.05
0.1
0.5
1.0
1 - T/Tc
○ Q 29
△ Q 30
□ P 27

could affect the plot in the following way. The measured critical temperature, $T_C$, will correspond to the part of the junction with the smaller $\alpha$ and therefore $1 - T/T_C$ will be shifted to higher values, while $\sigma(0)$ will be equal to that for the majority of the junction area.

### VI.3.b Tunneling from a superconductor

The normalized conductance for tunneling from a superconductor into the S-side of a weakly - coupled proximity sandwich exhibits the multiple - peaked structure shown in Fig.VI.10.b. The curve was constructed for tunneling at 1.1°K between the density of states for aluminum (see Chapter VI.1) and the McMillan density of states shown in Fig.VI.10.a. The expected positions of the structure are indicated by arrows at $P1 \pm \Delta$ and $P2 \pm \Delta$. One can see very poor coincidence between the expected energy of the structure and actual energy of the peak maxima. Also, in certain cases a peak appears in the normalized tunneling conductance associated with a dip in the McMillan density of states so that extra peaks sometimes appear. These effects make final interpretation of the tunneling conductance curves quite difficult.

In Fig.VI.11 an experimental curve at 1.4°K for junction 022 is compared with a calculated curve using $\Gamma_S = 0.03$ meV and $\Gamma_N = 0.012$ meV. The value for $\Gamma_S$ was found by fitting the peak position to Fig.III.7 and $\Gamma_N$ was found from the condition $\Gamma_S/\Gamma_N = d_N/d_S$, obtained by assuming

FIG. VI. 10

Illustration of the occurrence of multiple peak structure in the tunneling conductance between an ordinary superconductor and the S-side of an aluminum-tin proximity sandwich.

(a) The normalized density of states in the superconducting aluminum, $N_{Al}$ (characterized by $\Delta_{Al} = 0.24$ meV, $\delta_{Al} = 0.013$), and proximity sandwich, $N_{prox}$ (characterized by $\Gamma_S = 0.05$ meV, $\Gamma_N = 0.01$ meV, $\Delta_S^{ph} = 0.539$ meV, and $\Delta_N^{ph} = 0.141$ meV). When voltage is applied the densities of states shift on the energy scale.

(b) The resulting calculated tunneling conductance at 1.1°K (———). Expected structures at P1 ± Δ and P2 ± Δ are indicated by arrows.

For comparison the tunneling conductance between a normal metal and the same proximity sandwich at the same temperature is also plotted (-----).

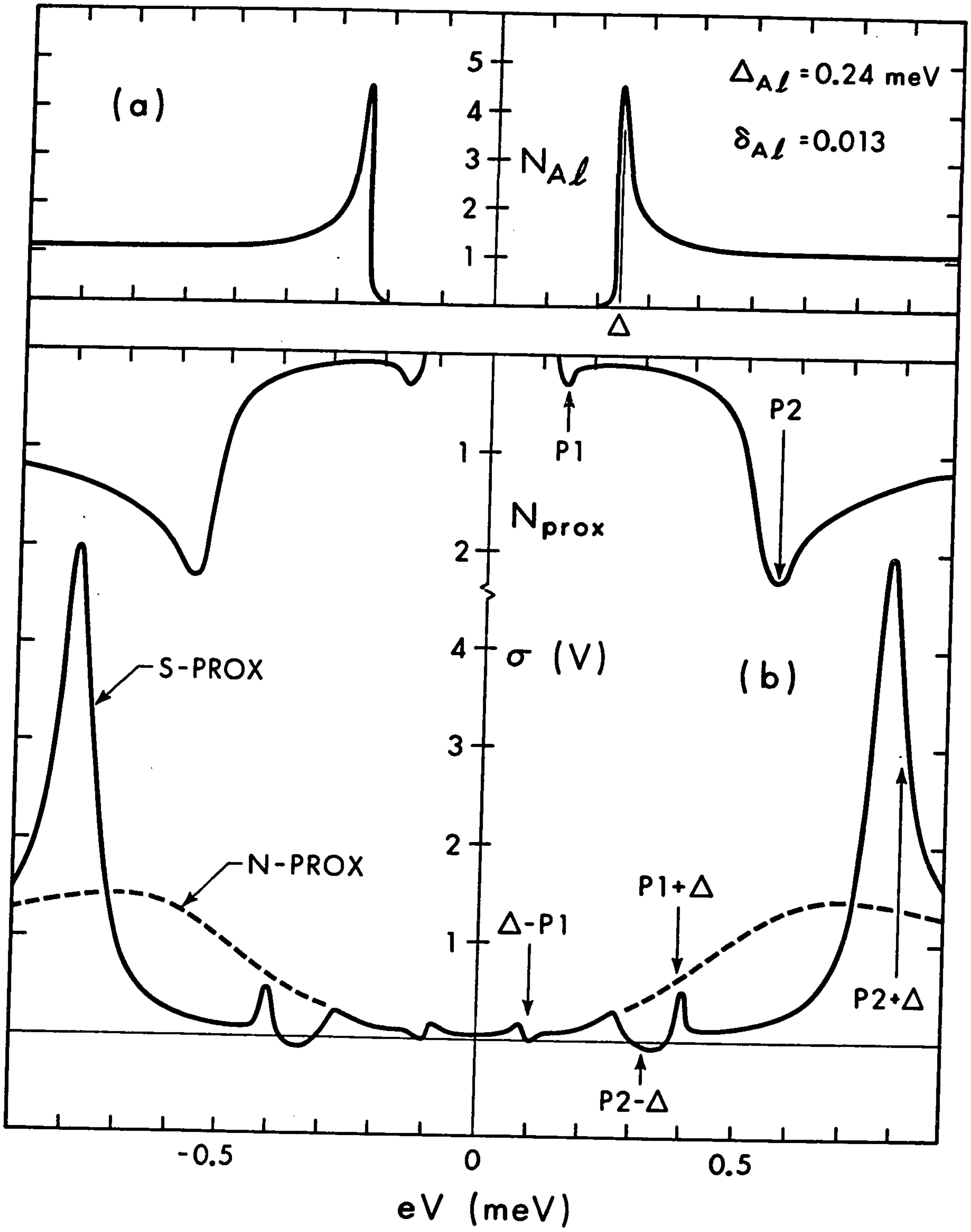
(a)
5
4
3
2
1
$N_{A\ell}$
$\Delta_{A\ell}$ = 0.24 meV
$\delta_{A\ell}$ = 0.013
$\Delta$
P1
P2
1
2
$N_{prox}$
4
3
2
1
$\sigma$ (V)
(b)
S-PROX
N-PROX
$\Delta$-P1
P1+$\Delta$
P2-$\Delta$
P2+$\Delta$
-0.5
0
0.5
eV (meV)

FIG. VI. 11

Comparison of experimental and theoretical normalized conductance for tunneling from superconducting aluminum into the S-side of aluminum-tin proximity sandwich.

——— experiment 022, T = 1.4°K, $d_{Al}$ = 2790 Å, $d_{Sn}$ = 1015 Å.

----- calculated, $\Gamma_S$ = 0.03 meV, $\Gamma_N$ = 0.012 meV, $\Delta_S^{ph}$ = 0.55 meV, $\Delta_N^{ph}$ = 0.10 meV.

Aluminum electrode from which the tunneling was done is characterized by $\Delta_{Al}$ = 0.12 meV, and $\delta$ = 0.013.

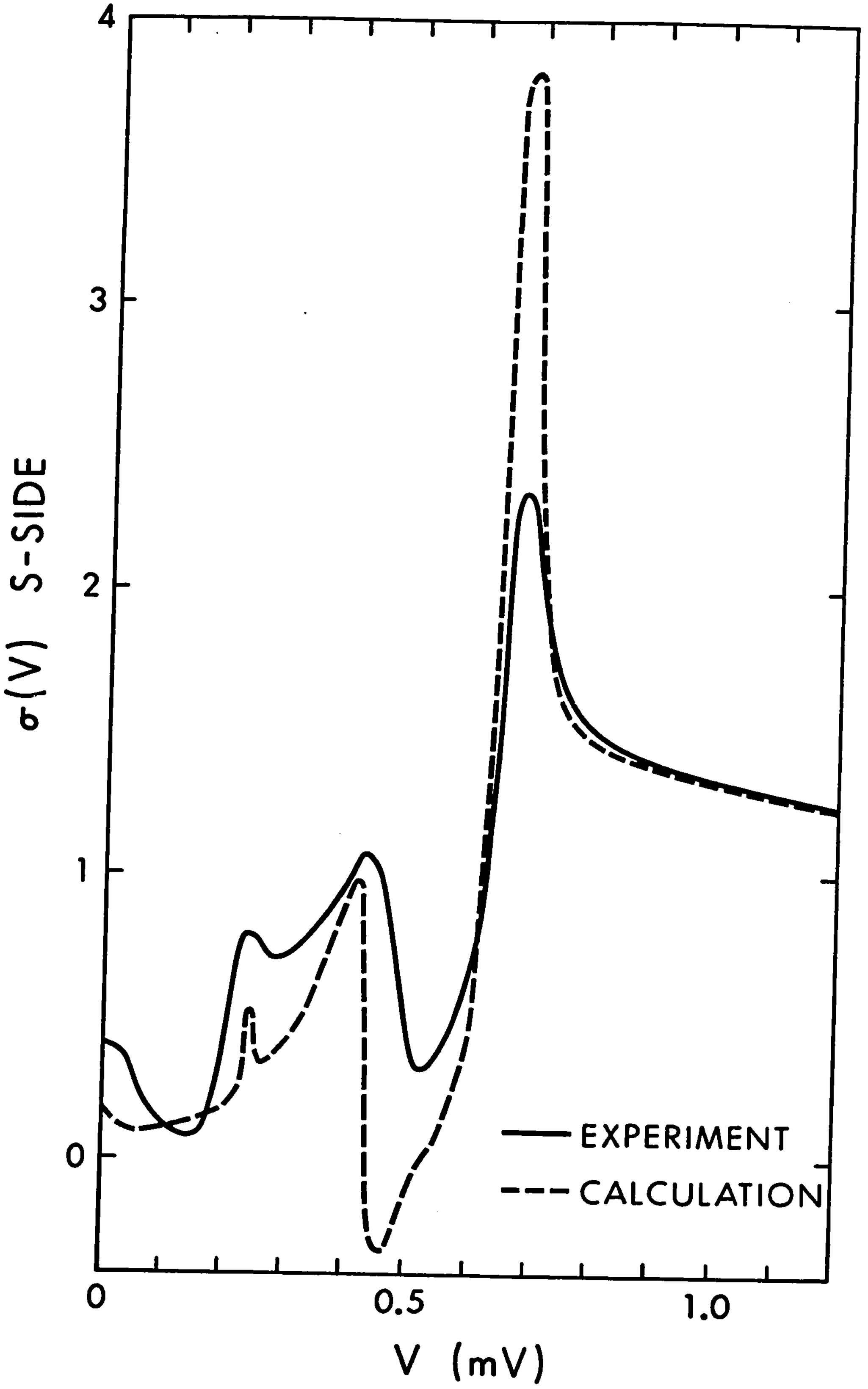
σ(V) S-SIDE
4
3
2
1
0
0
0.5
1.0
V (mV)
EXPERIMENT
CALCULATION

$B_N = B_S$ and $v_{FN} = v_{FS}$. The peak positions agree quite well, but the structure on the calculated curve is sharper than the experimental structure. However the experimental curve may be a combination of different McMillan curves such as would be obtained if the transmission probability $\alpha$ was not constant over the area of the junction.

The temperature dependence of $P1 \pm \Delta$ and $P2 \pm \Delta$ should arise from the combination of the temperature dependence of the McMillan peak structure (see Fig.III.4) and the BCS temperature dependence of the gap edge in the aluminum electrode. The results of a typical experiment are plotted in Fig.VI.12. Since there are four structures and only three unknowns P1, P2, and $\Delta$, it is possible to calculate the unknowns at each temperature from three structures and reconstruct the position of the fourth or check the consistency of the method where all four structures are resolved. The values of P1 and P2 as calculated from the experimental points of $P1 \pm \Delta$ and $P2 \pm \Delta$ are compared with the theoretical values (----). Also $\Delta$, the gap of the aluminum electrode, can be compared with the temperature variation of a BCS gap with $T_C = 1.6°K$ as has been done in the lower part of Fig.VI.12. Remarkably good agreement is obtained.

### VI.3.c Dependence of data on $\alpha$

In Tables III and IV the $\Gamma_S$-values determined from the experimental data, and the transmission probabilities $\alpha$

FIG. VI. 12

The experimental temperature dependence of the peak positions.

● experimental points corresponding to Δ- P1, P1 + Δ, P2 - Δ, and P2 + Δ, junction 022.

○ calculated values using the experimental points. Note the consistency of the results for Δ - P1.

■ P1, □ P2 positions calculated from experimental points.

In the lower graph the gap of the aluminum electrode is shown from which tunneling into the proximity structure was performed (○) as calculated from the experimental points in the upper part. For comparison the BCS temperature variation of a gap is included.

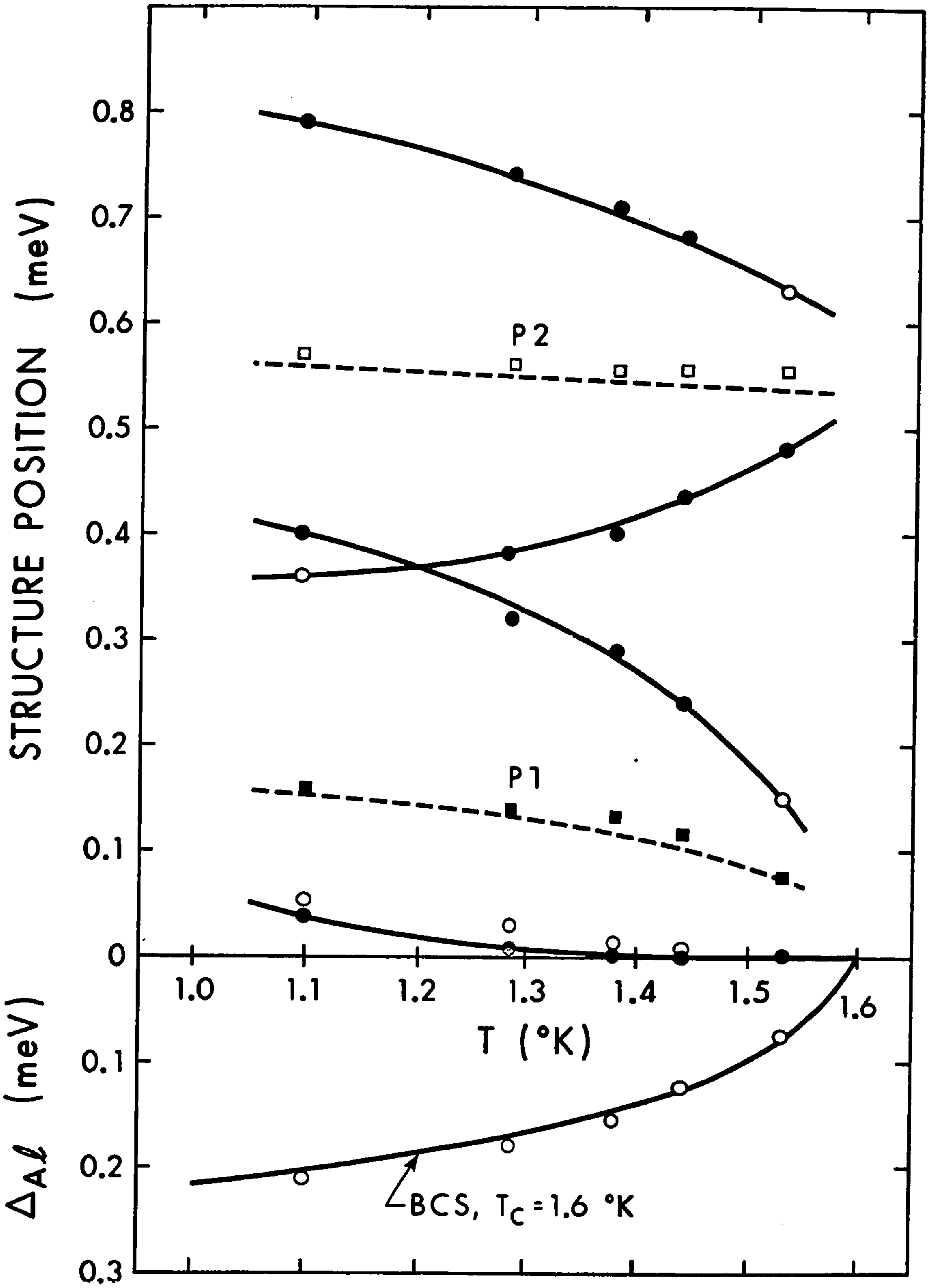
STRUCTURE POSITION (meV)
0.8
0.7
0.6
0.5
0.4
0.3
0.2
0.1
0
P 2
P 1
1.0
1.1
1.2
1.3
1.4
1.5
1.6
T (°K)
$\Delta_{A\ell}$ (meV)
0.1
0.2
0.3
BCS, $T_C$ = 1.6 °K

calculated from them, are presented. The $\Gamma$ values were determined by two different methods; first by comparison of the experimental critical temperature $T_C$ with Fig.III.5, and secondly by comparison of the experimental values of peak positions with Fig.III.7. The $\alpha$-values were determined using eq.III.4 and putting $B_S = 2$.

In Table III there are presented the junctions in which the transmission probability $\alpha$ was controlled by different amounts of oxidation of the tin layer. It is clear that $\alpha$ decreases systematically as the amount of oxidation at the interface increases, being in about the ratio 200:30:1 for the samples of Sec.I, II, and III respectively. This range of $\alpha$ values was achieved by creating the following conditions during the time interval $\Delta t$ between the evaporation of tin and aluminum.

Sec.I: pressure $\sim 5 \times 10^{-7}$ Torr, $\Delta t \approx 60$ sec.
Sec.II: pressure $\sim 0.2$ Torr of oxygen dried in liquid nitrogen trap, $\Delta t \approx 100$ sec.
Sec.III: pressure $\sim 0.2$ Torr of dry oxygen, $\Delta t \approx 1000$ sec.

When Sec.I of Table III is compared with Sec.II of Table II (in which the oxidation conditions are about the same) one can immediately see that the $\alpha$ obtained by the oxidation of aluminum is much smaller than the $\alpha$ obtained by the oxidation of tin, which is to be expected because aluminum oxidizes more readily then tin does.

The $\alpha$-value derived from the critical temperature is

## TABLE III

Transmission probability $\alpha$ and $\Gamma_S$ as a function of the oxidation conditions for Sn-Al proximity sandwiches. Peaks P1 and P2 are measured at 1.4°K, unless otherwise stated. (Tunneling into the tin side of a proximity sandwich).

| Section | Junction[a] | $d_S$ (Å) | $d_N$ (Å) | $\frac{\Gamma_S}{\Gamma_N}=\frac{d_N}{d_S}$ | Critical Temperature, $T_c$ |  |  | Peak positions P1 and P2 |  |  |  |
|---|---|---|---|---|---|---|---|---|---|---|---|
|  |  |  |  |  | $T_c$ (°K) | $\Gamma_s$ (meV) | α (B=2) | P1 (meV) | P2 (meV) | $\Gamma_s$ (meV) | α (B=2) |
| I | M17 | 457 | 2405 | 5.27 | 2.16 | 0.26 | 0.15 | 0.31 |  | 0.7 | 0.40 |
|  | N19 | 688 | 2200 | 3.20 | 1.90 | 0.35 | 0.30 | 0.30 |  | 0.6 | 0.52 |
|  | O21 | 822 | 1679 | 2.04 | 2.19 | 0.41 | 0.42 | 0.25 |  | 0.4 | 0.41 |
|  | P27 | 578 | 1176 | 2.03 | 2.35 | 0.26 | 0.19 | 0.39[b] |  | 0.9 | 0.65 |
|  | P28 | 918 | 1053 | 1.15 | 2.59 | 0.35 | 0.39 | 0.35[b] |  | 0.6 | 0.69 |
| II | O22 | 1015 | 2790 | 2.75 | 3.49 | 0.036 | 0.045 | 0.09 | 0.56 | 0.04 | 0.050 |
|  | Q30 | 617 | 767 | 1.24 | 3.42 | 0.043 | 0.035 | 0.22[b] | 0.56[b] | 0.04 | 0.031 |
|  | R32 | 995 | 1105 | 1.11 | 3.10 | 0.060 | 0.049 |  |  |  |  |
| III | Q29 | 575 | 732 | 1.27 | 3.76 | <0.0073 | <0.01 | 0.11[b] | 0.60[b] | 0.002 | 0.0014 |
|  | R31 | 532 | 680 | 1.28 | 3.76 | <0.0070 | <0.01 | ~0.02 | 0.58 | 0.001 | 0.0008 |

[a] Junctions designated by the same letter were prepared at the same time on the same substrate.

[b] These values were measured at 1.1°K.

smaller than that derived from the peak positions. The difference may be explained by slight non-uniformity of the oxide layer which forms the barrier between the films in proximity. Regions with thicker oxide will have a smaller value of $\alpha$ and higher value of $T_C$. In the experiment we will detect the highest $T_C$ in the sample, thus getting a smaller value of $\alpha$ than the average value which is measured by the peak positions.

The discrepancy between the $\alpha$ values determined by the two methods is most remarkable in Sec.I. This probably arises from the fact that the McMillan model is valid only for $\alpha << 1$, while the values of $\alpha$ in this section range from 0.15 to 0.70.

We have also attempted to control $\alpha$ by another means. The results are collected in Table IV.

A thin layer of SiO was evaporated in between the aluminum and tin in junctions K and L. The thickness of SiO was calculated from the density $\rho = 2.165 \ g/cm^3$ and known mass sensitivity of the frequency of the quartz crystal thickness monitor. The sandwiches produced in this way usually exhibited more peaks in the conductance curve than predicted by the McMillan model. When the peaks were plotted against temperature, it looked as if peaks from different junctions were drawn onto the same sheet of paper. We assigned this behaviour to the inhomogeneity of the SiO layer, which probably condenses in islands. The resulting effect is equivalent to two junctions in parallel,

## TABLE IV

Transmission probability α for barriers formed by the evaporation of SiO or glow discharge oxidation. Peaks P1 and P2 are meassured at 1.4°K. (Tunneling into the tin side of a proximity sandwich).

| Junction[a] | Formation of $\alpha$ | $d_S$ (Å) | $d_N$ (Å) | $\frac{\Gamma_S}{\Gamma_N}=\frac{d_N}{d_S}$ | Critical temperature $T_c$ | | | Peak positions P1 and P2 | | | |
|---|---|---|---|---|---|---|---|---|---|---|---|
| | | | | | $T_c$ (°K) | $\Gamma_S$ (meV) | $\alpha$ ($B_S$=2) | P1 (meV) | P2 (meV) | $\Gamma_S$ (meV) | $\alpha$ ($B_S$=2) |
| K12 | 4Å SiO | 992 | 1680 | 1.69 | 3.49 | 0.034 | 0.042 | 0.158 | 0.458 | 0.30 | 0.57 |
| K11 | 8Å SiO | 470 | 1620 | 3.44 | 3.67 | 0.021 | 0.012 | 0.158 | 0.481 | 0.20 | 0.12 |
| L13 | 12Å SiO | 536 | 1673 | 3.12 | 3.70 | 0.013 | 0.0084 | 0.09 | 0.60 | 0.05 | 0.034 |
| L14 | 18Å SiO | 970 | 1731 | 1.79 | 3.79 | <0.0054 | <0.0065 | 0.08 | 0.585 | 0.04 | 0.049 |
| I4 | glow discharge[b] | 1015 | 56 | 0.055 | | | | | 0.61 | <0.05 | <0.0063 |
| J6 | glow discharge[b] | 630 | 920 | 1.46 | | | | | 0.62 | <0.05 | <0.0039 |

[a] Junctions designated by the same letter were prepared at the same time on the same substrate.

[b] The glow discharge current was 1mA for 60 sec in 0.15 Torr of dry $O_2$.

one with a high value of $\alpha$ and the other one with a small value of $\alpha$. Also a very large discrepancy between $\alpha$ determined from $T_C$ and from the peak positions (the strongest sets of peaks were chosen) speaks for a large variation of $\alpha$.

The glow discharge method was employed to control the value of $\alpha$ in the junctions I and J. The method produced very thick oxide and resulted in very weak coupling between the films.

# CHAPTER VII

## SUGGESTIONS FOR FURTHER WORK

A most interesting extension of the present experiments would be the fabrication of a double-junction in which the tunneling characteristics of a proximity sandwich could be measured from both aluminum and tin sides simultaneously. One should then be able to compare the value of $\alpha$ and the positions of the peaks P1 and P2 as measured from both sides of the sandwich. However such a double-junction, requiring the evaporation of four metal films and three oxidation procedures, would be rather difficult to fabricate.

Of some interest would be experiments in which the critical temperature of the base layer was higher than the critical temperature of the proximity sandwich (e.g. junctions Pb-I-Al, Sn, or Sn-I-Sn, Al, where I stands for the tunneling barrier). One should be able to measure the temperature dependence of the peak positions over a broader range of reduced temperature $T/T_C$ in such a junction. Also the peaks would be further separated and they would not be mixed up at $V = 0$.

The McMillan theory should also be tested for a pair of metals, one of which is a superconductor and the other one a "real" normal metal, which is known not to be superconducting. The best choice would probably be copper and lead, which have already been extensively studied in the De Gennes approximation (i.e. thick films with short mean free path and with coupling between them as strong as possible).

From the theoretical point of view the general dependence of the McMillan model on the mean free path should be established, or at least, introduction of the diffusion limit into the McMillan model, as suggested by Deutscher and De Gennes (1969), should be done. This should open further possibilities for the experimental investigation.

# CHAPTER VIII

## CONCLUSION

The tunneling characteristics of junctions between aluminum and both sides of proximity sandwiches formed by evaporated films of aluminum and tin have been measured and the experimental results compared with a computer analysis using the McMillan model.

To fulfil the assumptions of the McMillan model the coupling of the proximity films has been limited by allowing slight oxidation at the interface. The oxidation of the interface in dry oxygen or in "vacuum" (pressure $\simeq 10^{-6}$Torr) produced values of the transmission probability $\alpha$ which are qualitatively quite consistent with the different oxidation conditions and the kind of oxidized surface (either tin or aluminum). Glow-discharge-assisted oxidation produced extremely weak coupling between the metals in proximity. Thin evaporated layers of SiO were not suitable for decoupling of the metals, because they were not homogeneous.

The junction conductance at zero bias when tunneling from normal aluminum into the aluminum side of the proximity sandwich has been compared in the vicinity of the critical temperature of the sandwich with the empirical expression

$$1 - \sigma(0) = \text{constant}\ (1 - T/T_C)^n. \qquad \text{VIII.1}$$

Values from n = 1 to 6 have been obtained. The McMillan model predicts the observed magnitude of $\sigma(0)$ and very nearly this temperature dependence, although for the higher n-values the experimental data fit the empirical law somewhat better than the model calculations do. The measured conductance as a function of voltage fits the McMillan model very well.

When tunneling from normal aluminum into the tin side of the sandwich is performed in the vicinity of the critical temperature of the sandwich the McMillan model predicts the BCS value n = 1 in relationship VIII.1 for the junction conductance at zero bias. Experimentally n = 1 also but sometimes the constant required to fit eq.VIII.1 is smaller than for BCS superconductors. The shift in constant may be attributed to a variable background conductivity and to inhomogeneity of the decoupling barrier.

When tunneling from a superconductor into a proximity sandwich is performed a multi-peaked conductance curve is observed and compares well in some detail with the predictions of the McMillan model. The positions of the peaks and their variation with temperature as well as their dependence on the proximity film coupling and thickness of the normal (aluminum) film have all been compared with theory and agreed well. Those discrepancies that exist may be largely a result of applying calculations using properties of bulk aluminum to experiments with thin films for tunneling into the aluminum side of the sandwich or a result of slight inhomogeneities in the decoupling barrier for tunneling into the tin side of a sandwich.

The McMillan theory predicts sharper peaks than the observed ones. The broader peaks in the experiment may be explained by superposition of different McMillan curves with slightly different $\alpha$.

As a whole the McMillan model accounts well for the observed behaviour of aluminum-tin proximity sandwiches.

# APPENDIX I

## THE CALCULATION OF THE FUNCTION B

The value of the function B in the McMillan tunneling model of the proximity effect will be calculated under the following assumptions:

(a) the mean free path is infinite,

(b) the reflection on the back face of the film is specular,

(c) the probability dw that an electron penetrates the barrier to enter the film within a solid angle $d\Omega$ at an angle $\Theta$ to the normal obeys the cosine law.

The situation is illustrated in the figure below where the plane of the thin film of the thickness d is perpendicular to the z axis.

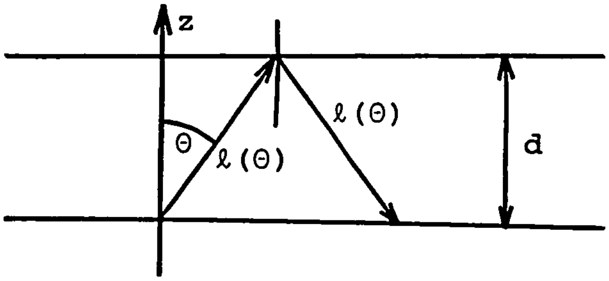

We may write

$$dw = w_\circ \cos\Theta \, d\Omega,$$

where $d\Omega = 2\pi\sin\Theta d\Theta$. $w_\circ$ can be found from the normalization equation

$$1 = \int_0^{\pi/2} dw = 2\pi w_\circ \int_0^{\pi/2} \cos\Theta\sin\Theta \, d\Theta = \pi w_\circ .$$

The path which is travelled in the film of thickness d by an electron which enters the film at angle $\Theta$ is

$$2\ell(\Theta) = \frac{2d}{\cos\Theta} \ .$$

Therefore the average path L is

$$L = \int_0^{\pi/2} 2\cos\Theta \, \frac{2d}{\cos\Theta} \sin\Theta \, d\Theta = 4d .$$

When, following McMillan, we write $L=2dB$, we may immediately see that $B=2$. However, the calculation is still valid, if instead of assumption (b) we assume that the electron is reflected at the back face of the film according to the cosine law. Therefore we may conclude that $B=2$ as long as assumptions (a) and (c) are obeyed and the reflection at the back face of the film is a mixture of specular and diffuse reflection.

# APPENDIX II

## THE CALCULATION OF THE CRITICAL TEMPERATURE OF THE McMILLAN MODEL

The method for calculation of the critical temperature of the proximity sandwich, as suggested by Mr. R. Teshima, is described. The method utilizes the fact that $\Delta_S^{ph}$ goes to zero when T goes to $T_C$. First, new variables x, y, and $\gamma$ are defined by equations

$$\begin{aligned} \Delta_S &= x\Delta_S^{ph}, \\ \Delta_N &= y\Delta_N^{ph}, \\ \Delta_N^{ph} &= \gamma\Delta_S^{ph}. \end{aligned} \tag{A.II.1}$$

The new variables are introduced into eqs. III.1 and the equations are evaluated in the limit $\Delta_S^{ph} \to 0$, giving

$$\begin{aligned} x\left(1 + \frac{i\Gamma_S}{E}\right) - y\,\frac{i\Gamma_S}{E} &= 1, \\ x\,\frac{i\Gamma_N}{E} - y\left(1 + \frac{i\Gamma_N}{E}\right) &= -\gamma. \end{aligned} \tag{A.II.2}$$

A similar procedure is applied to eqs III.2, giving

$$\gamma = \lambda_N \int_0^{\omega_c^N} \mathrm{Re}\left(\frac{y}{E}\right) \tanh\frac{E}{2T}\, dE, \tag{A.II.3}$$

$$1 = \lambda_S \int_0^{\omega_c^S} \mathrm{Re}\left(\frac{x}{E}\right) \tanh \frac{E}{2T}\, dE. \qquad \text{A.II.3}$$

Eqs.A.II.2can be solved for x and y and the results put into eqs.A.II.3 ,giving

$$\gamma = \lambda_N \int_0^{\omega_c^N} \frac{\gamma E^2+(\Gamma_N + \gamma\Gamma_S)\ (\Gamma_N + \Gamma_S)}{E^2 + (\Gamma_N + \Gamma_S)^2} \tanh \frac{E}{2T}\, dE,$$

$$\text{A.II.4}$$

$$1 = \lambda_S \int_0^{\omega_c^S} \frac{E^2+ (\Gamma_N + \gamma\Gamma_S)\ (\Gamma_N + \Gamma_S)}{E^2 + (\Gamma_N + \Gamma_S)^2} \tanh \frac{E}{2T}\, dE.$$

When $\gamma$ is eliminated from eqs.A.II.4 we get the final result

$$F \equiv \frac{\lambda_N\lambda_S\Gamma_N\Gamma_S I_1 I_3}{1 - \lambda_N I_2/(\Gamma_N+\Gamma_S) - \lambda_N\Gamma_S I_1} + \frac{\lambda_S I_4}{\Gamma_N+\Gamma_S} + \lambda_S\Gamma_N I_3 - 1 = 0 \qquad \text{A.II.5}$$

where

$$I_1 = \int_0^{\omega_c^N} D(E)\ dE, \qquad I_2 = \int_0^{\omega_c^N} E^2 D(E)\ dE,$$

$$I_3 = \int_0^{\omega_c^S} D(E)\ dE, \qquad I_4 = \int_0^{\omega_c^S} E^2 D(E)\ dE,$$

and

$$D(E) = \frac{\Gamma_N + \Gamma_S}{E^2+ (\Gamma_N + \Gamma_S)^2}\ \frac{1}{E} \tanh \frac{E}{2T}\ .$$

The temperature for which $F = 0$ is the critical temperature of the McMillan model. The equation $F = 0$ has more than one solution. The root of physical interest is selected from the temperature interval 1.2°K to 3.8°K.

# APPENDIX III

## GLOW DISCHARGE OXIDATION OF FRESHLY EVAPORATED ALUMINUM FILMS

### Introduction

A discussion is presented of glow discharge assisted oxide growth on the surface of freshly evaporated aluminum films at 14°C with special attention to the preparation of tunnel junctions. The mass gain of the aluminum film during the oxidation was measured with a quartz crystal microbalance and recorded as a function of time.

The rate of mass gain cannot be described by a single oxidation law covering the whole period of oxidation. The oxidation rate was found to depend only on the total current through the glow discharge; the applied voltage and oxygen pressure were not important.

### Experimental

The vacuum apparatus was a standard system used for preparation of thin film tunnel junctions (three stage oil diffusion pump with diameter of 4 inches with a liquid nitrogen trap backed by a mechanical pump). Before the evaporation, the vacuum reached 1 x $10^{-7}$ Torr and was kept in the range of $10^{-6}$ Torr during the evaporation.

The quartz crystal microbalance consisted of two 5 MHz quartz crystals mounted in the same water-cooled copper holder.

One crystal was directly exposed to evaporated material and the surrounding oxidizing atmosphere, the other was in thermal contact with the copper holder only. The change of beat frequency, which arose from mass deposition onto the exposed crystal, was recorded. The mass sensitivity was 0.02 $\mu g/cm^2$ Hz. The drift of the system was about 2 Hz per hour after an initial warm-up period.

A film of aluminum about 300 Å thick (99.999% purity) was evaporated onto the surface of the quartz crystal from a tungsten coil at a distance of about 45 cm. A few minutes after the deposition was completed, commercial grade oxygen purified by passing through a coil immersed in liquid nitrogen, was admitted to the system at various pressures ranging from 0.02 to 0.2 Torr.

A glow discharge was initiated in accordance with Miles and Smith by applying a negative d.c. potential to an aluminum electrode. The metallic part of the evaporator served as the ground electrode. Current I flowing through the negative glow electrode was measured and its value controlled either by varying the applied potential or oxygen pressure in the evaporator.

The negative glow electrode consisted of two straight pieces of aluminum wire about 3 in long and 5 in apart. They were connected together and brought to the vacuum feed-through by a wire surrounded with 10 mm glass tubing in order to restrict the discharge to the aluminum wires only. The position and the shape of the glow electrode were chosen to produce an oxide film with uniform thickness over an area of 1 x 3 $in^2$. This was the size of microscope slide on which three tunneling junctions were prepared at the same time. It was assumed that uniformity of the tunneling resistance of the oxide implies uniformity of the oxide thickness. First, it was found experimentally that the tunneling resistance of an oxide film formed in a glow discharge depends approximately on $r^{-3/2}$ where r is the radial distance from a single straight electrode. Secondly, two such electrodes were combined to produce uniform oxide over the desired area. The quartz crystal microbalance was placed in an asymmetrical position about 12 cm above one electrode. The actual oxidation rate depends on the exact geometry of the ground electrode and it was found to be different in different evaporation systems.

Tiny sparks that sometimes appear on the glow electrode may produce pinholes in the oxide and certainly introduce irreproducibility in tunnel junction preparation. It is therefore necessary to clean the electrode prior to the actual oxidation. This may be accomplished when the system is being evacuated for the first time by maintaining a glow discharge with a higher voltage than planned for the actual oxidation, until all sparks disappear. In this process, all dust particles and surface irregularities which may form sharp points on the surface of the electrode are burned off. Sometimes, when aluminum wires of low purity are used, the sparking cannot be avoided.

## Results and discussion

Typical oxide growth characteristics are shown in Fig. A.III.1. The change of crystal frequency (counting was started after the evaporation of the aluminum film was completed) is plotted vs time for glow discharge oxidation at an applied voltage of 900 volts and current of 3.5 mA through the glow electrode. There are three stages of glow discharge oxidation visible in Fig. A.III.1.

1) When the system was filled with dry oxygen (at time $t_1$) the frequency of the crystal increased about $\Delta f_o$ ($\Delta f_o$ is usually from 4 to 6 Hz). This process was usually completed within 50 sec. This change did not disappear when the system was again pumped to high vacuum but it was then stable in time. It was concluded that the frequency jump $\Delta f_o$ corresponds to a formation of aluminum oxide with its limiting thickness, as discussed by Mott (1939,1940,1947), Mott and Cabrera (1949), Fromhold and Cook (1967), and Hart (1956). To convert mass gain data per unit area to change in oxide film thickness, we note according to Dignam et al. (1966) that a mass gain of 1 $\mu g/cm^2$ corresponds to an increase of oxide thickness of 66.4 Å. Therefore a frequency change of 5 Hz corresponds to 0.1 $\mu g/cm^2$ or 7 Å of aluminum oxide. This seems to be a bit too low for the saturated thickness of aluminum oxide (which is usually about 25 Å) but oxide formation on the surface of very thin evaporated films in dry oxygen is probably different from that on bulk aluminum.

FIG. A.III.1

The change of the crystal frequency ( left hand scale ) or corresponding mass gain ( right hand scale ) plotted vs time ( glow discharge oxidation at I = 3.5 mA ).

○ experimental points,

——— least squares fit to generalized Mott-Cabrera law,

------- linear law fit .

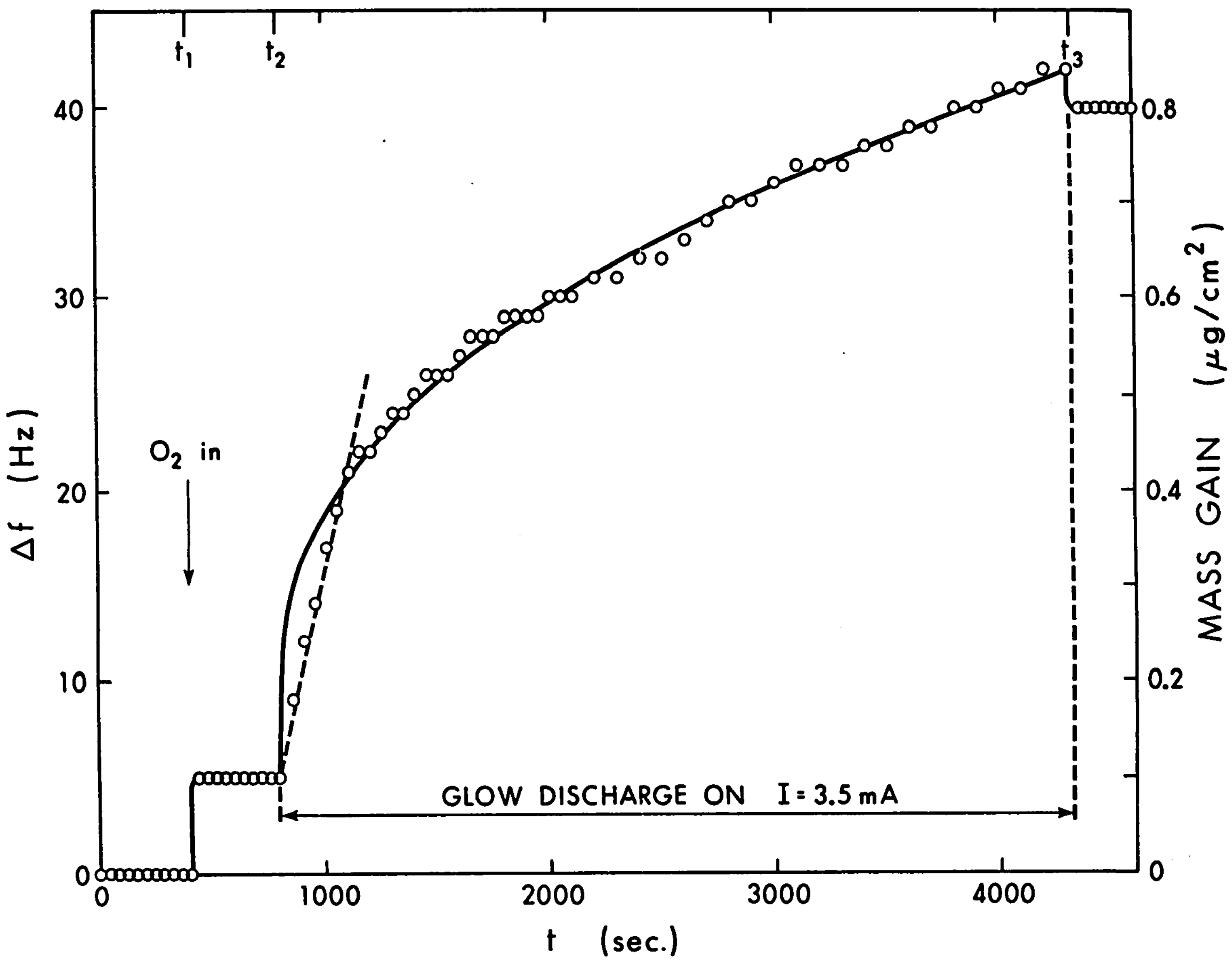

t1
t2
t3
$O_2$ in
GLOW DISCHARGE ON I = 3.5 mA
Δf (Hz)
0
10
20
30
40
t (sec.)
0
1000
2000
3000
4000
MASS GAIN (μg/cm²)
0
0.2
0.4
0.6
0.8

2) When the glow discharge was switched on (at the time $t_2$) the frequency steadily increased with time (which represents the forced growth of the aluminum oxide). This stage is discussed later on in more detail.

3) When the glow discharge was switched off (at the time $t_3$) the frequency usually dropped about 2 Hz. This stage probably corresponds to the outgassing of the loosely bound or physically adsorbed oxygen molecules from the surface. When the system was again pumped to high vacuum, the frequency of the crystal microbalance remained unchanged.

The oxide thickness that produced an Al-$Al_2O_3$-Sn tunnel junction with a resistance of 100Ω was estimated to be about 27 Å or about 0.4 μg/cm$^2$ of mass gain. Using the known time for the junction preparation, the geometrical factor was employed to calculate the corrected time at the position of the crystal and the oxide thickness was read from the corresponding mass gain vs time plot. One has to remember that the oxide thickness of 27 Å is reduced as the top electrode is evaporated and the metal ions penetrate the oxide.

As the aluminum oxide grows, aluminum ions must traverse the oxide film to the oxide-oxygen interface (ionic current) and simultaneously electrons must be transferred through the oxide (electronic current) to account for the change of the charge. It is assumed, that in the present case, the ionic current is rate limiting and that we can write for the rate of growth according to Cabrera and Mott (1949), Fromhold and

Cook (1967), and Dignam et al. (1966)

$$\frac{dX}{dt} = 2A \sinh(\frac{\mu E}{kT}) \quad , \quad A = \Omega \nu \; a \; n \; e^{-\frac{w}{kT}} \; ,$$

where X is the oxide film thickness at time t, $\Omega$ is the volume of oxide per one ion, n is the concentration of mobile ions, $\nu$ is the ionic attempt frequency, a is the ionic jump distance, w is either the metal-oxide interface barrier or barrier inside the oxide film (whichever is bigger), $\mu$ is the ionic jump distance times effective charge and E is the electric field in the oxide. We may derive two limiting laws of growth.

1) When E = C, where C is constant, we obtain a linear law of growth

$$X + X_o = 2A \; t \; \sinh \; (\frac{\mu C}{kT}) . \qquad \text{A.III.1}$$

2) When the potential V = EX across the film is constant, we may write according to Fromhold and Cook (1967), and Dignam et al. (1966)

$$\frac{dx}{dt} = 2A \sinh \; (\frac{B}{X}) \quad , \quad B = \frac{\mu EX}{kT} = \frac{\mu V}{kT}$$

$$\text{and} \quad \int_{B/X}^{B/X_o} \frac{dz}{2z^2 \sinh z} = 2At \quad , \qquad \text{A.III.2}$$

where $X_o$ is the oxide thickness at time t = 0. Eq. A.III. 2 is called the generalized Mott-Cabrera law.

In general, neither E nor V are constants. For thermal oxidation, V is normally considered to be the initial difference between the metal Fermi level and the oxygen $O^-$

level (see e.g. Fromhold and Cook (1967)). However, in our case, V also includes the effect of the glow discharge.

A linear plot of mass gain vs time (circles) is shown in Fig. A.III.1 for typical oxidation at constant current, $I = 3.5$ mA. The solid line represents a least squares fit of the data to Eq. A.III.2 (fitted by IBM computer).The fit is quite good for $t - t_2 \gtrsim 300$ sec (or for thickness greater than 27 Å). For $t - t_2 < 300$ a linear law fits the data best. In terms of eqs.A.III.1 and A.III.2 it appears that in the initial stage of a glow discharge oxidation performed at constant current there is a rather constant electric field in the oxide. That is, as the oxide thickness increases, the potential drop across it must increase. The later oxidation stage, $t - t_2 \gtrsim 300$ sec, which fits the generalized Mott-Cabrera law quite well is characterized by a constant potential V across the oxide film.

From the least squares fit of data to eq. A.III.2 we have found for the later oxidation stage at 14°C and $I = 1$ mA the values, $B = 29.2$ Å and $A = 3.13 \times 10^{-3}$ Å $\text{sec}^{-1}$, and for $I = 3.5$ mA, $B = 68.1$ Å and $A = 1.80 \times 10^{-3}$ Å $\text{sec}^{-1}$. These values of B lead to $\mu V = 0.72$ eÅV for $I = 1$ mA and $\mu V = 1.69$ eÅV for $I = 3.5$ mA. Because $\mu$ is connected with the oxide structure and should be about the same in both cases we see that the total current I through the glow discharge affects the potential across the growing oxide film. We may compare our results with the high temperature oxidation data of Dignam et al. (1966) extrapolated to 14°C, which yield $\mu V = 8.2$ eÅV and $A = 2.2 \times 10^{-22}$ Å $\text{sec}^{-1}$. The differences indicate a substantial difference of oxide structure for glow discharge oxidation and thermal oxidation. There is of course some question about whether conclusions based on high temperature oxidation can be extrapolated to low temperature and whether the rate limiting process (barriers inside oxide or in metal-oxide interface) remains the same.

In Fig. A.III.2 the oxidation data for different runs are plotted so that a parabolic relationship $x^2 \propto (t - t_2)$ would give a straight line. It may be seen that a parabolic law (dashed line) fits the data over a more limited range than does Eq. A.III.2 (solid line).

In Fig. A.III.3 the data are plotted in accord with the direct logarithmic law $x \propto \log (t - t_2)$. The fit is quite good for $t - t_2 \leq 1700$ sec (thickness < 43 Å), but for longer oxidation times experimental data deviate from logarithmic law. The logarithmical law fits the data in the range suitable for the preparation of good tunnel junctions, therefore one can expect approximately a linear relationship between the junction resistivity and oxidation time.

A very important feature of glow discharge oxidation is illustrated in Fig. A.III.2. The oxide thickness at any time depends only on the total current I through the glow discharge and is independent of the way it is controlled. The glow discharge produces the same thickness of aluminum oxide at a low pressure of oxygen and high applied voltage as at high pressure of oxygen and low applied voltage as long as the

FIG. A.III.2

The change of the crystal frequency vs time for different oxidation runs plotted in terms of parabolic law. ● represents the oxidation when I = 3.5 mA, constant applied voltage is 900 V and I is kept constant by varying pressure of dry $O_2$ from 0.1 Torr to 0.2 Torr; ○ represents the oxidation when I = 3.25 mA, constant pressure of dry $O_2$ is 0.11 Torr and I is kept constant by varying voltage from 800 V to 1450 V. Similarly △ represents the oxidation when I = 1 mA, constant applied voltage is 900 V and I kept constant by changing the pressure from 0.03 Torr to 0.1 Torr, and □ is oxidation when I = mA, constant pressure of dry $O_2$ is 0.08 Torr and I kept constant by varying voltage from 600 V to 800 V.

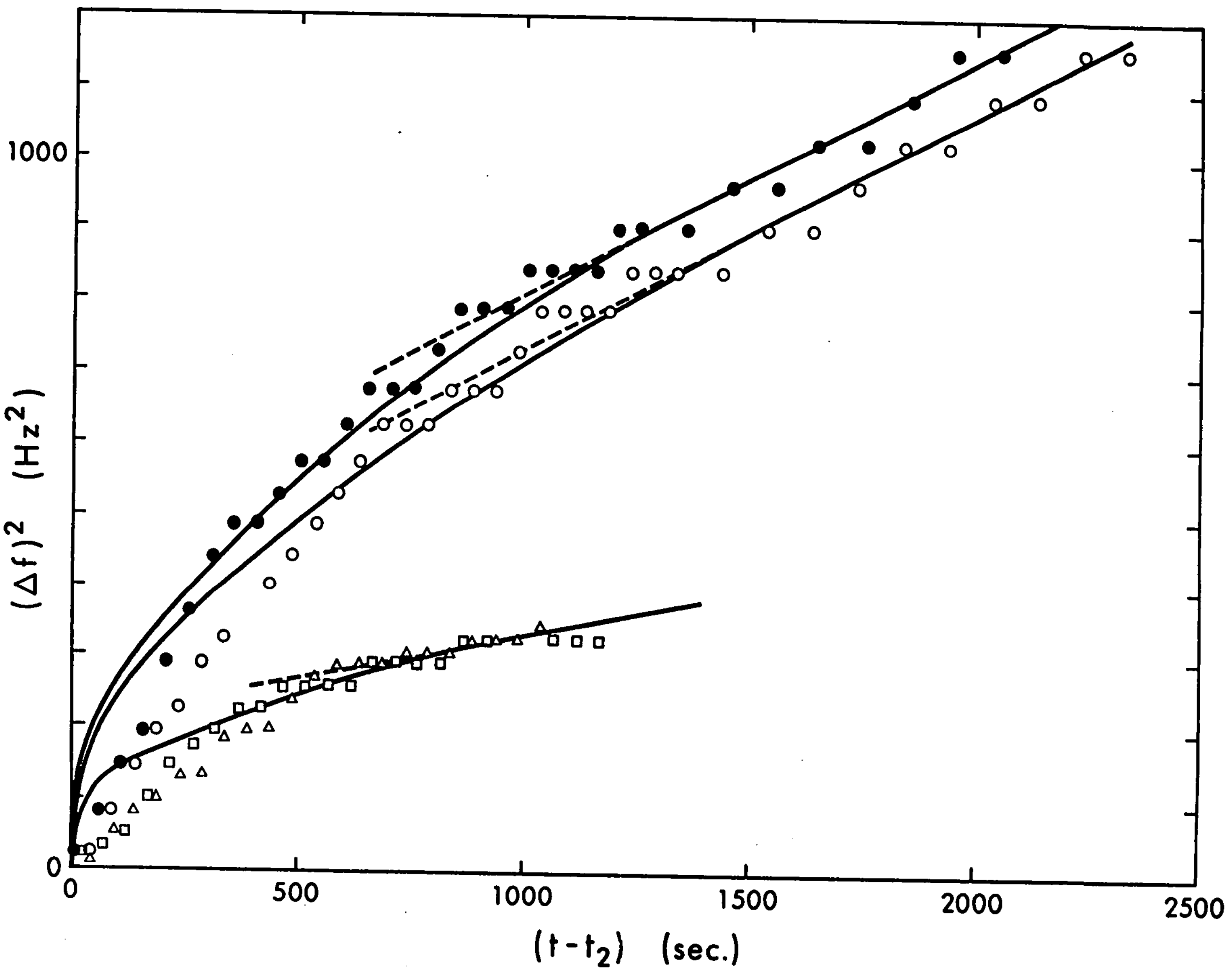
1000
0
$(\Delta f)^2$ $(Hz^2)$
0
500
1000
1500
2000
2500
$(t-t_2)$ (sec.)

FIG. A.III.3

The crystal frequency vs logarithm of time for the oxidation run with I = 3.5. mA.

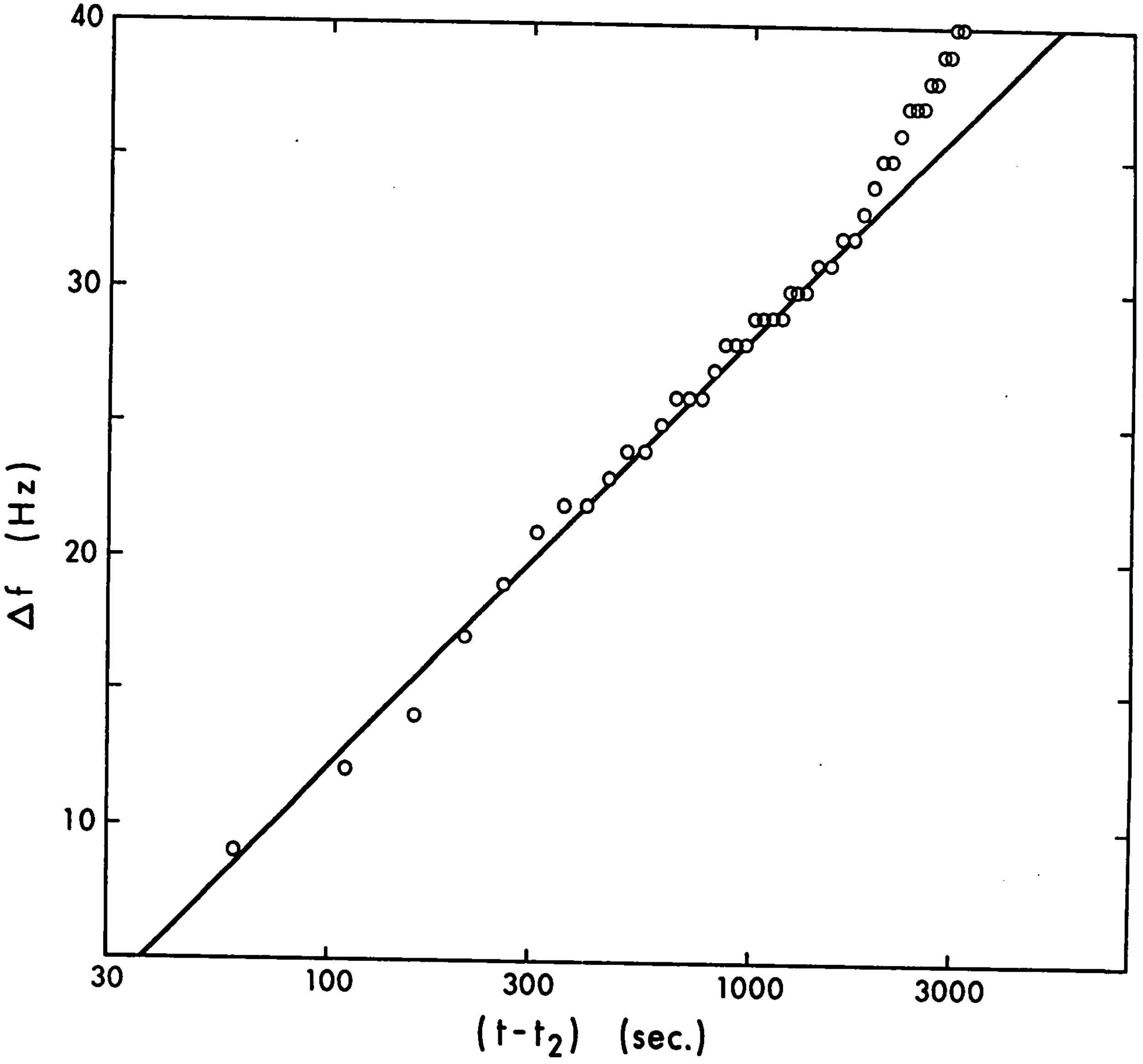
40
30
20
10
Δf (Hz)
30
100
300
1000
3000
(t-t₂) (sec.)

current I is the same. No maximum in the oxidation rate at a pressure of 0.05 Torr as reported by Miles and Smith (1963a) was found.

## Conclusion

Oxidation of thin evaporated aluminum films has been studied. The time dependence of the oxide growth does not conform to a generalized Mott-Cabrera law, a parabolical law, or a logarithmic law over a broad time range. We may conclude from fitting the generalized Mott -Cabrera law, that in the first stage of glow discharge oxidation the potential across the oxide film is growing, keeping the electrical field in the oxide approximately constant and giving a linear law of oxidation, while in the advanced stage of oxidation, the potential across the film is constant, leading to the Mott-Cabrera oxidation law.

The oxidation rate was found to depend only on the total current through the glow discharge.

# APPENDIX IV

## THE EVALUATION OF THICKNESS FROM THE INTERFERENCE FRINGES

The interference fringes are photographed and their spacings on the film are measured using an optical densitometer. The optical system of the densitometer is focussed into a sharp spot ( the size is smaller than the width of a fringe),over which the intensity of the light passing through the film may be recorded. The photograph of the fringes is placed on a two-dimensionally movable table in the focal plane of the optical system, and the steps in the fringes that correspond to the edge of the thickness change are adjusted so that a line through them would be as nearly as possible parallel to one direction of the table motion. The positions of the fringes on both sides of the steps are recorded and the thickness calculated from them.

A reference frame may be defined by the steps and by one of the fringes. However, the fringes are never perpendicular to the line of the steps and the photograph is never placed on the table of the optical densitometer with the fringes exactly perpendicular to one direction of the table motion. Thus an error that depends linearly on the measuring distance from the steps is introduced.

A method which eliminates this error was designed and is described below.

To eliminate the error, we draw onto the photograph equally spaced lines ( called simply "the lines" ) which are approximately parallel to the steps. The line which is closest to the steps is called the X-axis. Assume for a moment, that X can be placed exactly parallel to the direction of the motion of the table of the optical densitometer. See Fig.A.IV.1.a. The perpendicular distance between the lines is a, the angle between the fringes and X-axis is $\alpha$, the perpendicular distance between two fringes is $\ell$, the perpendicular height of the step at the edge of the thickness change is $\Delta$, and $\Delta'$ and $\ell'$ are the same as $\Delta$ and $\ell$ but the distances are measured in the direction parallel to X. It is obvious, that $\frac{\Delta}{\ell} = \frac{\Delta'}{\ell'}$ , therefore the thickness $d = (\lambda/2)(\Delta/\ell)$ does not depend on the direction along which we measure the distances. The numbers $A_{n1}$, $A_{n2}$, ... $A_{nN}$ denote the X coordinates of the intercepts of the fringes with the line which intercepts the Y axis at the point na, and N is the total number of fringes. The intercepts of the fringes with the lines which cross the negative Y axis are labeled by the symbol B. Therefore from measurement we get the following two sets of data

$$\underset{\sim}{A}_1 = A_{11}, \; A_{12}, \; A_{13}, \; \ldots \; A_{1N}$$
$$\underset{\sim}{A}_2 = A_{21}, \; A_{22}, \; A_{23}, \; \ldots \; A_{2N}$$
$$\vdots$$

FIG. A.IV.1

( a ) The geometry of interference fringes ,

( b ) The effect of "off perpendicular" measurement.

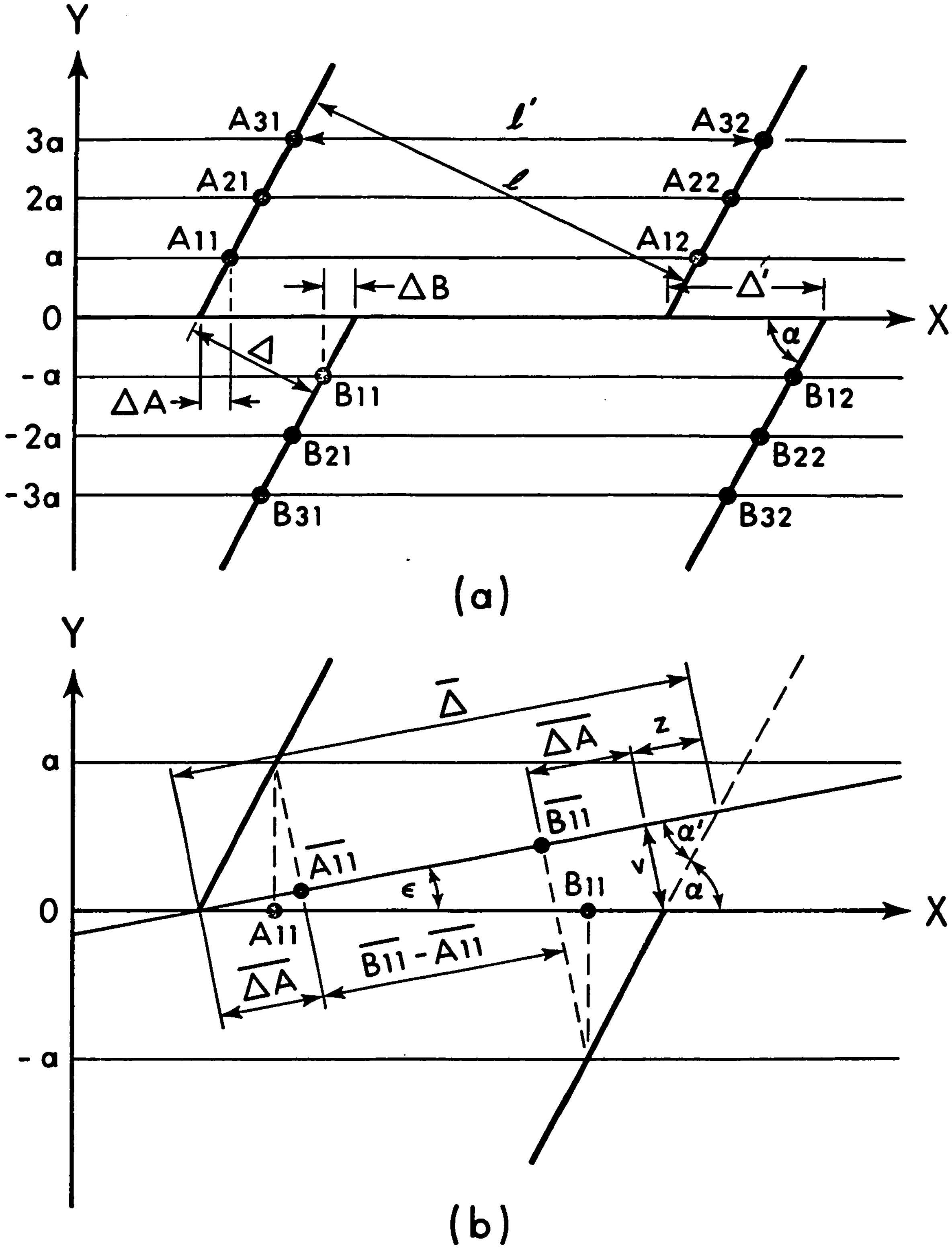
Y
X
3a
2a
a
0
-a
-2a
-3a
A31
A21
A11
A32
A22
A12
B11
B21
B31
B12
B22
B32
ℓ'
ℓ
ΔB
Δ'
Δ
ΔA
α
(a)
Y
X
a
0
-a
$\overline{\Delta}$
$\overline{\Delta A}$
z
$\overline{B11}$
$\overline{A11}$
α'
α
v
ε
A11
B11
$\overline{B11}-\overline{A11}$
$\overline{\Delta A}$
(b)

$$\underset{\sim}{A}_K = A_{K1},\quad A_{K2},\quad A_{K3},\ \ldots\ A_{KN}$$

$$\begin{aligned}
\underset{\sim}{B}_1 &= B_{11},\quad B_{12},\quad B_{13},\ \ldots\ B_{1N} \\
\underset{\sim}{B}_2 &= B_{21},\quad B_{22},\quad B_{23},\ \ldots\ B_{2N} \\
&\vdots \\
\underset{\sim}{B}_L &= B_{L1},\quad B_{L2},\quad B_{L3},\ \ldots\ B_{LN}
\end{aligned} \qquad \text{A.IV.1}$$

where $K$ is the number of lines which are drawn in the $Y>0$ space and $L$ is the same in $Y<0$ space. ( In Fig. A.IV.1.a $K = L = 3$ ).

Now the averaging procedure for $\Delta'$ and $\ell'$ in terms of A's and B's will be described. First we define the vectors

$$\begin{aligned}
\Delta\underset{\sim}{A}_k &= \underset{\sim}{A}_{k+1} - \underset{\sim}{A}_k\,, \\
\Delta\underset{\sim}{B}_\ell &= \underset{\sim}{B}_\ell - \underset{\sim}{B}_{\ell+1}
\end{aligned} \qquad \text{A.IV.2}$$

where $k = 1,2,\ \ldots\ K-1$ and $\ell = 1,2,\ \ldots\ L-1$. When the vectors $\underset{\sim}{A}_k$ and $\underset{\sim}{B}_\ell$ are averaged over $k$ and $\ell$ (it means averaging each component over the appropriate fringe) we get new vectors

$$\begin{aligned}
\Delta\underset{\sim}{A} &= \frac{1}{K-1}\sum_{k=1}^{K-1} \Delta\underset{\sim}{A}_k\,, \\
\Delta\underset{\sim}{B} &= \frac{1}{L-1}\sum_{\ell=1}^{L-1} \Delta\underset{\sim}{B}_\ell\,.
\end{aligned} \qquad \text{A.IV.3}$$

In the ideal case ( no scatter in the data set A.IV.1 ) all components of vectors $\Delta\underset{\sim}{A}$ and $\Delta\underset{\sim}{B}$ are equal. If such a component is denoted $\Delta A$, we can calculate the angle $\alpha$ from the expression

$$\mathrm{tg}\alpha = \frac{a}{\Delta A} \,. \tag{A.IV.4}$$

We may define the vectors

$$\underset{\sim}{\Delta}'_j = \underset{\sim}{B}_j - \underset{\sim}{A}_j + j\,(\Delta\underset{\sim}{A} + \Delta\underset{\sim}{B}), \tag{A.IV.5}$$

where $j = 1, 2, \ldots M$, and $M = \min(K, L)$. When the vectors $\underset{\sim}{\Delta}'_j$ are averaged over $j$, we get

$$\underset{\sim}{\Delta}' = \frac{1}{M}\sum_{j=1}^{M}\underset{\sim}{\Delta}'_j \,. \tag{A.IV.6}$$

In the ideal case ( no scatter in the data set A.IV.1 ) all components of vector $\underset{\sim}{\Delta}'$ are equal to $\Delta'$.

To calculate $\ell'$, we form a vectors $\underset{\sim}{\ell}^A_k$ and $\underset{\sim}{\ell}^B_\ell$ , which components are defined by

$$\begin{aligned} \ell^A_{k,n} &= A_{k,n+1} - A_{k,n} \,, \\ \ell^B_{\ell,m} &= B_{\ell,m+1} - B_{\ell,m} \,, \end{aligned} \tag{A.IV.7}$$

where $m, n = 1, 2, \ldots N - 1$. Averaging over $k$ and $\ell$, and both together we get the vector

$$\underset{\sim}{\ell}' = \frac{1}{2}\left( \frac{\sum\limits_{k=1}^{K-1} \underset{\sim}{\ell}^A_k}{K-1} + \frac{\sum\limits_{\ell=1}^{L-1} \underset{\sim}{\ell}^B_\ell}{L-1} \right) . \tag{A.IV.8}$$

Again, in the ideal case each component of $\underset{\sim}{\ell}'$ is equal to $\ell'$. Now we form the vector $\underset{\sim}{\frac{\Delta'}{\ell'}}$ by division of each component of $\underset{\sim}{\Delta}'$ by corresponding component $\underset{\sim}{\ell}'$. Averaging over the components of the vector $\underset{\sim}{\Delta'/\ell'}$ we get the final answer

$$\frac{\Delta}{\ell} \equiv \frac{\Delta'}{\ell'} = \frac{1}{N-1} \sum_{i=1}^{N-1} \frac{\Delta_i'}{\ell_i'} \, . \qquad \text{A.IV.9}$$

The above described method for calculation of $\frac{\Delta}{\ell}$ was programmed together with its standard deviation for the IBM/360 time sharing system using APL/360 language ( Falkoff and Iverson (1968)).

Now it will be shown, that when the photograph is placed with X-axis at an angle $\varepsilon$ to the direction of the motion of the table of optical densitometer, the results are not affected. For simplicity the calculation is done only for one line drawn in each half plane $Y>0$ and $Y<0$ and for one fringe. The situation is shown in Fig.A.IV.1.b. The quantities which are read when the angle $\varepsilon$ is introduced are denoted with a bar. By elementary geometrical considerations, the following expressions may be derived

$$\begin{aligned} \bar{\Delta} &= (\bar{B}_1 - \bar{A}_1 + 2\overline{\Delta A})\left(1 + \frac{tg\varepsilon}{tg\alpha'}\right), \\ \bar{\ell} &= (\bar{A}_2 - \bar{A}_1)\left(1 + \frac{tg\varepsilon}{tg\alpha'}\right) = (\bar{B}_2 - \bar{B}_1)\left(1 + \frac{tg\varepsilon}{tg\alpha'}\right), \end{aligned} \qquad \text{A.IV.10}$$

where $\alpha' = \alpha - \varepsilon$ and the meaning of the other symbols is obvious from the Fig.A.IV.1.b. One can see from eq.A.IV.10 that the ratio $\frac{\bar{\Delta}}{\ell}$ is independent of angle $\varepsilon$.

When the lines are not equally spaced, the resulting error $\delta d$ in the calculated thickness d is of the order of

$$\delta d \simeq 2730 \frac{\delta a}{\ell \mathrm{tg}\alpha} ,$$

where $\delta a$ is the variation in the spacing of the lines, $\ell$ is usually about 10 mm and $\alpha$ is within 10° around 90° ( which is easy to adjust ). If e.g. the maximum allowed error $\delta d$ is about 5Å, we may estimate $\delta a \simeq 0.5$ mm. Such an error is very unlikely because the parallel lines are separated about 5 mm and are drawn through a rigid mask which is machined from 1/16 inch brass plate.

# APPENDIX V

## THE CIRCUIT DIAGRAM OF THE QUARTZ CRYSTAL MONITOR

The 5 MHz quartz crystals are driven by two identical transistor oscillators, shown in Fig.A.V.1. The transistors T3 and T6 act as impedance transformers. Both oscillators are mounted inside the high vacuum jacket and the high frequency from both is brought out on one wire together with the d.c. power.

A circuit diagram of the mixer and filter is shown in Fig.A.V.2.a. Transistor T7 acts as a mixer and detector. Transistor T8 acts as a buffer separating the active filter A1 from the mixing circuit. The filter does not pass frequencies higher than 250 kHz.

The final amplifier A2 is shown in Fig.A.V.2.b. The output beat frequency is connected to the input of a digital frequency counter ( 5214L Preset Counter, Hewlett Packard ).

FIG. A.V.1

Oscillators for quartz crystal monitor which are mounted inside vacuum space. All transistors are International Rectifier, TR 20-C.

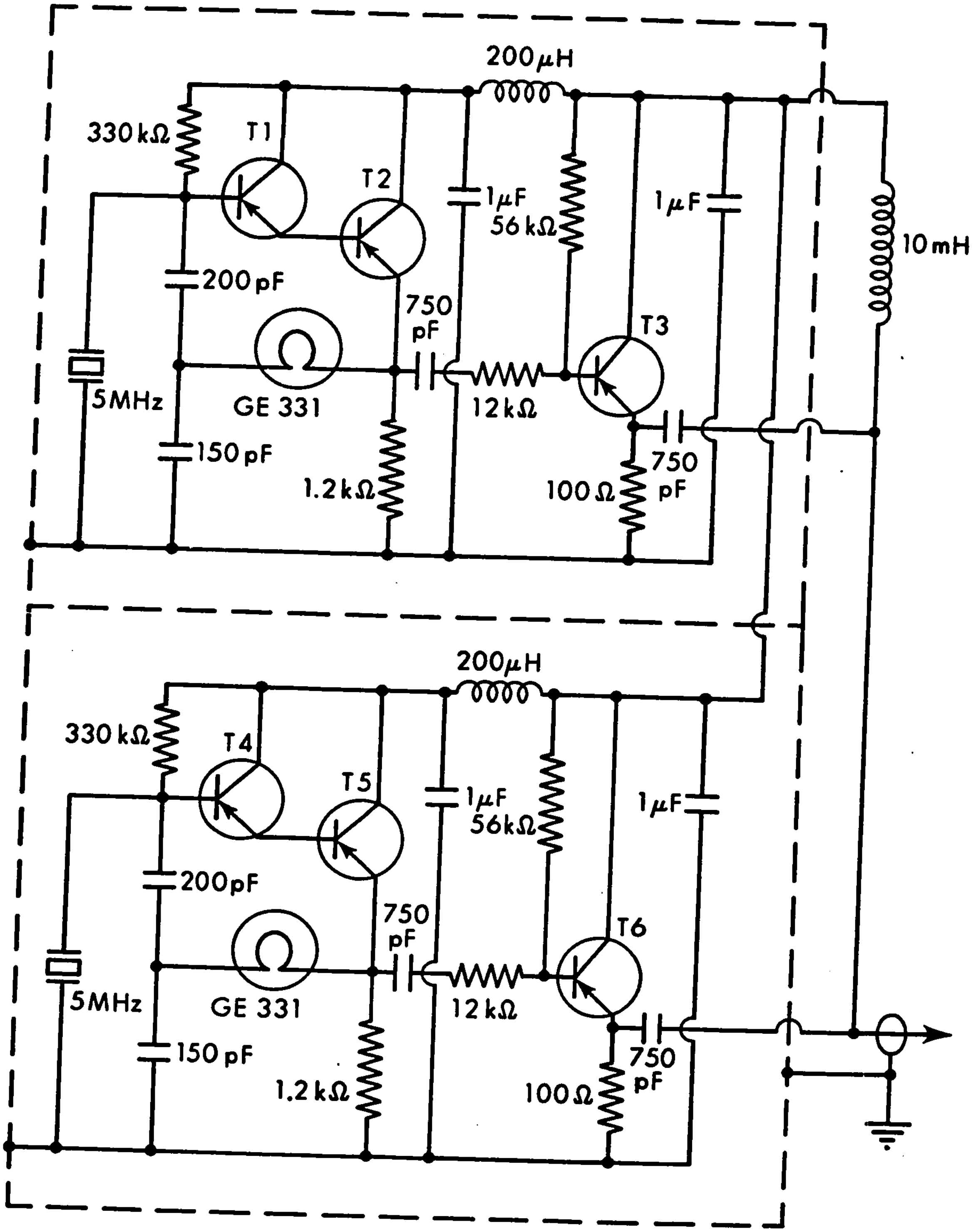
200μH
330kΩ
T1
T2
1μF
56kΩ
1μF
10mH
200pF
750 pF
T3
5MHz
GE 331
12kΩ
150pF
1.2kΩ
100Ω
750 pF
200μH
330kΩ
T4
T5
1μF
56kΩ
1μF
200pF
750 pF
T6
5MHz
GE 331
12kΩ
150pF
1.2kΩ
100Ω
750 pF

FIG. A.V.2

(a) Mixing, detecting and filtering circuit for extraction of beat frequency from two quartz crystal oscillators.

(b) Output amplifier for frequency counter.

All transistors are of the type International Rectifier TR 20 – C; operational amplifiers are NS LM 301 A.

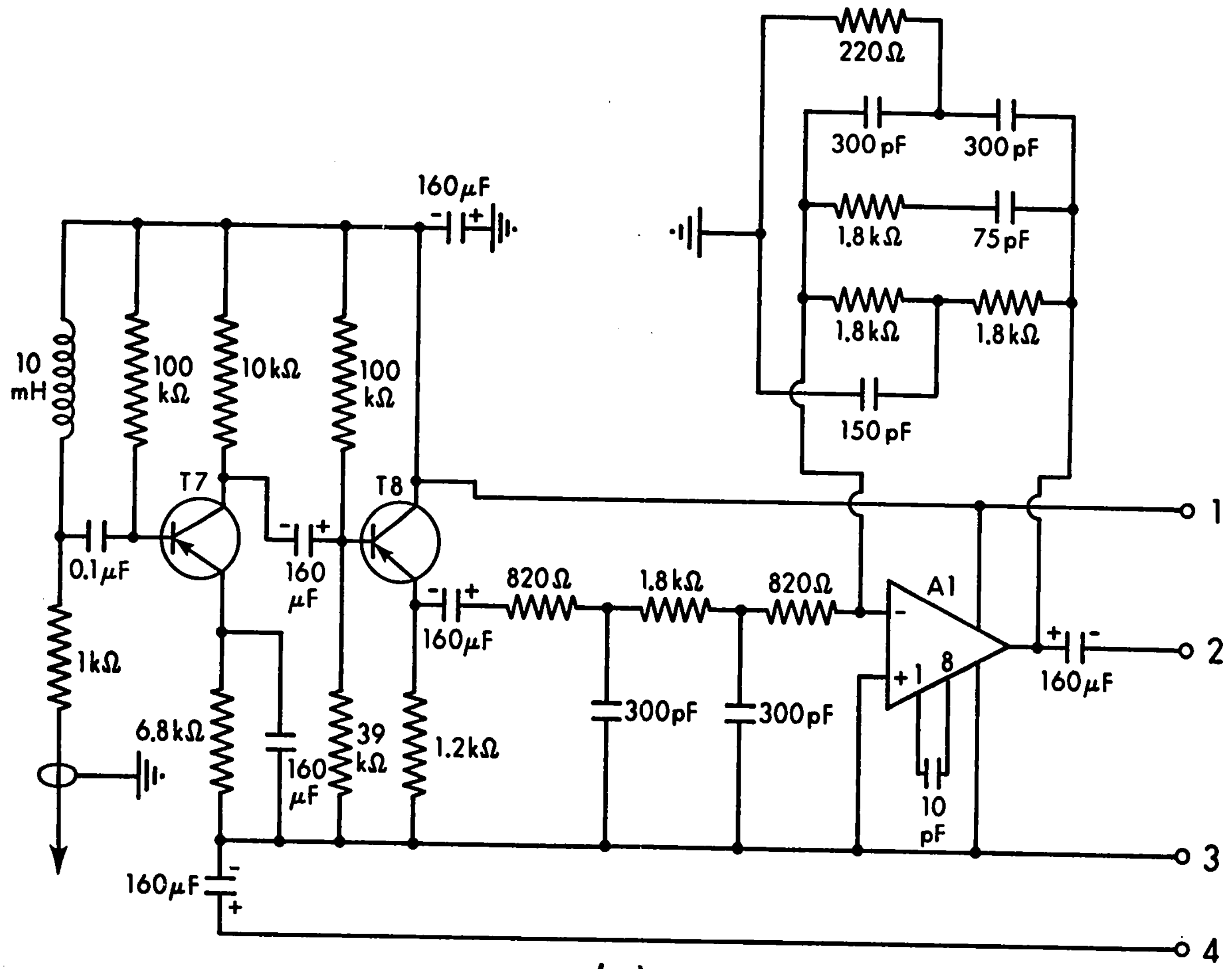

220Ω
300 pF
300 pF
1.8 kΩ
75 pF
1.8 kΩ
1.8 kΩ
150 pF
160μF
10 mH
100 kΩ
10kΩ
100 kΩ
T7
T8
0.1μF
160 μF
1kΩ
6.8kΩ
160 μF
39 kΩ
1.2kΩ
160μF
820Ω
1.8kΩ
820Ω
300pF
300pF
A1
8
1
10 pF
160μF
160μF
1
2
3
4

(a)

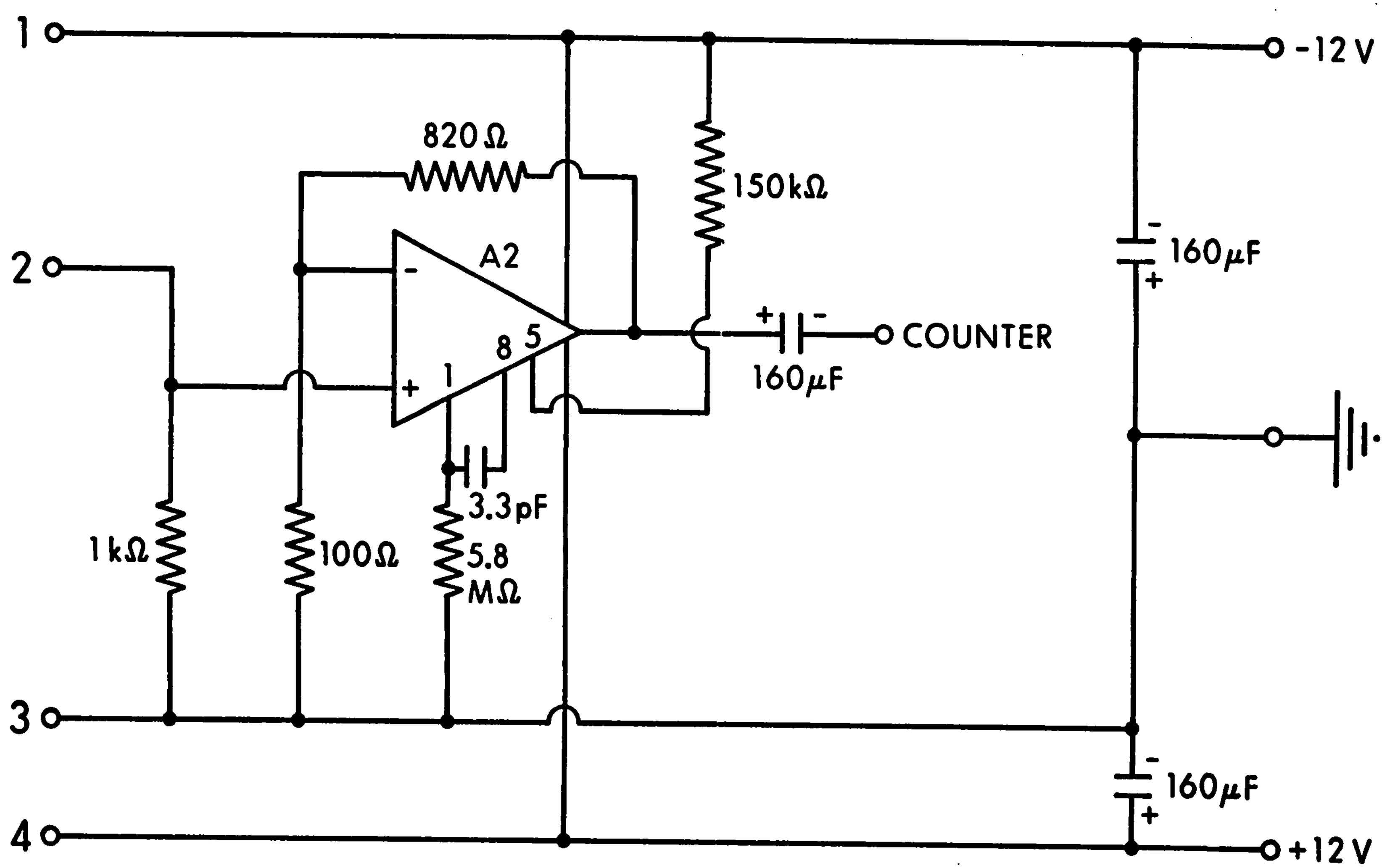
1
2
3
4
-12 V
+12 V
820 Ω
150 kΩ
A2
-
+
1
8
5
160 μF
-
+
COUNTER
3.3 pF
5.8 MΩ
1 kΩ
100 Ω
160 μF
160 μF

(b)

# APPENDIX VI

## A SIMPLE, CONTINUOUS READING LIQUID LEVEL DETECTOR

A continuous reading liquid level detector, employing the difference between the dielectric constant of gas and liquid, is described. The construction and alignment are very simple and the liquid level is read directly from a panel meter. Other authors ( Williams and Maxwell (1954), Meiboom and O'Brien (1963), Seguin and Leonard (1966), Preshkov, Vetchinkin, and Elkonin (1969), Dash and Boorse (1951), Jones (1969), and Capocci and Gugan (1967)) have described level detectors working on the same principle, but requiring expensive instrumentation or sophisticated electronics and more complicated methods for level reading.

In the present system, the change of the dielectric constant is detected by a coaxial capacitance probe which forms one arm of a capacitance bridge that is fed by a low frequency voltage. The unbalance voltage that arises from the liquid level change is amplified, rectified and read directly on a panel meter. The bridge design does not employ carefully balanced arrangements with guards because zero adjustment is provided with a d.c. voltage in the last amplification stage. The system may be used for liquid helium, for liquid nitrogen, or for other liquids by simply changing the amplification.

The level detecting probe consists of a coaxial capacitance $C_o$ of length $\ell_o = 20.5$ cm ( along which the level $\ell$ is changing ) and of the capacitance $C_s$ formed by the connections to the measuring device. The total capacitance of the probe is thus $C_3 = C_s + C_o$. The capacitor $C_o$ is formed by two stainless steel tubes of 1/4 in-diam and 3/16 in-diam separated by nylon washers (see Fig.A.VI.1) The inner tube is extended above the liquid region by a s.s. tube of 1 mm diam in order to reduce capacitance $C_s$. Small holes are drilled along the length of the probe to permit easy liquid access and prevent pressure oscillations in the probe. Rigid construction is important.

When length $\ell$ of the probe is immersed into the liquid, the capacitance increases about $\Delta C = C_o(\ell/\ell_o)(\Delta\varepsilon/\varepsilon_o)$, where $\varepsilon_o$ is the dielectric constant of the vapor and $\Delta\varepsilon$ is its difference from the liquid phase. ( For liquid helium $\Delta\varepsilon/\varepsilon_o = 0.05$, and for liquid nitrogen $\Delta\varepsilon/\varepsilon_o = 0.45$ ).

The probe together with capacitors $C_1$, $C_2$, and $C_4$ form a capacitance bridge ( see Fig. A.VI.2 ). The bridge capacitors are zero temperature coefficient units ( type TCZ, Centralab ) with values $C_1 = C_4 = 82$ pF and $C_2 = 62$pF in parallel with a 20pF air trimmer. The bridge is fed from an oscillator with a frequency of about 20kHz and a peak output voltage $E_o = 8$V. Its stability and actual frequency are not important. A simple double integrator circuit with a regenerative feedback oscillator ( Burr - Brown (1963)) is used.

FIG. A.VI.1

The level detecting capacitance probe.

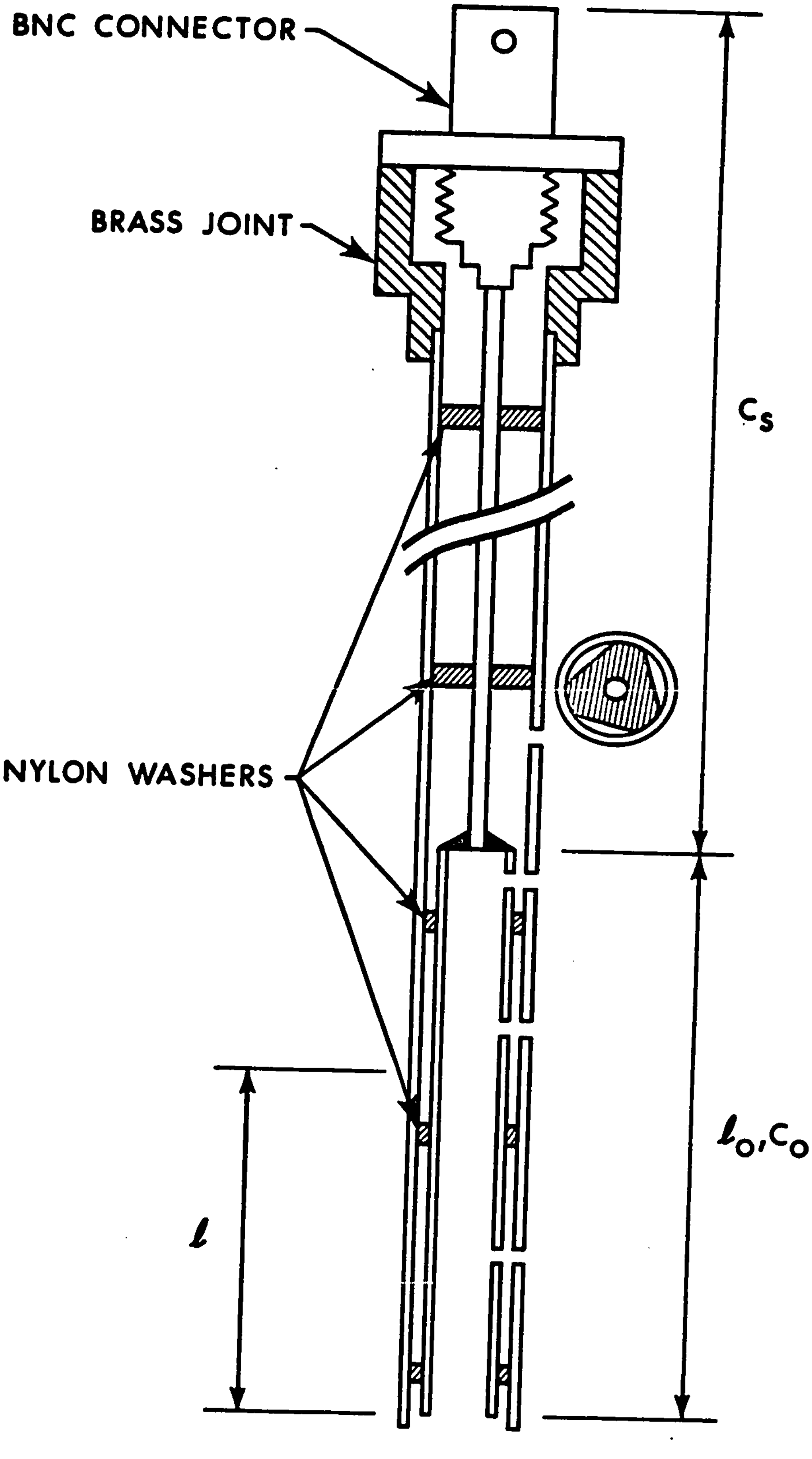
BNC CONNECTOR
BRASS JOINT
NYLON WASHERS
$C_S$
$\ell$
$\ell_0, C_0$

FIG. A.VI.2

Circuit diagram ( The capacitance bridge and differential amplifier A1 are connected to the remaining system by a long cable. )

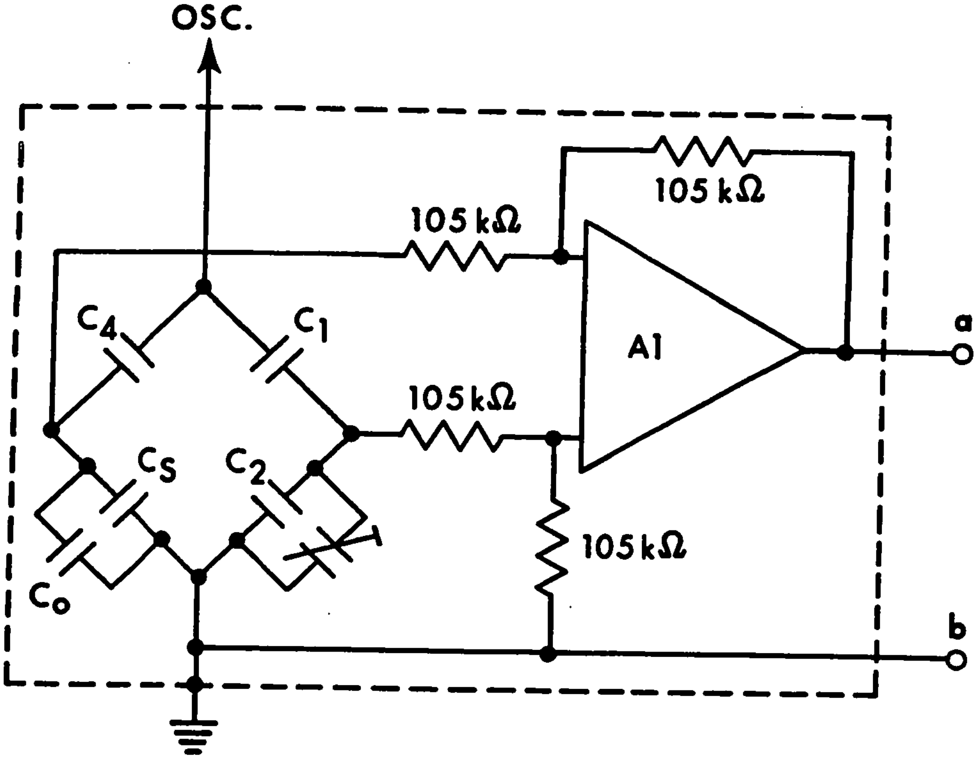
OSC.
105 kΩ
105 kΩ
C4
C1
A1
a
105 kΩ
CS
C2
105 kΩ
Co
b

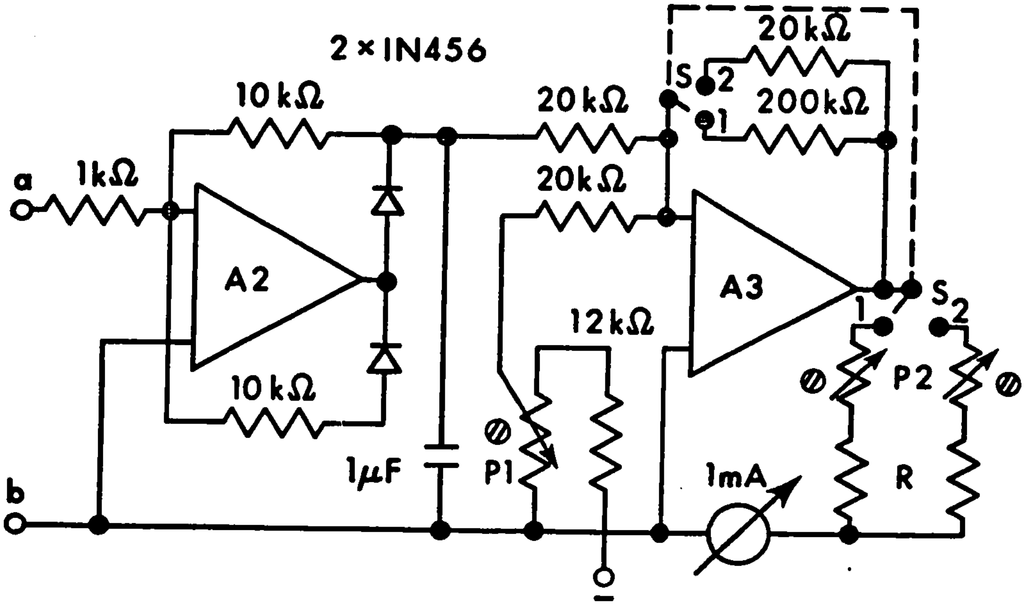
2 × IN456
20 kΩ
S 2
1
200 kΩ
10 kΩ
20 kΩ
a
1kΩ
20 kΩ
A2
A3
S2
1
2
12 kΩ
10 kΩ
P2
1μF
P1
1mA
R
b

We can write ( Harris (1957)) for the unbalance voltage U of the bridge working into infinite impedance,

$$U = E_o \frac{C_4}{C_3+C_4} \frac{\alpha \ell}{1+C_s/C_o+C_4/C_o+\alpha \ell}, \text{ where } \alpha = \frac{\Delta\varepsilon}{\varepsilon_o \ell_o} .$$

For liquid helium when $\alpha\ell << D = 1 + C_s/C_o + C_4/C_o$, the unbalance voltage U is linearly proportional to the liquid level height $\ell$. The magnitude of the voltage U is roughly proportional to $\Delta\varepsilon ( 1 + C_s/C_o )^{-1}$ ( because $C_4 \simeq C_3$ ). In order to keep U large ( $\Delta\varepsilon$ is small for liquid helium ) the bridge circuit is mounted directly on top of the level detecting probe and the capacitance $C_s$ is kept small by the probe construction. In our case $C_s/C_o \simeq 0.8$. This arrangement requires less overall amplification and therefore the requirement for component stability is milder.

When the same system is used with liquid nitrogen, the condition $\alpha\ell << D$ is not as well satisfied and the voltage U is a slightly non-linear function of the level height. In another system, which was used for liquid nitrogen only, the ratio $C_s/C_o = 4$, and U was then a linear function of $\ell$.

The unbalance a.c. voltage U is detected by the differential amplifier ( Burr-Brown (1963)) A1 ( see Fig. A.VI.2 ) which has an input impedance at least ten times the impedance of the capacitors in the bridge at the operating frequency. The signal is amplified ten times and rectified ( Burr - Brown (1963)) by A2 and filtered. A small negative voltage, which serves as a zero adjustment is added to the d.c. voltage at the input to the last amplification stage A3.

Therefore it is sufficient to bring the bridge into an approximate balance and then to zero the system by the potentiometer P1 (350Ω) when there is no liquid present. Since the detection is not phase sensitive, one must insure that the bridge does not pass through the exact balance condition as the level of liquid gas is increased. The liquid level is read on panel meter ( 1 ma F.S. ) and the maximum deflection ( when the system is full of liquid ) is adjusted by R(1kΩ) and P2(350Ω). The values of these two components must be changed if $C_s$ and $C_o$ are changed. The switch S changes the amplification factor by ten and is for liquid helium/nitrogen in the position 1/2.* All operational amplifiers used are of the type NS LM 301 A.

The electronics system follows the bridge unbalance voltage U linearly and disturbs the bridge negligibly. Calibrations carried out for helium and nitrogen fit the dependences predicted for the bridge working to the infinite impedance within 2% at all points. Drift of the system is $\lesssim$ 4% of full scale in about 12 hours for liquid helium sensitivity and about ten times less for liquid nitrogen sensitivity. The stability could be improved by the use of more stable operational amplifiers.

*The amplification in the position 1 is ten times higher than in the position 2.

# APPENDIX VII

## DESCRIPTION OF A TYPICAL RUN

After the glass substrate with gold contacts is clamped to the bottom of the liquid helium pot, the copper shield with the movable mask is screwed to the liquid helium ( LHe ) vessel. The mask is connected by piano wire to an outside dial and the position of the mask is calibrated in terms of the dial reading. Then the copper shield is fastened to the liquid nitrogen ( LN ) vessel and a movable shutter is also connected by steel piano wire to the outside knob. The evaporation sources are filled with fresh metals and the system is sealed off and pumped ( for about 15 hours ) to a vacuum of about $2 \times 10^{-7}$ Torr. Then all evaporation sources are covered by the shutter and are heated up until the evaporation starts, thus melting and degassing the materials which are to be evaporated later. The LN is passed through the Meissner coil inside the evaporation space. The preparation of the junctions is started when the pressure drops below $1 \times 10^{-7}$ Torr.

If a SiO layer is wanted on the substrate, this is evaporated first, then the mask moved and the aluminum base layer is evaporated. The aluminum thickness is monitored by the quartz crystal monitor and the resistivity of the evaporated film is measured simultaneously. When the evaporation of the base layer is completed, the main gate valve is shut off, the flow of LN through the Meissner coil is interrupted and oxygen at a pressure of about 0.1 Torr is introduced into the system. The oxygen is purified by passing it through a coil immersed in LN. Then the whole strip of aluminum is oxidized using the glow discharge. After that, the system is pumped to a pressure of ~ $5 \times 10^{-7}$ Torr within a few minutes. Then the flow of LN through the Meissner coil is again initiated, thus improving the vacuum pressure to ~ $1 \times 10^{-7}$ Torr. The mask is moved to the next position, pressed against the glass substrate and the first layer of the proximity sandwich is evaporated. The thin layer of oxide is allowed to grow (or a layer of SiO less than 20 Å thick is evaporated) and the junction is completed when the second layer of the proximity sandwich is evaporated. The same procedure is repeated for the other junction. When this is done the shutters on both LN and LHe shields are closed. The flow of LN through the Meissner coil is then stopped and the vacuum slowly deteriorates to a value of ~ $3 \times 10^{-5}$ Torr within 10 minutes. After that the pressure quickly drops to the $10^{-7}$ Torr range. This effect is caused by gas molecules trapped on the cold surface of the Meissner coil, which are released as the coil warms.

After the junctions are prepared the level detectors are switched on and all three vessels are filled with LN. (Nitrogen vessel,helium vessel and helium pot,into which the LN is syphoned through the 1/8 inch diameter pumping hole ). The filling of the system with LN can be finished within half an hour. Thermal equilibrium with LN in the nitrogen vessel ( no violent boiling) is usually reached after 1 hour; in the other two vessels the equilibricum is reached much sooner. At this stage it is safe to leave the system for about 20 hours without refilling.

In order to cool the sample to LHe temperature, we proceed as follows. A thin stainless steel tube is inserted into the helium pot and LN is blown out. Then the helium pot is pumped to about $10^{-2}$ Torr and LN is blown out of the LHe vessel. The helium pot ( and all system with which it is interconnected ) is filled with He gas at atmospheric pressure. A copper rod is inserted through the 1/8 inch hole into the helium pot to provide heat contact with the LHe vessel ( through the exchange gas in the helium pot system ). Then LHe is transferred into the LHe vessel. After the temperature of the helium pot reaches about 5 to 8°K ( in about 20 or 30 minutes ), the copper rod is replaced by a thin syphon and the helium pot is filled with LHe. The helium level is detected by a carbon resistor placed in the pumping line about 7 inches above the top of the helium pot. At the beginning of the LHe transfer the temperature of the helium pot is increased to about 10°K by warm gas from the inside of the syphon tube. About 10 litres of LHe are required to cool the system from LN temperature and fill it with about 5 litres of LHe.

The temperature during the measurement is regulated by controlling the vapor pressure of LHe in the helium pot. The lowest attainable temperature is 1.05°K. We tried to lower the temperature by pumping both the helium pot and the LHe vessel simultaneously; however the temperature was decreased about 20m°K only at the lowest attainable temperature.

After all the measurements are finished the LHe is boiled off ( from the pumping pot by a heater in situ, from the LHe vessel by a dipstick heater ) and the system is left overnight to warm up by radiation. Next morning the main gate valve is shut off and the evaporator - cryostat is filled with helium gas at a pressure of a few Torr. About three hours later the system is all at room temperature.

# BIBLIOGRAPHY

Adkins,C.J. and Kington,B.W. (1969) Phys. Rev. 177, 777.

Andrew,E.R. (1949) Proc. Phys. Soc. 62, 77.

Bardeen,J., Cooper,L.N., and Schrieffer,J.R. (1957) Phys. Rev. 108, 1175.

Bassewitz,A.v. and Minnigerode,G.v. (1964) Z. Physik 181, 368.

Bermon,S. (1964) National Science Foundation, Grant # NSF-GP1100, Technical report No.1, March 20.

Blakemore,J.S., Winstel,J., and Edwards,R.V. (1970) Rev. Sci. Instr. 41, 835.

Burr-Brown Research Corporation (1963) Handbook of Operational Amplifier Applications (First Edition).

Cabrera,N. and Mott,N.F. (1949) Rept. Progr. Phys. 12, 163.

Capocci, F.A. and Gugan,D. (1967) Cryogenics 7, 374.

Caswell,H.L. (1964) Phys. Let. 10, 44.

Chambers,R.G. (1950) Proc. Royal Soc. A 202, 378.

Chiou,C. and Klokholm,E. (1964) Acta Metallurgica 12, 883.

Claeson,T. and Gygax,S. (1966) Solid State Communications 4, 385.

Claeson,T., Gygax,S., and Maki,K. (1967) Phys. Kondens. Materie 6, 23.

Cooper,L.N. (1961) Phys. Rev. Let. 6, 689.

Cooper,L.N. (1962) IBM Journal 6,75.

Dash,J.G. and Boorse,H.A. (1951) Phys. Rev. 82, 851.

Davis,H.T. (1935) Tables of Higher Mathematical Functions, Principia Press, Inc., Bloomington, Indiana, Vol. I.

Deutscher,G. and De Gennes,P.G. (1969) chapt. 17 "Proximity effects" in the book by R.Parks: Superconductivity, New York, M.Dekker, Inc.

De Gennes,P.G. and Guyon,E. (1963) Phys. Let. 3, 168.

De Gennes,P.G. (1964a) Rev. Mod. Phys. 36, 225.

De Gennes,P.G. (1964b) Phys. Kondens. Materie 3, 79.

De Gennes,P.G. and Mauro,S. (1965) Solid State Communications 3, 38.

Dignam,M.J., Fawcett,W.R., and Böhni,H. (1966) J. Electrochem. Soc. 113, 656.

Dijk,H.van, Durieux,M., Clement,J.R., and Logan,J.K. (1960) The "1958 $He^4$ Scale of Temperatures", NBS Monograph 10, June 17.

Elliott,R.P. (1965) Constitution of Binary Alloys, First Supplement, McGraw Hill, Inc.

Falk,D.S. (1963) Phys.Rev. 132, 1576.

Falkoff,A.D. and Iverson,K.E. (1968) APL/360 Users Manual, IBM Corporation.

Freake,S.M. and Adkins,C.J. (1969) Phys. Let. 29A, 382.

Fromhold,A.T.Jr. and Cook,E.L. (1967) Phys. Rev. 158, 600.

Fuchs,K. (1938) Proc. Cambridge Phil. Soc. 34, 100.

Fulde,P. and Maki,K. (1965) Phys. Rev. Let. 15, 675.

Guyon,E., Martinet,A., Mauro,S., and Meunier,F. (1966) Phys.

Kondens. Materie 5, 123.

Handy,R.M. (1962) Phys. Rev. 126, 1968.

Hansen,M. (1958) Constitution of Binary Alloys, New York, Mc Graw Hill.

Harris,F.K. (1957) Electrical Measurements, New York, John Wiley and Sons, Inc.

Hart,R.K. (1956) Proc. Roy. Soc. (London), A236, 68.

Hauser,J.J., Theuerer,H.C., and Werthamer,N.R. (1964) Phys. Rev. 136, 637.

Hauser,J.J. and Theuerer,H.C. (1965) Phys. Let. 14, 270.

Hauser,J.J., Theuerer,H.C., and Werthamer,N.R. (1966) Phys. Rev. 142, 118.

Heavens,O.S. (1950) J.Sci. Instr. 27, 172.

Heavens,O.S. (1951) Proc. Phys. Soc. London B64, 419.

Hilsch,P. (1962) Z. Physik 167, 511.

Holland,L. (1963) The Vacuum Deposition of Thin Films, Chapman and Hall Ltd., (London).

Holwech,I. and Jeppesen,J. (1967) Phil. Mag. 15, 217.

Jones,B.K. (1969) Cryogenics 9, 214.

Kahan,G.J., DeLano,R.B.,Jr., Brennemann,A.E., and Tsui,R.T.C. (1960) IBM Journal 4, 173.

Kaiser,A.B. and Zuckermann,M.J. (1970) Phys. Rev. B1, 229.

Klokholm,E. and Chiou,C. (1964) IBM Research Note, Thomas J. Watson Research Center, Yorktown Heights (12/23/64).

Mayadas,A.F. and Shatzkes,M. (1970) Phys. Rev.B1, 1382.

McMillan,W.L. (1968) Phys. Rev. 175, 537.

Meiboom,S. and O'Brien,J.P. (1963) Rev. Sci. Instr. 34, 811.

Meissner,H. (1960) Phys. Rev. 117, 672.

Miles,J.L. and Smith,P.H. (1963) J. Appl. Phys. 34, 2109.

Miles,J.L. and Smith,P.H. (1963a) J. Electrochem. Soc. 110, 1240.

Mott,N.F. (1939) Trans. Faraday Soc. 35, 1175.

Mott,N.F. (1940) Trans. Faraday Soc. 36, 472.

Mott,N.F. (1947) Trans. Faraday Soc. 43, 429.

Preshkov,V.P., Vetchinkin,A.N., and Elkonin,B.V. (1969) Cryogenics 9, 133.

Riegert,R.P. (1968) IBM Journal 12, 46.

Rogers,J.S. (1970) Rev. Sci. Instr. 41, 1184.

Rose-Innes,A.C. and Serin,B. (1961) Phys. Rev. Let. 7, 278.

Seguin,H.J. and Leonard,R.W. (1966) Rev. Sci. Instr. 37, 1743.

Simmons,W.A. and Douglass,D.H.,Jr. (1962) Phys. Rev. Let. 9, 153.

Smith,P.H., Shapiro,S., Miles,J.L., and Nicol,J. (1961) Phys. Rev. Let. 6, 686.

Sondheimer,E.H. (1952) Advances in Physics 1, 1.

Strongin,M., Kammerer,O.F., and Paskin,A. (1965) Phys. Rev. Let. 14, 945.

Strongin,M., Thompson,R.S., Kammerer,O.F., and Crow,J.E. (1970) Phys. Rev. B1, 1078.

Tolansky,S. (1960) Surface Microtopography, Longmans, Green and Co. Ltd.

Tolansky,S. (1948) Multiple Beam Interferometry of Surfaces and Films, Oxford.

Tsuya,Hideki (1967) J. Phys. Soc. Jap. 23, 975.

Van Gurp, G.J. (1963) Phys. Letters 5, 303.

Vrba, J. and Woods, S.B. (1971) Phys. Rev. B, April.

Werthamer,N.R. (1963) Phys. Rev. 132, 2440.

Williams,W.E.,Jr. and Maxwell,E. (1954) Rev. Sci. Instr. 25, 111.

Woolf, M.A. and Reif, F. (1965) Phys. Rev. 137, 557.